UNIVERSITY OF SOUTHAMPTON

Faculty of Engineering and Physical Sciences
School of Physics and Astronomy

Microcavity Enhancement of Terahertz Absorbing metamaterials

DOI: 10.100 2/0470841559.ch1

Volume 1 of 1

by

Lewis Kieran Piper

MPhys

ORCiD: 0000-0002-1825-0097

A thesis for the degree of
Doctor of Philosophy

June 2022

University of Southampton

Abstract

Faculty of Engineering and Physical Sciences
School of Physics and Astronomy

Doctor of Philosophy

Microcavity Enhancement of Terahertz Absorbing metamaterials

by Lewis Kieran Piper

This work pertains to the design, development and experimentation of Terahertz Metasurfaces and their inclusion within microcavities to achieve a near perfect, tunable absorber. Early chapters discuss terahertz technology, its applications and the obstacles needed to overcome for its further development. After which the theory behind metamaterials and more specifically split ring resonators is discussed along with simulations of multiple resonator designs with a resonant response within the Terahertz domain.

The theory behind and the experimental results for the metamaterial microcavities is discussed and shows that the resonant response of these materials is tunable through manipulation of the cavity. The mechanisms behind the interactions between the microcavity and the metamaterial are explored through simulations which show the enhancement effect is caused by the interference between light that travels through the microcavity and the light reflected from the metasurface. Experimentally it is shown that absorption can be achieved up to -45.8dB through the manipulation of the aforementioned metamaterial and microcavity while also displaying a phase singularity in phase space around this peak absorption. This achievable high absorption and tunability would allow for accurate detection of THz across a tunable range of frequencies.

Further work is proposed for next stages of implementation of the microcavities.

Contents

List of Figures

Declaration of Authorship

I declare that this thesis and the work presented in it is my own and has been generated by me as the result of my own original research.

I confirm that:

1. This work was done wholly or mainly while in candidature for a research degree at this University;
2. Where any part of this thesis has previously been submitted for a degree or any other qualification at this University or any other institution, this has been clearly stated;
3. Where I have consulted the published work of others, this is always clearly attributed;
4. Where I have quoted from the work of others, the source is always given. With the exception of such quotations, this thesis is entirely my own work;
5. I have acknowledged all main sources of help;
6. Where the thesis is based on work done by myself jointly with others, I have made clear exactly what was done by others and what I have contributed myself;
7. Parts of this work have been published as: Lewis K. Piper, H. Johnson Singh, Jonathan R. C. Woods, Kai Sun, Otto L. Muskens, and Vasilis Apostolopoulos. Mechanically tunable terahertz metamaterial perfect absorber. *Advanced Photonics Research*, 2:2100136, 12 2021. ISSN 2699-9293. . URL https://onlinelibrary.wiley.com/doi/full/10.1002/adpr.202100136

Signed:..... Date:.....

Acknowledgements

This is an acknowledgement of those people and things who helped me mentally, physically, financially and otherwise. Hazel Piper, Kevin Piper, My Grand Parents, Step-Parents, my cats, Supervisors, Coffee, Lee Bois, BBAS, God Emperor of Man, Dr Ayers, Gin, more Coffee, Antidepressants and The University severely underpaying me...

Dedicated to the memory of my mental health that died in the process of this work

Academia is no place for the truth

-Vasilis Apostolopoulos

Definitions and Abbreviations

THz	Terahertz
SRR	Split Ring Resonator
PCA	Photo Conductive Antenna
QCL	Quantum Cascade Laser
$LiNbO_3$	Lithium Niobate
MPA	Metamaterial Perfect Absorber

Chapter 1

Introduction

1.1 Background

The Terahertz (THz) regime is a band of electromagnetic frequencies ranging from $0.1 - 10$ THz ($30\ \mu$m-1 mm)[2–10] which sits between the radio-wave and infra-red radiation. Due to the ability of THz electromagnetic waves to penetrate non-conducting materials without causing ionization, THz technologies are implemented in a large range of fields and industries, as illustrated in figure 1.1, and can be roughly divided into imaging, spectroscopy, and communications. In imaging applications, the contrast between transparent materials and metallic or polar materials can be used to identify concealed objects, which is of interested for example for security [11–13]. For similar reasons, THz radiation finds use in nondestructive testing [14, 15]. Many materials have specific THz spectroscopic fingerprints that can be detected. This characteristic feature has led to many applications of THz spectroscopy in areas such as Chemistry [16–24], Medical [14, 25–29], biological imaging [26, 30], pharmaceutical industry [31–37], and food production and testing [38–47]. THz-enabled communication is an extension of microwaves and is proposed as the next generation of wireless communication known as 6G [10, 48–58]. Finally THz spectroscopy is used in fundamental scientific research, such as condensed matter physics and is of interest for characterisation of some types of objects in astronomy, e.g. spectroscopic analysis of asteroids and comets [59, 60]. The extremely wide range of applications and reach of THz technologies in science and society testifies the importance of developing new platforms for generating, controlling and detecting THz electromagnetic radiation.

In the following I will briefly highlight some of the main developments relevant to this thesis, related to the field of THz spectroscopy and the use of metamaterials as components in the THz domain. At the end of this chapter the aim and objectives of the thesis are summarised.

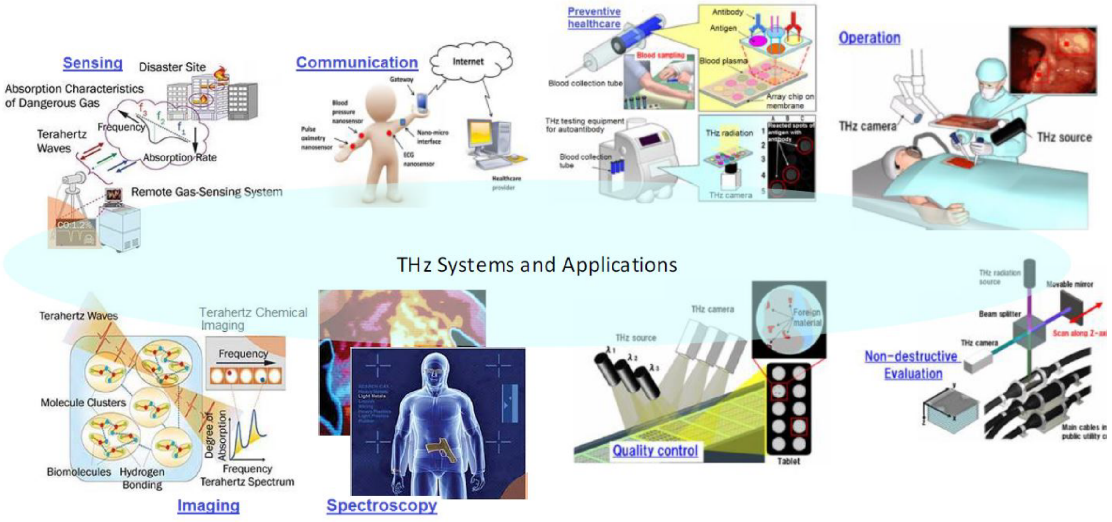

FIGURE 1.1: Typical application areas for THz imaging and spectroscopy. Image reproduced from [38].

1.2 Electromagnetic spectrum and the THz gap

The electromagnetic spectrum can be divided into two distinct regions as is shown in Figure 1.2. The first is the part of the spectrum of Microwaves and longer wavelengths which is generated using electronic methods such as antenna. The second is the part of the spectrum of Far Infra-Red and shorter wavelengths which are generated using optical and photonic methods such as lasers. The limitations of the electronic region of the spectrum are caused by heating effects from driving antenna at the corresponding electrical frequencies. The optical region of the spectrum is limited as the lower frequencies due to thermal background noise from black body radiation. Between these two regions is the terahertz gap, in order to generate THz alternative methods must be utilized.

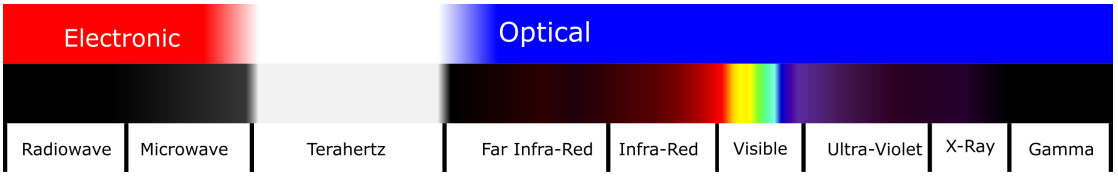

FIGURE 1.2: The Terahertz gap is situated between Microwave and Far Infra-Red ranging from $0.1 - 10\ THz$. The electromagnetic spectrum can be divided into two major regions based on their generation methods. The electronic part of the spectrum refers to the electromagnetic waves generated through antenna such as radio waves. The optical region contains the higher frequency waves created by optical effects such as lasers. Between these two regions is the Terahertz Gap, which is formed by the limits of the Electronic and Optical regions.

The Terahertz regime lays between the Microwave and Infra-red regimes of the electromagnetic spectrum. Ranging from 0.1 - 10 THz, it covers an region of the electromagnetic spectrum which conventional generation of EM waves is impractical. Microwaves, radio-waves and other long wavelength EM waves can easily be generated through the oscillation of a electrical current inside of an antenna. The acceleration of electrons within the antenna causes the emission of EM waves with a corresponding frequency to that of the current. The difficulty of generating THz this way is that the required high frequency of the electrons oscillating causes heating of the antenna which in turn causes damage.

The terahertz gap exists due to issues with emission and detection of electromagnetic frequencies within this region. Difficulties arise when terahertz is attempted to be generated electronically due to the high frequency of electron oscillation required which leads to physical limits in hardware. Additionally it is difficult to generate optically as it resides below infra-red on the frequency spectrum and is dominated by thermal effects from black body radiation. Like infra-red and microwave, THz is non-ionizing and can penetrate a large number of non-conducting materials such as wood and plastic, however THz is heavily absorbed by water due to its molecular bonds [61, 62].

As the THz spectrum crosses over from the electronic to optical domains this offers both challenges and new opportunities for finding solutions to control electromagnetic radiation in the THz gap where many of the conventional approaches from electronics and photonics break down. For example, conventional optical elements that are based on refractive index variation and polarization, such as fibres and waveplates, are cumbersome to achieve and are mostly inefficient at the longer wavelength range of the THz domain. On the other hand, conventional electronics reaches it limits above a few hundred GHz frequency.

As it turns out, metasurfaces are an ideal platform to create new optical functionalities in the THz range where traditional optical elements are lacking, primarily on account of their ability to create independent custom electric and magnetic responses to incident radiation. As such the development of new materials and structures for the THz regime to facilitate improved devices and components is the focus of intense research. Initial excitement in this field has focused on electromagnetic metamaterials and metasurfaces which exhibited unique properties which simply cannot be achieved with conventional materials [63–67]. Since the early studies, many new applications have been investigated which include replicating also more basic functionalities of optical devices.

1.3 Metamaterials and metasurfaces

Metamaterials and their planar equivalent metasurfaces are sub-wavelength structures that are designed to have properties that are not see in the bulk material they are made from. This is achieved by creating structures that have features that are sub-wavelength in size. By creating these features, when light interacts with the metamaterial it is unable to resolve these sub-wavelength features and interacts with the metamaterials as though it were a homogeneous structure. By changing these sub-wavelength features the perceived material the light interacts with can be finely tuned to create a large assortment of different properties

Different metamaterial configurations can have positive or negative permitivity(ϵ) and permeability(μ). By engineering the desired values of ϵ and μ different material responses can be induced, such as negative refractive indices [68, 69] , electromagnetic resonances[70], second harmonic generation[71] and superconducting meta-devices [72] . Examples of their applications include light harvesting [73], optical sensors[74], second-harmonic generation[75], negative refractive indices[76] and thermal black-body control[77]. Several methods for achieving a perfect absorber based on metasurfaces have been demonstrated, which include the addition of metallic films[78], graphene[79], multiple metamaterial geometries [80], the use of semiconductor structures[81], and the inclusion of metamaterials within microcavites[82].

The Permittivity(ϵ) and Permeability(μ) of different types of materials and metamaterials are shown in figure1.3. In the top right, Positive Permittivity and Permeability, corresponds to dielectric and conventional materials. The top left section is where most magnetic materials are found including split ring materials. The bottom right sector contains metals and electrical plasma. The bottom left sector corresponds to negative refractive indices and other properties that aren't found in nature. [83, 84]

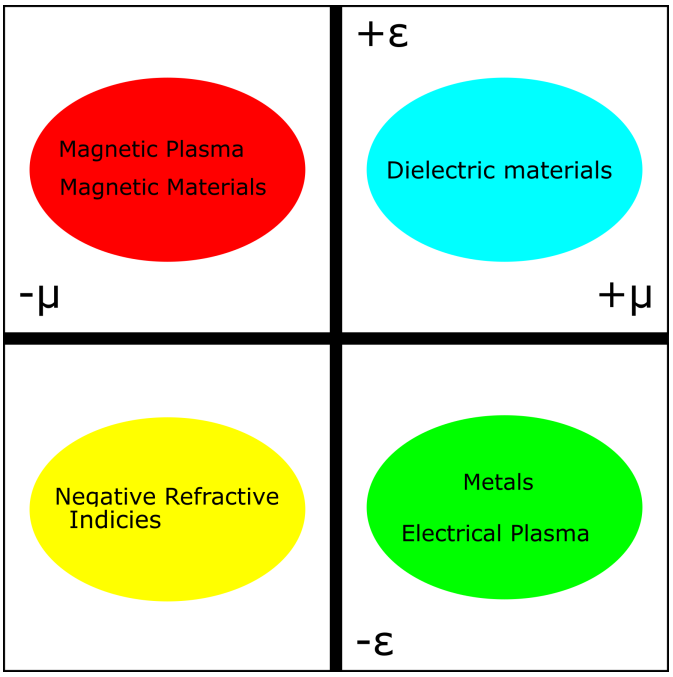

FIGURE 1.3: The Permittivity(ϵ) and Permeability(μ) of different types of materials and metamaterials. In the top right, Positive Permittivity and Permeability, corresponds to dielectric and conventional materials. The top left section is where most magnetic materials are found including split ring materials. The bottom right sector contains metals and electrical plasma. The bottom left sector corresponds to negative refractive indices and other properties that are not found in nature.

1.4 Terahertz Metamaterials

Metamaterials based on split ring resonators (SRRs) have been shown to create THz metamaterials that show a resonant response to incident EM waves [7, 85, 86]. By taking advantage of the very high refractive index of metallic structures in the terahertz spectral region, the response of the metamaterials can be easily scaled geometrically for different wavelengths. Metamaterial concepts have been successfully applied to other parts of the electromagnetic spectrum including the infrared and visible domains. An important category of devices using this technology platform are the metamaterial perfect absorbers (MPAs) which have been realized over a significant portion of the electromagnetic spectrum [78, 79, 87, 87–96].

Alongside static applications, the possibility of realising devices with tunable or reconfigurable characteristics is of interest for achieving flexible and agile functionalities. Adjustable structures achieve tunability for example through mechanical tuning, electromechanical displacement and thermal stimulation. Mechanical tuning requires the deformation and flexing of a structure to change its properties, such as constructing split rings on a flexible substrate e.g polymide [97], by deforming the substrate, the spacings of the SRR's change and the resonant frequency shifts accordingly [98].

Electromechanical displacement works on a similar principle to mechanical tuning but uses an external electrical bias to induce mechanical deformation of metamaterial structures to control their resonant frequency [99–101]. Similarly thermal stimulation uses a material, such as STO (strontium titanate), in which the magnetic permeability is dependant on temperature and allows to control the resonance of the surrounding metamaterials [4, 102].

Electrical tuning of metamaterials can be achieved for example using doped semiconductors [103] or graphene [79]. Through methods such as chemical doping or electrical gating [5] the carrier density, photonic response and carrier mobility can be altered which in turn changes the properties of surrounding meta materials [104–106].

1.5 Thesis Outline

This thesis presents an experimental investigation into the resonant characteristics of THz split-ring resonators using both transmission and reflection time-domain THz setups. The main aim is to achieve precise control over the electromagnetic absorption of THz radiation by combining the resonant metamaterial and a metallic back reflector in a mechanically controllable microcavity configuration. Through fine control of these components it is to be shown that the strength of the resonant response central frequency can be shifted as-well as the strength of the resonant response can be greatly amplified.

Chapter 2 introduces some of the basic principles of THz metamaterials. Here I briefly discuss the background theory of metamaterials and then more specifically the theory for the metamaterials used in this work based on split ring resonators (SRRs). In the end of the chapter I describe the fabrication process used to create the metamaterials used in the experimental sections of the report.

Chapter 3 provides an overview of methods and techniques for Terahertz generation and detection and how these methods for generation and detection are used.

In Chapter 4 I look into the Terahertz time domain spectroscopy, how transmission and absorption are calculated and show the experimental setups used in this thesis for measurements. Additionally I discuss the work done In Terahertz Echo Self Referencing.

Chapter 5 discusses the theory and experimental results for microcavity control over the metamaterial response. It is shown here that the resonant response of the metamaterial can be finely controlled through the use of a a metallic back reflector in such a way that demonstrates both fine control over the resonant responses position and the strength of the response.

In Chapter 6 I am laying down the Future prospects and conclusions of this project that would potentially allow for greater control of the resonant position of the microcavity. It is proposed that the inclusion of additional components such as membrane or additional materials such as lithium niobate or Antimony Trisulfde would allow for such changes.

Chapter 2

Theory and simulation of THz metamaterials

2.1 Introduction

This chapter provides an overview of the theory of metamaterials, and particularly split ring resonators (SRRs) and presents simulations of their THz optical response. Split ring resonators are a family metamaterials that exhibit magnetic and electrical resonant responses, which allows for them to be used in a large range of applications such as those mentioned in the introduction i.e negative refractive indices. The basic principles of the split ring resonator are that of an inductance and capacitance circuit which is discussed later in this chapter. This chapter looks at multiple resonator designs that exhibit useful properties for the work done later in this project.

First, the basic theory of the coupled capacitance and inductive response of SRRs is given and the resulting resonance behaviour is discussed. Next, results on the numerical simulation of these resonators on a dielectric substrate are presented and the dependence on variations in the design parameters as well as the local environment of the resonators is discussed. Finally, the effect of different resonator designs is discussed.

2.2 Split Ring Resonator Equation

Figure 2.1 shows the geometry of a simple SRR. An SRR geometric has properties of inductance and capacitance that lead to the electromagnetic resonance. On either side of the gap, the edges of the ring become charged plates and act like a capacitor, the ring itself acts as an inductance coil [107–111]. The resonant frequency of a SRR is given by equation 2.1 where L is the inductance of the ring part of the SRR, C is the capacitance of the SRR's gap and f_{LC} is the resonant frequency [112]. The derivation of equation 2.1 from the geometry and material properties is given in Appendix A.

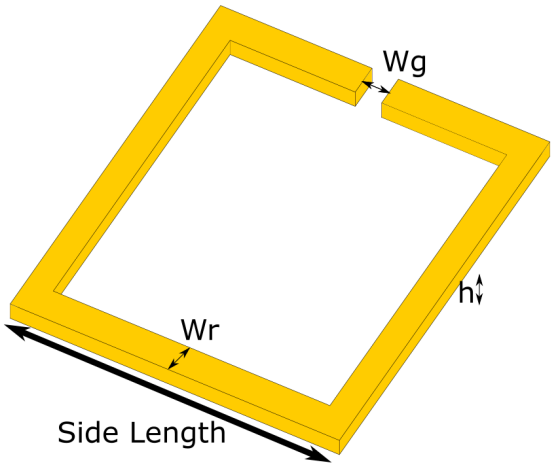

FIGURE 2.1: The Resonant frequency of a SRR is dependant on its geometry and material properties. Equations 2.1-2.12 show how different material properties and parts of the SRR's geometry effect the resonance.

$$f_{LC} = \frac{1}{2\pi\sqrt{LC}} \tag{2.1}$$

$$L_s = \mu_0 \frac{A}{t} \tag{2.2}$$

(2.2) Is the self inductance of the SRR due to its geometric properties. The self inductance is modelled on a solenoid with only one turn which is proportional to the surface area of the single turn,A, and inversely proportional to the length of the solenoid, which in this case is the effective thickness t.

$$E_{inductor} = \frac{1}{2} i^2 L_{kin} \tag{2.3}$$

$$v = \frac{i}{Anq} \tag{2.4}$$

$$E_{kin} = \frac{1}{2}(mnAlv^2) \tag{2.5}$$

$$E_{kin} = \frac{1}{2}\frac{lm}{Anq^2}i^2 \tag{2.6}$$

$$L_{kin} = \frac{l}{A}\frac{m}{nq^2} \tag{2.7}$$

$$\omega_p = \sqrt{\frac{nq^2}{m\varepsilon_0}} \tag{2.8}$$

$$L_{kin} = \frac{l_{eff}}{\varepsilon_0\omega_p^2 w_{eff} t} \tag{2.9}$$

Equations 2.3 - ?? show the derivation of the kinetic inductance. 2.3 shows the energy stored within an inductor where L_{kin} is the inductance of the inductor and i is the current passing through the inductor. Equation 2.4 shows the velocity of the charge carriers v is proportional to the current in the inductor and inversely proportional to the area (A) of the inductor, the charge of the charge carriers (q) and the number of charge carriers (n). Equation 2.5 is for the kinetic energy of the charge carriers in the inductor, where m is the mass of the charge carriers and l is the length of the inductor. By substituting equation 2.4 into equation 2.5 we arrive at equation 2.6. By equating equations 2.3 and 2.6 we can solve for the the kinetic inductance and get equation 2.7. Equation 2.8 is the plasma frequency equation, if we substitute this into equation 2.7 along with the resonators effective length (l_{eff}), thickness (t) and width (w_{eff}) we arrive at equation 2.9 for kinetic inductance.

(2.9) Is the kinetic inductance is created from the kinetic energy of the charge carrier within the split ring resonator.This inductance is suppressed by the plasma frequency (w_p) of the resonators material i.e gold. ring length (l_{eff}), the effective ring width (w_{eff}).

$$L = L_s + L_{kin} \tag{2.10}$$

(2.10) The total inductance of the SRR is equal to the sum of the self inductance and the inductance of the free electrons as given in equations 2.2 and 2.9.

$$C = \varepsilon_0\varepsilon_g\frac{w_g h}{d} \tag{2.11}$$

(2.11) The capacitance of an SRR is modelled as a plate capacitor where w_g is the width of the SRR at the gap, h is the height of the SRR and d is the width of the gap.

L is the inductance of the ring and C is the capacitance of the SRR gap. Both the inductance and the capacitance are based on the geometric and material properties of the SRR, using equations 2.10 and 2.11 for the the inductance and capacitance respectively the resonant frequency of the SRR can be determined. The derivation of these equations can be found in Appendix A.

Due to the plasma frequency of gold being $2.15PHz$ [113] the kinetic inductance(L_{kin}) as show in equation 2.9 is on the order of $10^{-18}H$ and much smaller than the Self inductance(L_s) which is of the order ($10^{-7}H$), because of this the kinetic inductance can be ignored. The width(w_g) of the gap is the same as the gap separation (d) and μ_0 ε_0 is equal to ${v_c}^2$ where v_c is the speed of light in a vacuum. This means the resonance frequency can be simplified to equation 2.12 ε_g is the effective index of the SRR gap (n_{eff}^2):

$$f_{LC} = \frac{1}{2\pi\sqrt{L_s C}} = \frac{1}{2\pi\sqrt{\mu_0\varepsilon_0\varepsilon_g w_g h\frac{A}{td}}} = \frac{v_c}{2\pi\sqrt{\varepsilon_g h\frac{A}{t}}} = \frac{v_c}{2\pi n_{eff}}\sqrt{\frac{t}{h}}\frac{1}{\sqrt{A}} \tag{2.12}$$

Equation 2.12 shows a reduced version of equation 2.1 where the resonant frequency of the split ring can be seen to be inversely proportional to the square root of the area of the SRRs inductance region.

2.2.1 Charge and Current

The split ring resonator equation, equation 2.1 described the resonant frequency as a product of the rings Capacitance (C) and Inductance (L). This can be shown through simulating the current and charge distributions in the resonators as seen in figures 2.2 and 2.3. As the frequency of the terahertz approaches the SRR's resonant frequency, there is a charge build up either size of the resonators gap, like that of a capacitor. Similarly a current is formed from the movement of these charges such as in an induction circuits. As the frequency continues to increase the charge build up dissipates and the current reverses before dissipating also. At additional resonant frequencies, the charge build up again occurs at the resonators gap but also at other points throughout the resonator akin to a standing wave with nodes and anti-nodes. Figure 2.2 shows the charge build up across an SRR when the incident terahertz's polarization is parallel to the SRR's gap. The sub-figures of the figure show the charge distributions for the diff rent resonant responses of the SRR with sub-figure a) displaying the charge build up at the primary resonance and sub-figures b) and c) showing the secondary and tertiary resonances, in each case the charge accumulates in evenly distributed nodes across the ring of alternating positive and negative charges, with the rings gap having a positive and negative charge on either side. Figure 2.2 d) shows the charge build up across the

SRR but where the terahertz is perpendicular to the SRR's gap. Similarly to the charge distributions in sub-figures a)-c), the charge builds up on opposing sides of the SRR but in this instance the charge build up occurs perpendicular to the SRR gap.

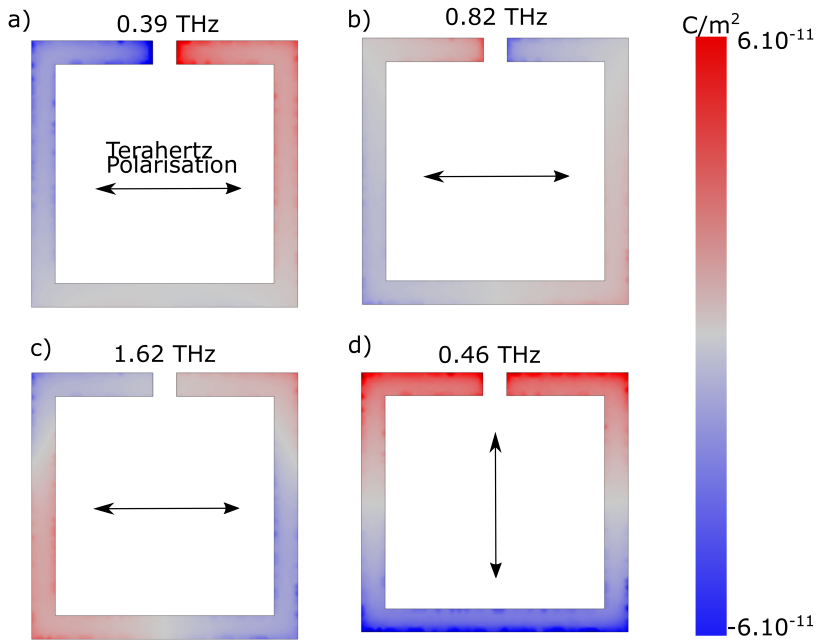

FIGURE 2.2: This figure shows the charge distributions of a simulated SRR at its different resonances.a), b) and c) are the resonances for when the incident terahertz is parallel to the SRR gap (horizontal on the page). d) Is the resonance for when the incident terahertz is perpendicular to the SRR gap (vertical on the page). These charge distributions show that at resonance, the charge is distributed in an alternating series of positive and negative nodes. The primary resonance, a), has these nodes on each side of the SRR gap, as you see in a capacitor. The secondary and tertiary resonances , b) and c) respectively, also show this charge build up on each side of the SRR gap but with additional charge build up throughout the ring. Due to this spread of charges the capacitance experienced at the gap, which corresponds to the higher resonant frequency of these subsequent resonances. d) shows the charge distribution when the incident terahertz is perpendicular to the SRR gap, which results in the charge also being distributed perpendicular to the gap

Figure 2.3 is similar to figure 2.2 a) and d) but with the inclusion of the induced current, shown in the black arrows. In sub-figure a) where the polarization incident terahertz is parallel to the SRR's gap, the induced current flows around the SRR in a coil. In sun-figure b) however, where the incident terahertz is polarized perpendicular to the SRR's gap, the current flows from one end of the resonator to the other on each of its side as in two parallel wires. By comparing the charge and current shown in sub-figure a) in both figure 2.2 and figure 2.3 with equation 2.1, the reason for the SRR being modeled as a inductance-capacitance circuit becomes clear, with the charge build up on either side of the SRR's gap acting as a capacitor and the current coiling around the SRR acting as an inductance coil.

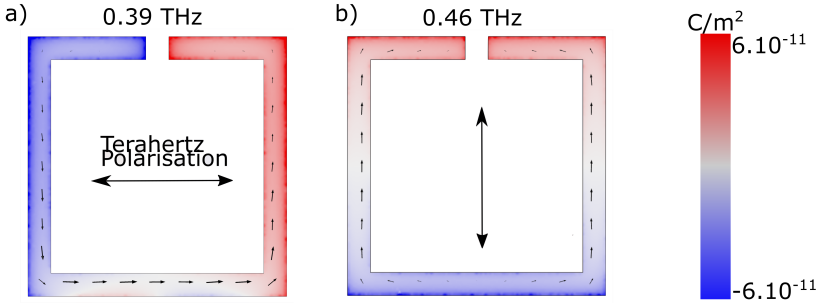

FIGURE 2.3: These figures show the same charge distributions as figure 2.2 a) and d) with the induced current displayed over them shown in black arrows. The current in a) passes through the SRR in a loop from one end to the other. this corresponds to the charge build up around the SRR gap. b) on the other hand shows the current passing from

2.3 Simulations of split ring resonators

In order to determine the appropriate size and design for a the resonators used in this work, simulations were conducted in Comsol multi physics, initially with version 5.2 but progressed to version 5.5a as the software was updated.

2.3.1 Design

The metamaterial design consists of three layers. The bottom layer is a layer of gold 2 µm thick, the middle layer is a substrate which can be made of several materials such as silica quartz because it is highly transmissive and has no natural resonances within the THZ range . The top layer is a 100 nm thick gold pattern which is a configuration of split ring resonators (SRRs) which have a resonance within the THz regime. This is shown in Figure 2.4. By adjusting the thickness and material of the substrate the metamaterial can be tuned to increase absorption and also to change the resonance frequency.

FIGURE 2.4: The structure on which the SRRs will be deposited via thermal deposition . The SRRs sit atop a substrate which separates the SRRs and the Gold layer.

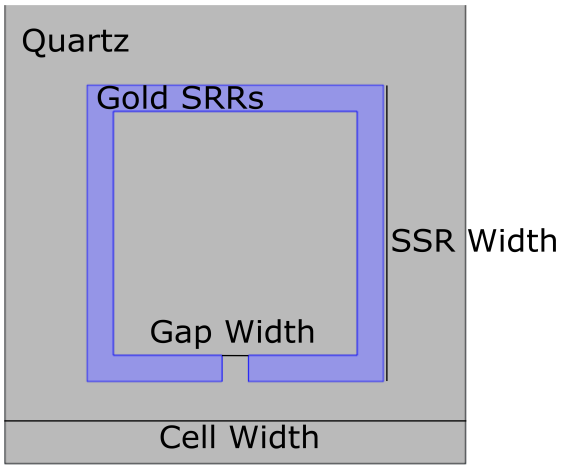

FIGURE 2.5: The geometry of a square SRR on top of the Quartz substrate.

Figure 2.5 shows the design of the SRR unit cell from the top layer of figure 2.4. This unit cell is repeated across the surface of the substrate to give a large array of SRRs. the separation of the SRRs can be also adjusted to tune the absorption of the metamaterial.

The metamaterial will be fabricated by using methods described in Section 4.2. The SRR will be fabricated using thermal vapour deposition to create the layer of gold and photo lithography to remove excess gold and create the SRR pattern. The substrate can be fabricated by spinning a photo resist to the desired thickness and then hardened. Alternatively a spacer ring can be used in place of a substrate to create a layer of gas or a pre-existing layer of material such as silica quartz can be used and the back reflector layer and the SRR layer built upon it. A spacer ring would be used so that different gasses could be passed over the SRRs in order to see their effects on the SRRs resonance.

2.3.2 Simulations: Comsol

Comsol is a simulation software that was used for the simulations within this work. Comsol works using the finite element method to preform these simulations. This

method allows for solving partial differential equations into numerical solutions. In Comsol the simulated space, in this case a split ring resonator, is created using the built in geometry tool. Then the different materials of the object are defined as are the equations that the simulated is to be solved for i.e electromagnetic waves, the properties of the incident THz waves, such as direction, polarization and power . The model is then broken up into a series of finite elements (hence the name). The systems equations are then applied to where these finite elements meet to produce a corresponding number of linear equations. These equations are then solved for, the more finite elements, the longer the simulation takes but the mesh element size must adhere to the Nyquist theorem and be smaller than half the wavelength of the incident EM radiation. In the simulations in this work, the incident THz radiation was polarized and a plane-wave at normal incidence and minimum wavelength 40 microns.

The metamaterial design consists of three layers. The bottom layer is a layer of gold 300 *nm* thick, the middle layer is a substrate which can be made of several materials such as silica quartz because it is highly transmissive and has no natural resonances within the THZ range . The top layer is a 100 *nm* thick gold pattern which is a configuration of split ring resonators (SRRs) which have a resonance within the THz regime. This is shown in Figure 2.6. By adjusting the thickness and material of the substrate the metamaterial can be tuned to increase absorption and also to change the resonance frequency.

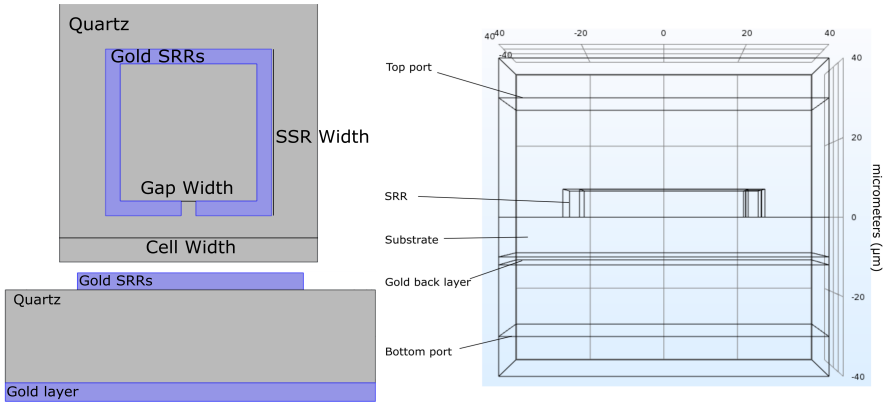

FIGURE 2.6: a) SRR unit cell layout as seen in figure 2.1 upon a quartz substrate. b) One of the simulation configurations in profile. A layer of gold SRRs on a quartz substrate which is has a 300 nm thick layer of gold on the opposite facing side. c) Side profile of the larger simulation unit cell.The top port acts as input for THz and the top and bottom ports act measure the amount of reflected and transmitted THz respectively. The thickness of the SRR layer has been increased for illustration purposes only, not to scale.

Figure 2.6 a) shows the design of the SRR unit cell from the top layer of figure 2.6 b). This unit cell is repeated across the surface of the substrate to give a large array of SRRs. the separation of the SRRs can be also adjusted to tune the absorption of the metamaterial.

Simulations were carried out in *Comsol Multiphysics* 5.5*a* and were composed of a repeating unit cell containing a SRR pattern with substrate and gold layers as shown in 2.6 a). For these simulations the gold is modeled as a thin film with material properties derived from [114] Above at the top of the cell is a port which serves as to replicate the emission of the THz. This port also measures the THz that is reflected from the metamaterial. A second port that exists below measures the light that is transmitted by the SRR. Figure 2.6 c) shows a side view of the simulation, in this figure the height of the SRR layer is 100 times greater than in normal simulations.

Microcavity simulations were also carried out for work done in section 5.3. The simulation layout is similar to that of figure 2.6 as shown in figure 2.7. The difference here is that the SRR layer and the Gold layer are separated not by a quartz substrate but by a gap of air.

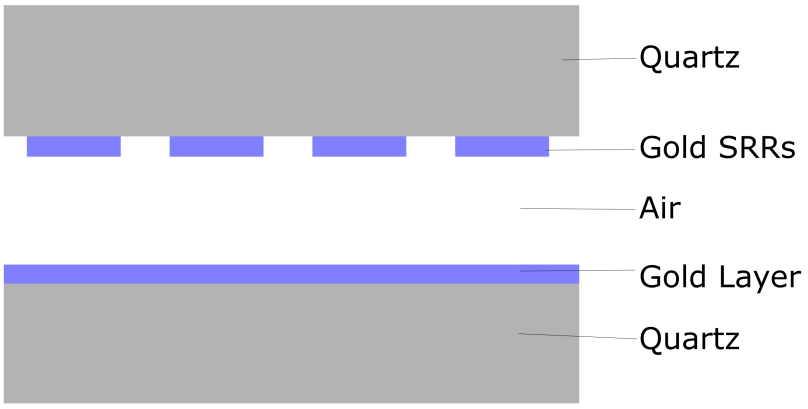

FIGURE 2.7: A side view of the simulated microcavityies. A layer of Gold Split ring resonators is separated from a gold reflector layer by an air gap.

Figure 2.8 b) shows the same ring and substrate as figure a) with a 2 µm layer of gold under the substrate layer. Comparing the two figures shows that with the addition to the gold plate the transmission of the SRR and substrate structure is reduced to zero over the range shown. As the gold plate prevents transmission of the THz, the THz is reflected from the structure apart from when the SRR's are at resonance then the reflection is reduced to 0.05 and the absorption is increased to near unity.

2.3.3 Approximation using Lorentz model

Metamaterial resonances can be approximated using the Lorentz model. The model describes the harmonic motion of electrons around an equilibrium position as a damped oscillator. From the Lorentz model the real and imaginary parts of the dielectric constant of the system can be extracted.

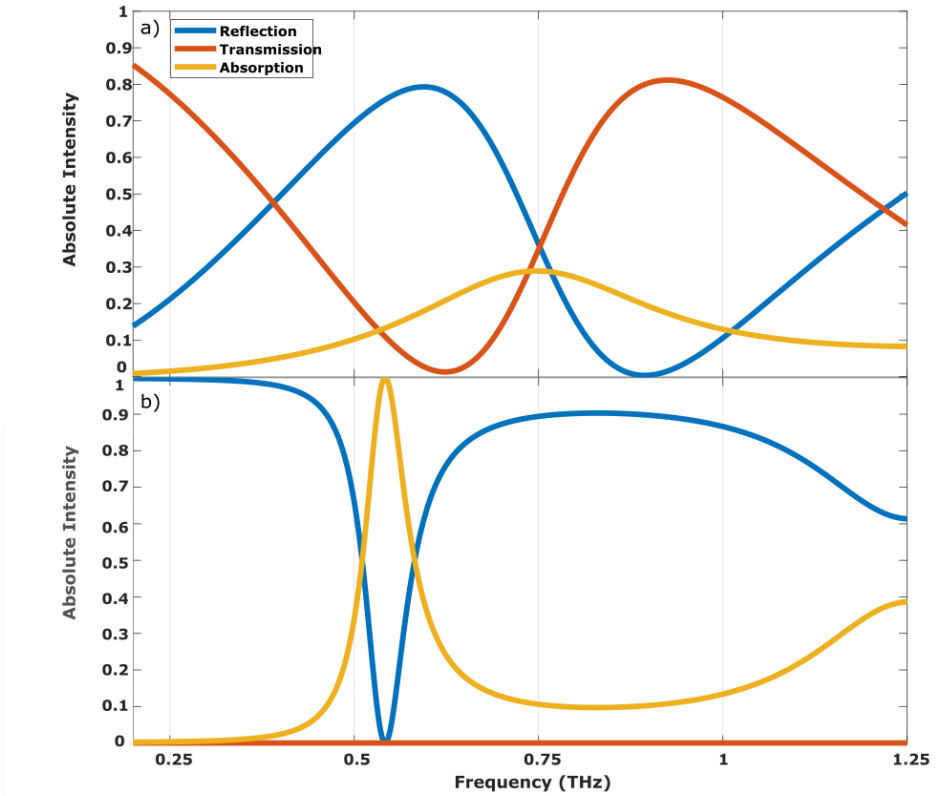

FIGURE 2.8: a) Shows the simulated Absorption, Reflection and Transmission of a square Split ring resonator of side length 45 µm with a ring width and gap size of 4 µm. With a resonance at 750 GHz with a peak absorption of 0.29. The reflectivity and transmission of the SRR fluctuate around the resonance with a peak reflection occurring at 600 GHZ of 0.79 and a peak transmission of 0.81 occurring at 920 GHZ. b)shows the same SRR as a) but with a 2 µm gold back reflector layer 18µm away from the SRR surface. The Transmission for this simulation is zero throughout as the gold layer is thicker than that of the THz skin depth for gold. Because of this zero transmission the Reflection and Absorption of the SRR's are mirrored with a resonance occurring at at shifted frequency of 540 GHZ with a peak absorption of 0.992.

$$\epsilon_r = 1 + \frac{\omega_p^2(\omega_0^2 - \omega^2)}{(\omega_0^2 - \omega^2)^2 + \gamma^2\omega^2} \tag{2.13}$$

$$\epsilon_i = \frac{\omega_p^2\gamma\omega}{(\omega_0^2 - \omega^2)^2 + \gamma^2\omega^2} \tag{2.14}$$

In equations 2.13 and 2.14, ω is the frequency with which the electrons are being driven, ω_p is the plasma frequency of the material. ω_0 is the resonant frequency of the electrons in the system and γ is the damping factor of the oscillation [115] [87]. The resonance of a SRR can be modelled as a Lorentz oscillation. In Chapter 4 the resonance from the metamaterials is fitted to this theory.

2.4 Split Ring Resonator Designs

The SRRs shown in figures 2.9-2.11 have a variety of different shapes and position of gaps and configurations, this variation is shown to change the position, strength, size and number of the resonant responses of the respective rings. The simulations each resonator in these figures have the same width of 45 µm, each gap and the ring depths are 4µm. The resonators are 0.1 µm thick and are modelled on the material properties in [114]. The incident THz in each of these simulations is horizontal across the page.

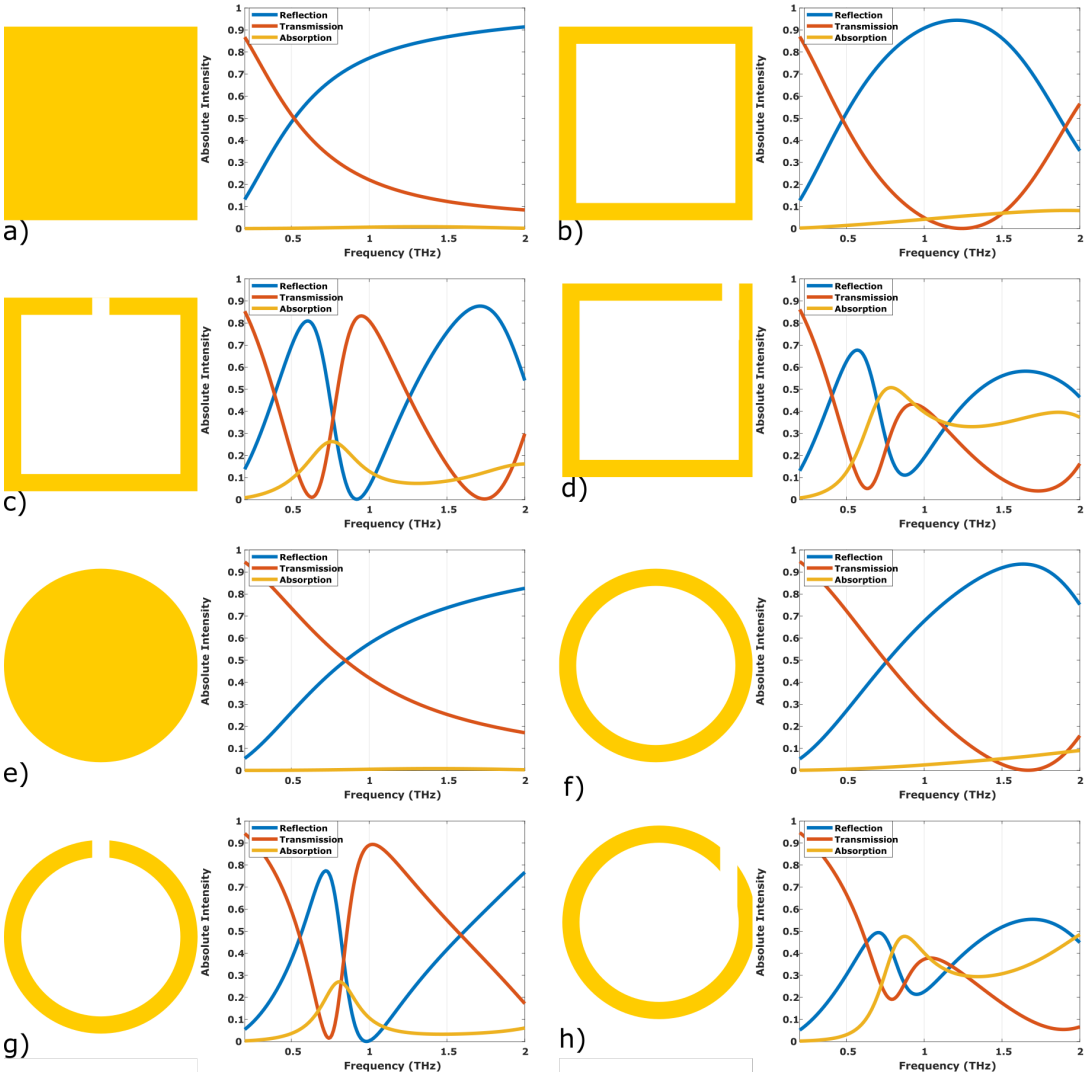

FIGURE 2.9: An array of different simulated split ring resonators. a) is a solid square resonator with width of 45µm. b) is a square ring resonator with a resonator width of 45µm and a ring width of 4µm. c) is the same resonator as in b) but with a gap along the top edge with a width of 4µm. d) is the same resonator as c) but the gap is shifted to the right of the resonators top edge. e) - h) follows the same pattern as a-d) but with a circular resonator instead of a square resonator.

In figure 2.9 a series of simulations are shown of different square and circular resonators. a)-d) shows the resonant responses of square resonators with changing geometries, starting within a solid square ring in a), progressing to a square ring in b), then a square split ring in c) and then a square split ring in d) with a shifted gap. The solid square ring has a broad reflectivity across the simulated region. The square ring has has a broad resonance with a peak reflection at 1.23 THz which ranges across the simulated frequencies. The square split ring has a resonance with a peak absorption at 0.75 THz. The square split ring with a shifted gap has a peak absorption at 0.8 THz, but unlike the square split ring the surrounding peaks in both the reflection and transmission are less prominent and the absorption remains between 30 % and 35 % for frequencies above the resonant frequency. Similarly to figures a)-d), figures e)- h) show a solid circle resonator, a circular ring resonator, a circular split ring resonator and a circular split ring resonator with a shifted gap respectively. The solid circle resonator tends to unity reflection as with the square resonator but at a slower rate than that of the square resonator. The circular ring resonator has a broad resonance like the square ring with a peak reflectivity at 1.63 THz. The circle split ring resonator has a peak absorption at 0.8 THz and the absorption curve is narrower than that of the square split ring resonator. The circular split ring resonator acts very similarly to that of the shifted square split ring resonator with the absorption remaining high at the frequencies above that of the resonant frequency.

In the same progression as figure 2.9, figure 2.10 shows the resonant responses for equilateral(a)-d)) and right angle triangles(e)-h)). a) and e) has responses that have their reflectively that tends towards 80 %. b) and f) increase similarly to a) and e) respectively but the reflectivity in f) reaches a peak at 1.8 THz. c) shows the response of a equilateral triangular split ring resonator has a peak absorption at 1.05 THz and g) shows the right angle triangular split ring resonator with a peak absorption at 0.9 THz. d) shows the equilateral triangle split ring resonator with a shifted gap with a resonance at 0.95 THz, but shows a stronger response than figure 2.9 d) and h). 2.10 h) has the right angle triangle resonator gap on the hypotenuse instead of a shorter edge. The peak absorption at just below 1 THz and increases towards the resonance that is seen in f).

Figure 2.11 has the same resonance progression as figures 2.9 and 2.10 but for pentagonal and hexagonal resonator. Similarly the solid shape resonators (a) and e)) have a reflectively that increases as frequency increases. The ring resonators (f) and b)) also have an increasing reflectivity that increases to a resonance at higher frequencies. The split ring resonators (c) and g)) have very similar responses as the circular split ring resonator in 2.9 g) because the more sides the shapes have the closer they approximate to a circle. d) and g) show the split ring resonators with shifted gaps and have similar responses as c) and g) respectively but with a slightly stronger resonant response.

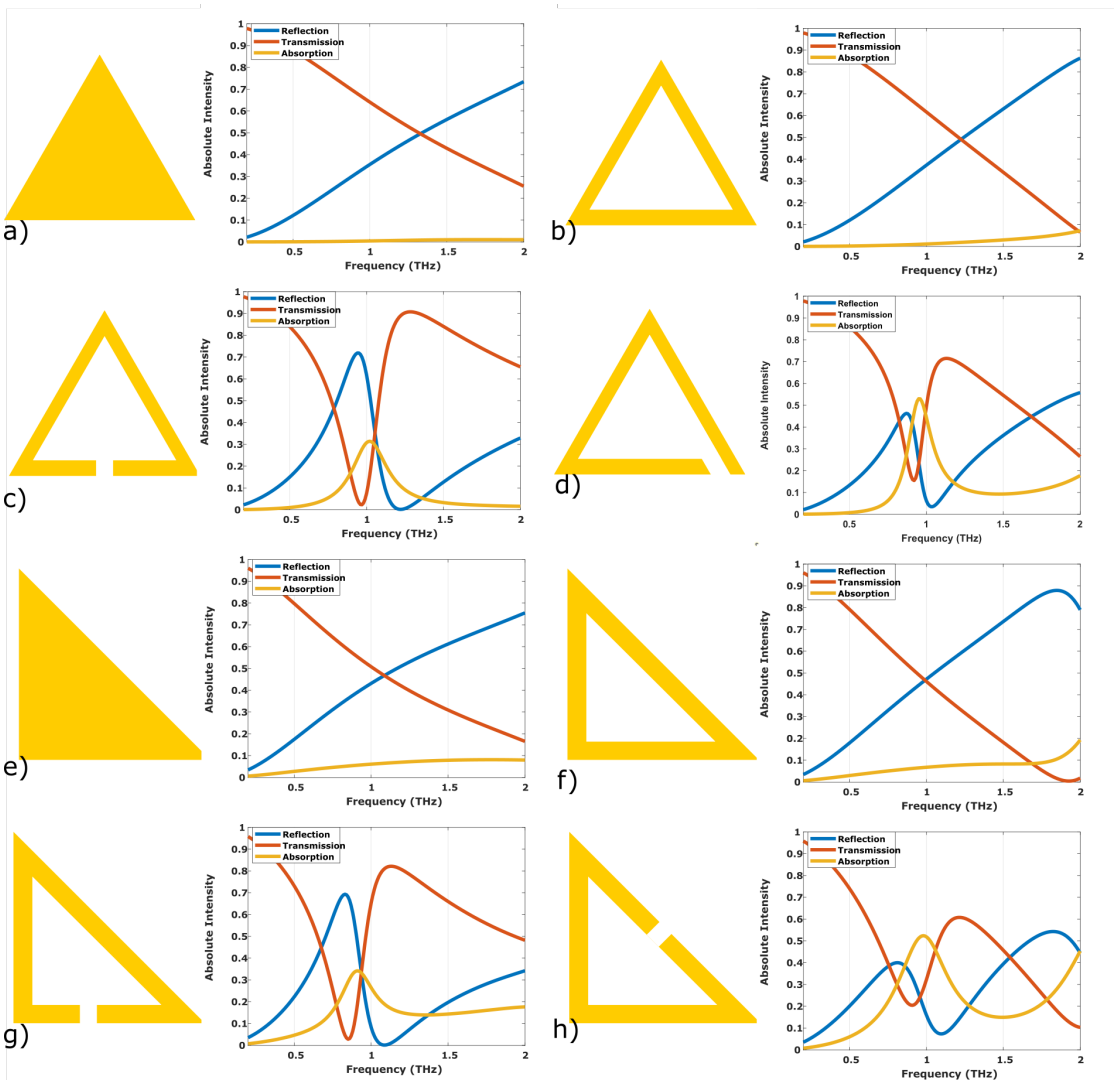

FIGURE 2.10: An array of different simulated split ring resonators. a) is a solid equilateral triangular resonator with a bottom edge width of 45µm, b) is an equilateral triangular ring resonator with a bottom edge width of 45µm and a ring width of 4µm. c) is the same resonator as in b) but with a gap along the bottom edge with a width of 4µm. d) is the same resonator as c) but the gap is shifted to the right of the resonators bottom edge. e) - g) follows the same pattern as a-c) but with a right angle triangle resonator instead of an equilateral triangle resonator. h) is the same resonator as g) but with the gap moved to the right triangles hypotenuse.

Figure 2.12 shows an array of more complex circular resonators. a) is a circular ring resonator with a bar across the middle with a gap in it. The response has broad peak absorption at 1.5 THz. b) is a similar resonator as a) but the gap is made wider with a smaller circular split ring around the gap. The response is stronger and narrower than in a) and has a peak absorption at 1.2 THz. c) and d) show the response of circular rings with six ”spokes” on the outside of the ring, in c) they are evenly distributed around the ring and d) has the spokes evenly distributed across one half of the resonator. Both resonances occur at 0.9 THz and have almost identical reflection and transmission. e) is a circular resonator with a bar across the middle going from bottom left to top right,

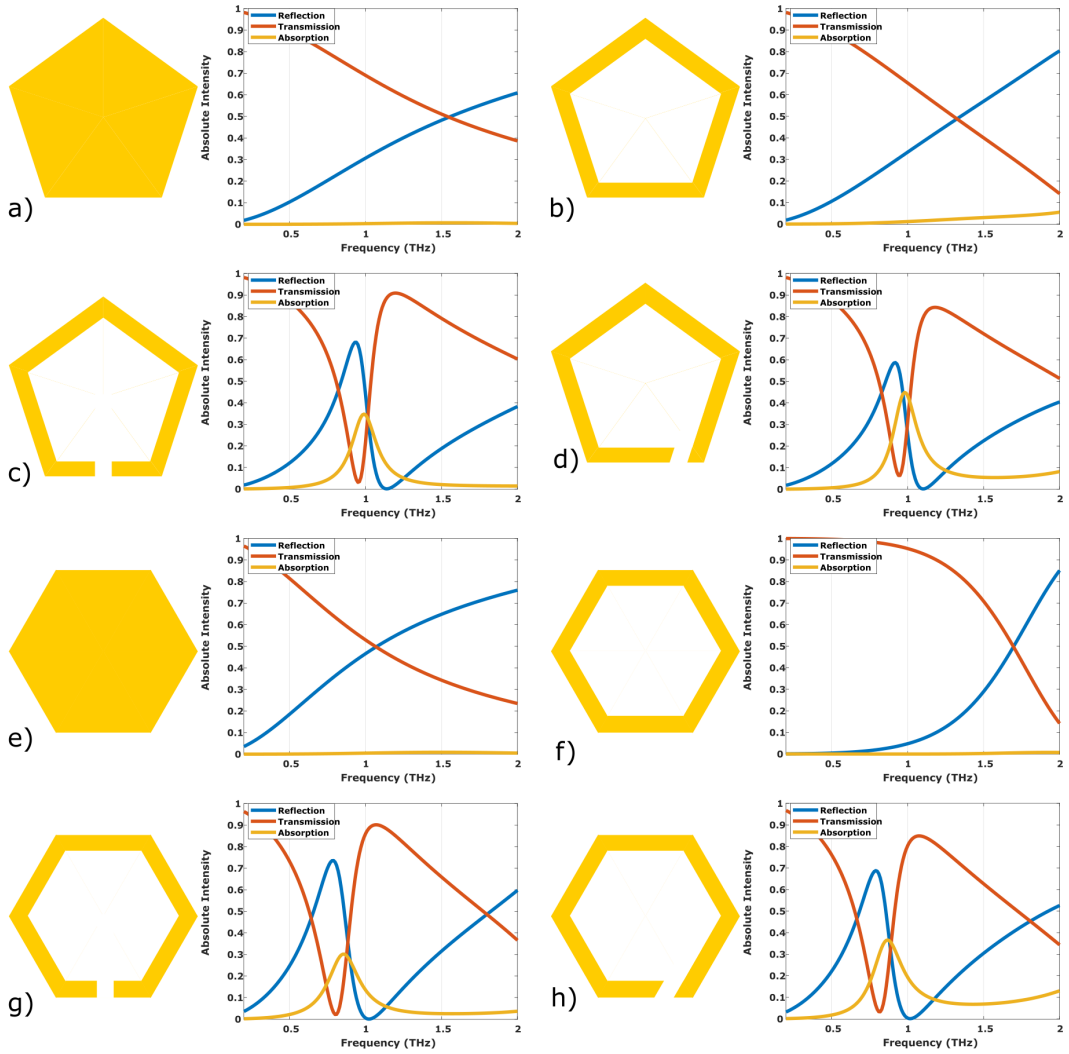

FIGURE 2.11: An array of different simulated split ring resonators. a) is a solid regualr pentagon resonator with width of 45µm, b) is a regular pentagon ring resonator with a resonator width of 45µm and a ring width of 4µm. c) is the same resonator as in b) but with a gap along the bottom edge with a width of 4µm. d) is the same resonator as c) but the gap is shifted to the right of the resonators bottom edge. e) - h) follows the same pattern as a-d) but with a regular hexagon resonator instead of a regular pentagon resonator.

the resonant response is very similar to that of 2.9 f). Figure 2.12 f) is the same resonator as e) but with a gap in the resonator at the top of the circle. The resonant response of this resonator is very similar to those seen for the resonators in sub-figures c) and d) but the absorption falls off at the higher frequencies slower than that of the previously mentioned resonators. sub-figure g) is a similar resonator as e) but it has an additional bar across the circle from top left to bottom right, forming a cross across the circle. The corresponding resonant response is more akin to the solid circle resonator seen in figure 2.9 e) than the circular ring resonators previously shown in this section. Figure 2.12 h) is the same resonator as g) but with gaps in the center of the cross, this creates a response very similar to that seen in sub-figure a).

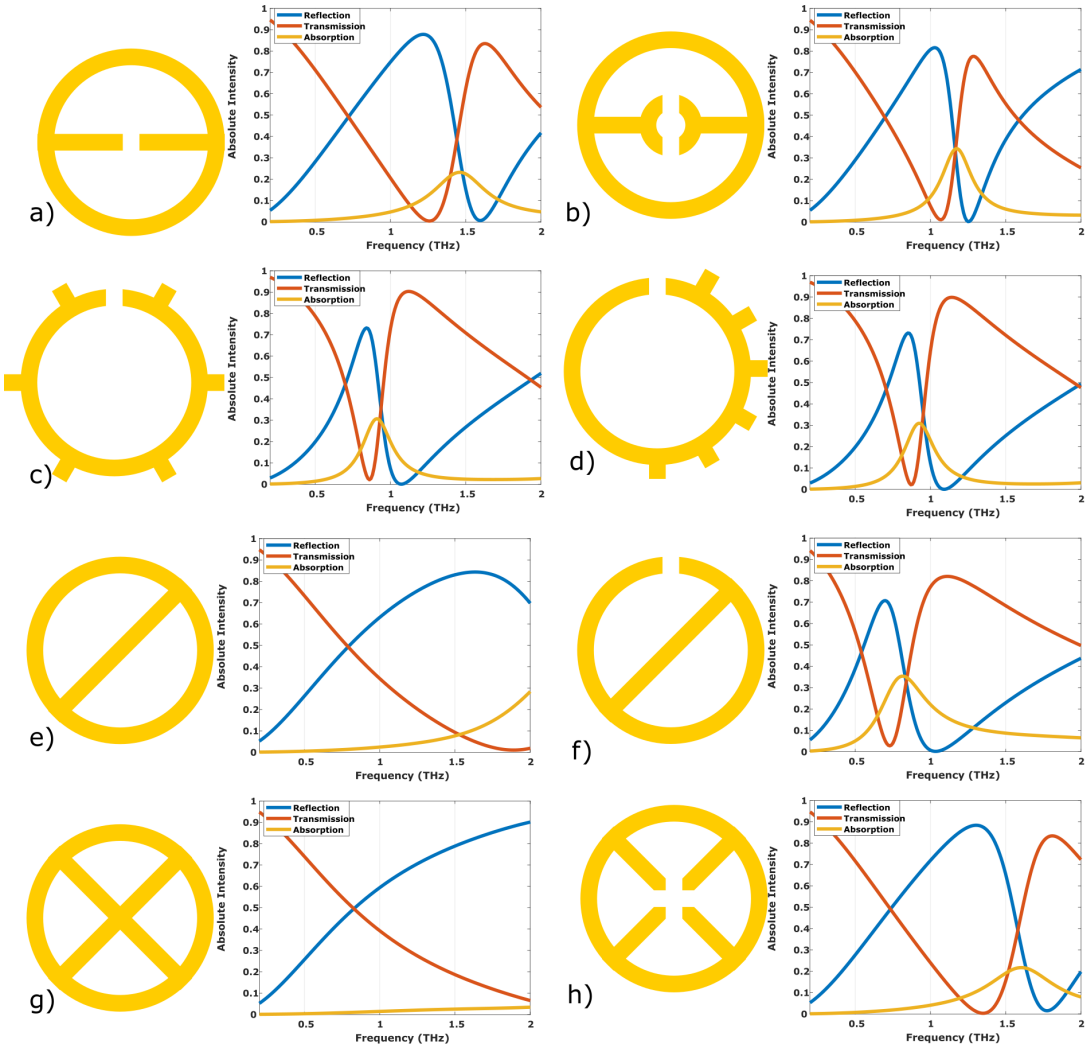

FIGURE 2.12: An array of different simulated split ring resonators. Each resonator is 45 µm wide and the resonators narrowest regions and the resonators gaps are 4 µm wide. a) is a circular resonator with a rod going across the middle of the resonator with a gap in its center. b) is a "poké ball" shaped resonator, it is the same resonator as b) but the rods gap is circular. c) is a circular resonator with six evenly spaced teeth around its outer edge. d) a "robot wars" shaped resonator, similar to c) but all the teeth are on one side of the resonators outer edge. e) is a "stop sign" shaped resonator, a circular resonator with a rod going across the circle at a 45 degree angle. f) is the same as e) but the top of the circle has 4µm wide gap. g) an "X-men" shaped resonator which is the same as resonator e) but with two perpendicular rods at 45 degrees crossing it. h) is the same as g) but the rods have 4µm gaps in their center.

2.4.1 Conclusions

In this chapter I have derived an equation for the resonant response of a split ring resonator based on the inductance capacitance circuit model. . This shows that for a simple resonator design, the resonant frequency is dependant on the square root of the resonators area. Simulations where also carried out to show the charge distributions and induced current within the resonators which serve to show that there is indeed induction and capacitance within the resonator design.

Additionally multiple resonator designs were carried out to help display the effect of the shape and design of the resonator can have on its resonant response. These resonator designs each have there own positive and negative aspects, both in charge distribution and in their response features.

While many of these resonators have stronger or more narrow resonant responses, a square split ring resonator was chosen to move forward with the work going forward. This is due, in part, to limitations in fabrication which reduce the quality of more complicated structures i.e the rounding off of acute corners and a loss of the finer details. Additionally the more simplistic design of the square split ring resonator was chosen as it resonance was more symmetric around the resonance position. While other resonator designs give either a stronger or sharper resonances, the square resonator gives an adequate response and as previously mentioned its simpler design lends itself to less manufacturing errors and rounded out finer details from parts of the fabrication such as photo-lithography.

Chapter 3

Techniques for Terahertz Spectroscopy

3.1 Terahertz Generation and Detection

Methods of terahertz generation come in all shapes and sizes. While there are natural sources of THz such as the interstellar clouds, comets and galaxies, these are not practical in a laboratory setting. To overcome this, multiple man made sources of THz have been developed such as Quantum Cascade Lasers (QCL) and Photo Conductive Antenna (PCA) and as have techniques for its detection. In this section I detail some of them and there positive and negative aspects.

3.2 Photo-Conductive Antennas in a THz time domain spectrometer

There are many methods of THz generation such as photomixing[116, 117], Quantum Cascade Lasers [118, 119], Schottky Diodes[120–122], Photo-Dember emitters [123, 124] and Photo Conductive Antenna (PCA's) [125, 126]. The method used in this work is the Photo Conductive Antenna because it can be used as both a emitter and detector.

Photo Conductive Antenna work by illuminating a semiconductor substrate with photons of a larger energy than the band gap of the substrate of Gallium Arsenide (GaAs)on which the electrodes are attached. For the generation of pulsed THz a pulsed laser with photon energy above the band gap of GaAs is used as the source of the illumination. This illumination creates electrons and holes within the GaAs substrate through photo-excitation. A pair of electrodes that are separated by a small gap are placed on top of the substrate and a bias voltage is applied across them. This voltage accelerates the

newly formed charge carriers and creates a drift current. The accelerated charge carriers emit electromagnetic radiation within the THz spectrum proportional to the rate of change of the current . This is shown in figure 3.1.

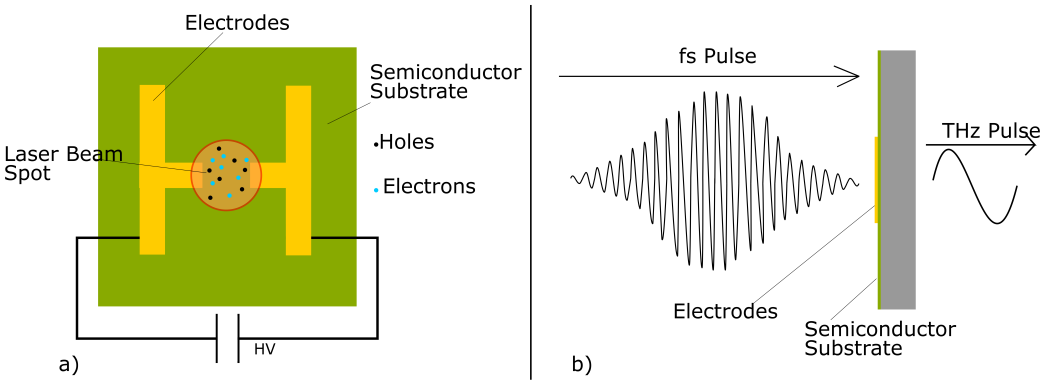

FIGURE 3.1: The geometry of a PCA used for THz pulse generation. Two electrodes are separated by a small gap which is illuminated by a laser pulse which has a photon energy greater than the band gap of the semiconductor substrate on which the electrodes are mounted. This illumination of the substrate creates free carriers which are accelerated by the voltages applied to the electrodes, this acceleration of the free carriers generates Terahertz.

In comparison, when a PCA is used as a detector, the laser pulse and the THz pulse arrive at the antenna together. The Laser pulse generates free carriers as in the emitter but in this case the THz pulse drives the free carriers to create a current which is then measured. The THz pulse created by a PCA is detected by altering the delay stage as shown in figure 3.2, the time between the laser pulse and the THz pulse can be adjusted allowing the detector to measure the current at different times of the THz pulse. This is because the strength of the induced carriers within the detector is dependant on the overlap of the two pulses. [127].

PCAs can also be used to create continuous wave (CW) THz through the process of photo-mixing. Photo-mixing is the combination of two separate CW lasers with frequencies of ω_1 and ω_2 to create THz frequencies as shown in equation 3.1 [128]. The PCAs used in photo-mixing have an altered electrode pattern in the shape of a spiral. Photo-mixing uses the beating of the two different frequencies of the CW lasers. [129, 130].

$$\omega_{THz} = \omega_1 - \omega_2 \tag{3.1}$$

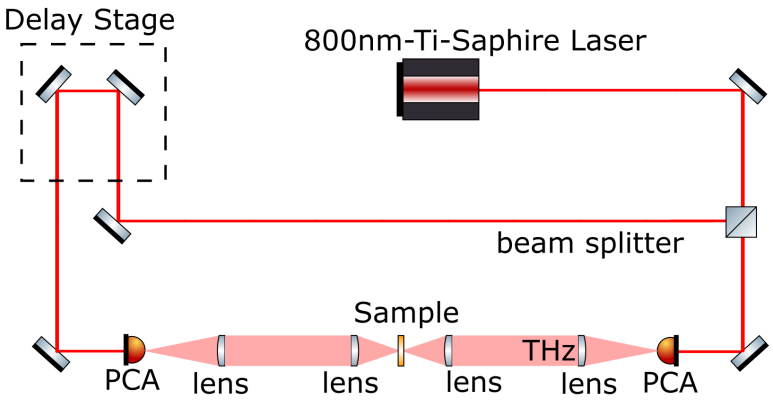

FIGURE 3.2: Setup for time domain spectroscopy(THz TDS). A 800nm Ti-Sapphire laser with a repetition rate of 60 MHz is radiant upon two PCAs. The first PCA has a bias voltage applied and serves as a THz emitter, the second PCA serves as a detector and generates a current when both the Ti-Sapphire laser and the THz are both incident upon it.

3.3 Quantum Cascade Laser

A Quantum Cascade Laser (QCL) is a variation of semiconductor laser which operates on the subband transitions of the semiconductors energy bands instead of between the energy bands themselves. A QCL operates similarly to a standard laser such that it emits electromagnetic radiation from the transition of electrons from high energy states to lower energy state. The subband structure of a semiconductor can be viewed as a series of quantum wells, each of these quantum wells contains energy states and these are the states from which stimulated emission occurs. Figure shows a simplified diagram of QLC energy level transitions. Firstly an electron in injected into the higher level quantum well where it transitions to a lower energy level and emits a photon. Afterwards it undergoes a non-radiative transition to the lowest energy level within the quantum well then tunnels to the higher energy state of the adjacent quantum well and repeats the cycle [131–133].

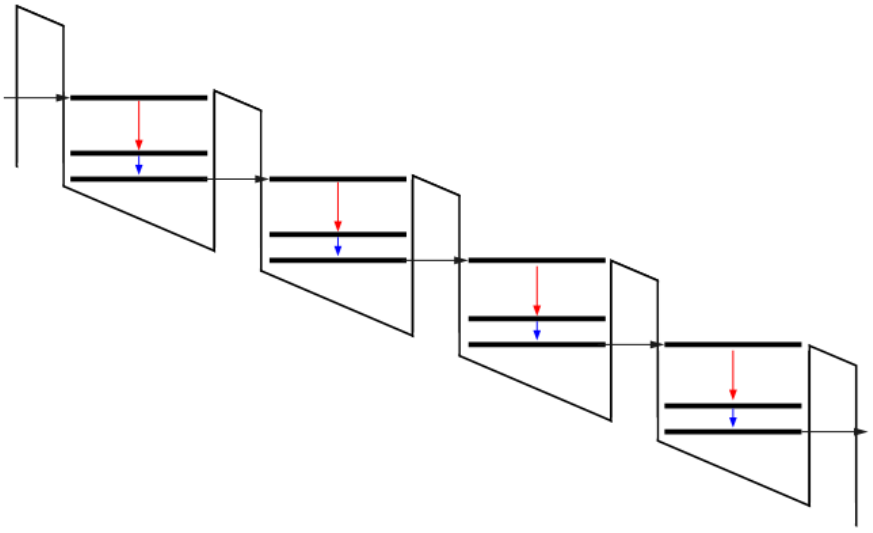

FIGURE 3.3: Energy level diagram for a Quantum Cascade laser. A electron is injected to the higher energy state of a quantum well which then decays to a lower level and emits a photon, as in a regular laser. The electron then under goes a non-radiative decay to the lowest level in the quantum well before tunneling into the adjacent well and repeating the cycle.

Through the application of an electrical field the quantum wells are offset from one another an allow for the quantum tunneling from one well to the other to occur, causing the cascade effect which the QCL gets it name.

The output of a QCL is highly dependant on the temperature, typically in the 50-100 K range but have been shown to work at temperatures as high as 164K [134], and design of the semiconductor used as a gain medium. QCL's are typically CW but can operate pulsed and are very narrow bandwidth. [135]

3.4 Pockels cell for THz detection

Pockel's electro-optic effect, describes the change or generation of a birefringent effect within a material under the influence of an electric field. A Pockel's cell is this effect applied to create a electrically controlled waveplate that causes a phase shift that is proportional to the electric field applied. In the case of detection, the electrical field that induces the Pockel's effect is the electric field from the Terahertz pulse itself. Hence, by passing laser light and pulsed through the crystal within the Pockel's cell, such as Zinc telluride, lithium niobate or cesium telluride, the polarization change of the laser light is proportional to the strength of the electric field. After this the pulsed light passes through a polarization dependant prism such as a Wollaston prism [136, 137] which splits the light into it's constituent ordinary and extraordinary parts. Using an experimental setup with a variable delay stage such as figure 3.4, the overlap of the THz pulse and the laser pulse can be changed such that the laser pulse probes different time intervals of the THz pulse's electric field and can be used to build an image of the THz pulse in time.

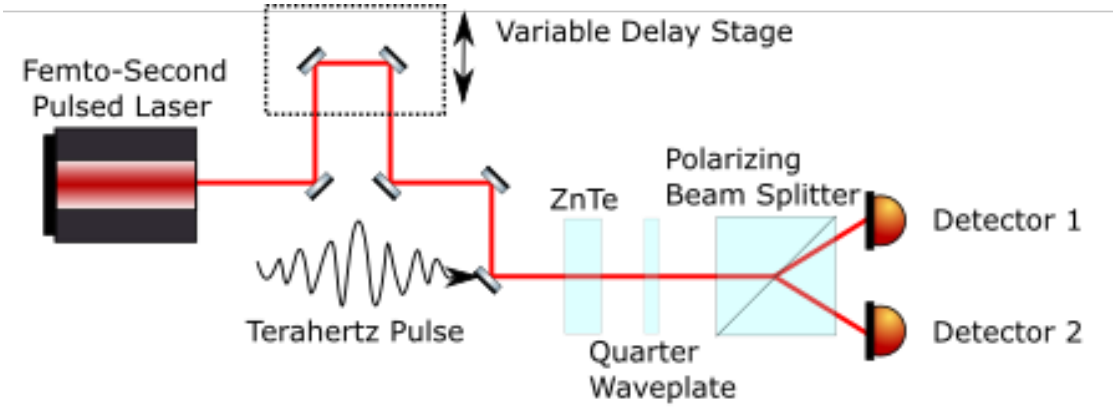

FIGURE 3.4: The experimental set up for the application of a Pockel cell. A femto-second pulsed laser is directed towards a material with a known linear electro-optical response, such as Zinc Telluride (ZnTe), through a variable delay stage such that is parallel to a terahertz pulse. The electric field of terahertz pulse changes the birefringent properties of the medium that it and the femto-second pulse pass through. After passing through the ZnTe the pulsed beam passes through a quarter-wave plate and a polarising beam splitter, such as a wollaston prism, which splits the beam into two opposing polarisations who's relative power is compared by detectors one a two. The difference in the power of the two detectors is proportional to the strength of the THz electric field By moving the variable delay stage the overlap between the terahertz pulse and the femto-second pulse can be altered such that the femto-second pulse interacts with a different part of the terahertz pulse's electric field allowing for a measurement of the terahertz pulse in time.

3.5 Golay Cell Detector

Golay cells use a sealed cavity containing a gas with a low thermal conductivity, with a membrane at one end and a THz transmissive window on the other. A material with high absorption at the desired THz frequency is placed within the gas which allows for the transferal of energy between he THz radiation to the gas. The energy from the absorber is thermally deposited into the gas filled cavity, thus causing the gas to heat up and thermally expand. This expansion causes a displacement of the membrane. By reflecting light from the membrane, the displacement of the membrane is seen as movement of the reflected light on a photo-detector. Figure 3.5 shows the layout of a Golay cell [93, 138]. A Golay cell allows for the detection of electromagnetic radiation that is absorbed through the absorbing medium within the gas filled cavity. By creating an absorber layer with a very narrow and/or controllable absorbtion spectrum, the Golay cell can be used for spectroscopy of that spectrum.

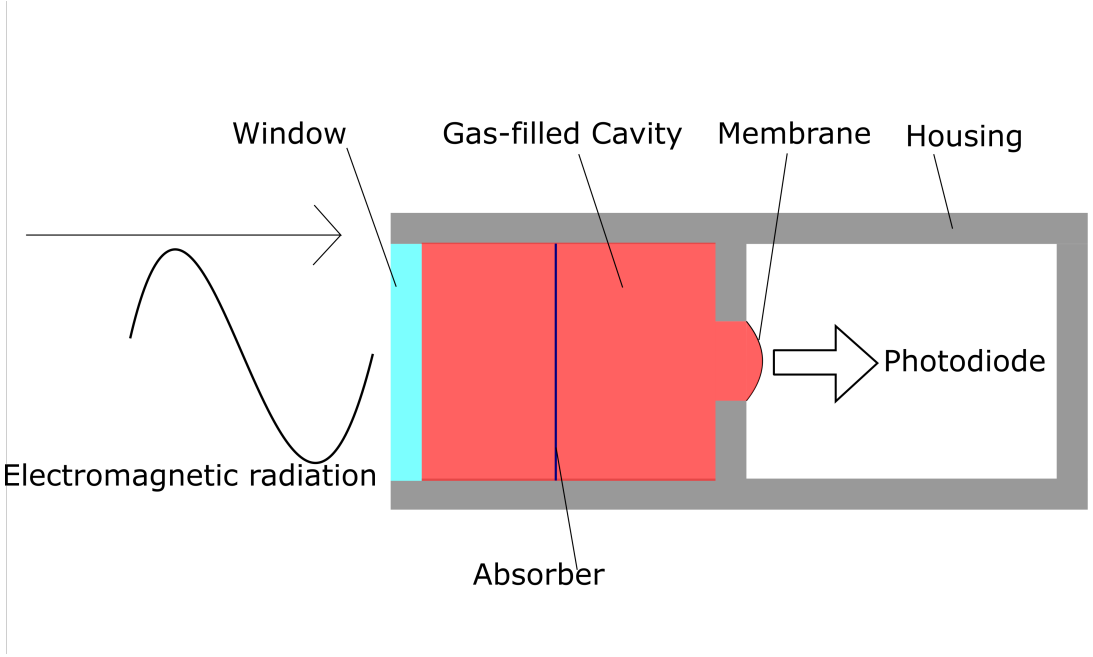

FIGURE 3.5: The structure of a Golay cell. A window is used to let electromagnetic radiation into a gas filled cavity which contains an absorbing medium. The absorbing medium then emits the absorbed energy as thermal radiation, this causes the expansion of the gas in the cavity. The gas expansion causes a translation of the membrane. The translation of the membrane deflects light on a photodiode which can be used as a measure of the gas expansion and energy absorbed. By making an absorbing layer with a narrow absorption spectrum that can be shifted to higher or lower frequencies, the golay cell can be used for spectroscopic measurements.

3.6 Conclusions

While multiple methods for THz detection and generation exist, they each have their own positives and negatives. For this work I will predominantly be using photo conductive antennae as they serve well as both emitters with a broad pulsed emission spectrum and detectors. Additionally a Pockel cell will also be used as a detector due to the equipment used in parts of the work have the pockel cell built in.

While a QCL could be used as a THz source for this work, they have a very narrow bandwidth and require very cold working temperatures and so are less suited to the work.

Chapter 4

Development of split-ring metamaterials and their THz spectroscopy

4.1 Introduction

In this chapter I present experimental results on the fabrication and spectroscopy of gold split ring metamaterials. The first section presents the fabrication of the devices using photolithography done in the Zepler Institute cleanroom. Subsequently the construction of the THz time domain experimental setups used in this thesis is discussed. Different setups were developed for measuring reflection and transmission of the materials. We discuss experimental results and particularly look at different ways of obtaining reference spectra including a new approach for self-referencing using echos in the time-domain traces.

4.2 Fabrication of THz split-ring metamaterials

Split ring resonators were created using lift-off Photo-lithography, the details of which are below. Fabrication of the SRRs was assisted by Sun Kai from the University of Southampton who taught me the method for the fabrication.

The first stage of the fabrication is to spin the photo-resist onto a sample of Quartz that the SRRs are to be made on. The photo-resist used is AZ2070. The AZ2070 is warmed to room temperature and then spun onto the sample using a spin coater at $6000rpm$ for forty seconds with a ramp speed of $3000rpm/s$. Then the sample is baked at 110^0C for one minute on a hot plate. After this the sample is exposed to UV radiation using the

photo mask aligner. A hard-contact between the sample and photo-mask is used to get the 4 μm details of the mask's pattern. The sample is exposed to a dose of $75mj/cm^2$ of UV which chemically alters the exposed photo resist. After the exposure the sample is baked for another minute at 110^0C. After the second bake the sample is developed in AZ725 MIF developer for eighty five seconds to remove the altered photo resist and then cleaned with DI water and then dried using compressed air. Once this is done the AZ2070 forms a layer that covers the sample with holes where it was exposed to UV.

Once the sample is dried it is transferred to the evaporative deposition chamber. The chamber is loaded with Gold and Chromium pellets and pumped down to $2*10^{-6}mbar$. Once the chamber is pumped down the metal pellets are heated using an applied current which causes the metal to eject atoms into the chamber onto the sample. using this method $5nm$ of Chromium is deposited followed by $100nm$ of gold. This process coats the sample of AZ2070 with the hole pattern with a layer of Chromium and a layer of Gold. The Chromium layer bonds the Gold and Quartz layers

To remove the remaining AZ2070 a stripper called Technistrip N1555 is used. The sample is left in a bath of Technistrip over night and then washed in DI water. The remaining pattern of Gold and Chromium on the sample is the negative of the pattern from the photomask. Figure 4.1 shows the stages of the sample though different stages of fabrication. The produced resonator arrays are square with a side length of two centimeters.

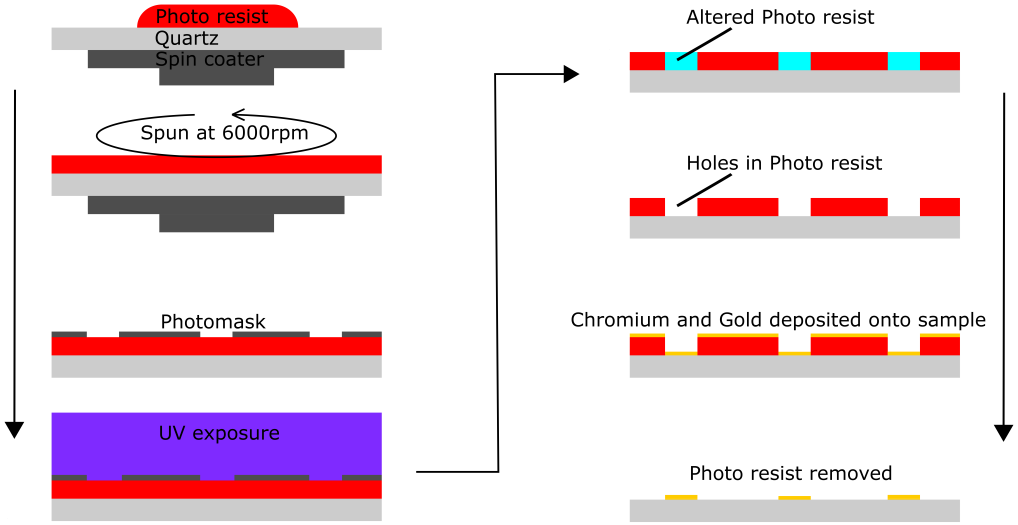

FIGURE 4.1: Fabrication process of the split ring resonators. Starting with deposition and spinning of the photoresist and then followed with the alignment of the photomask and exposure of UV to alter the photo resist. The next steps show the removal of the altered photoresist and the deposition of the Chromium and Gold followed by the removal of the photo resist. The final product is a quartz slide with an array of split ring resonators.

In figure 4.2 the additional fabrication steps used to fabricate a fixed microcavity as seen in section 5.1. Micro beads of a given size, in this case 7 μm and 12 μm separately, are applied to the corners of a quartz slide with a 400 μm layer of gold deposited on it. The beads are contained within a UV curable adhesive. A quartz slide is then placed atop the beads with the split ring resonators and the gold layer separated by a an air gap. The newly made fixed microcavities are the cured with UV light for two-three minutes. Once the exposure is complete, the fixed microcavity samples are done.

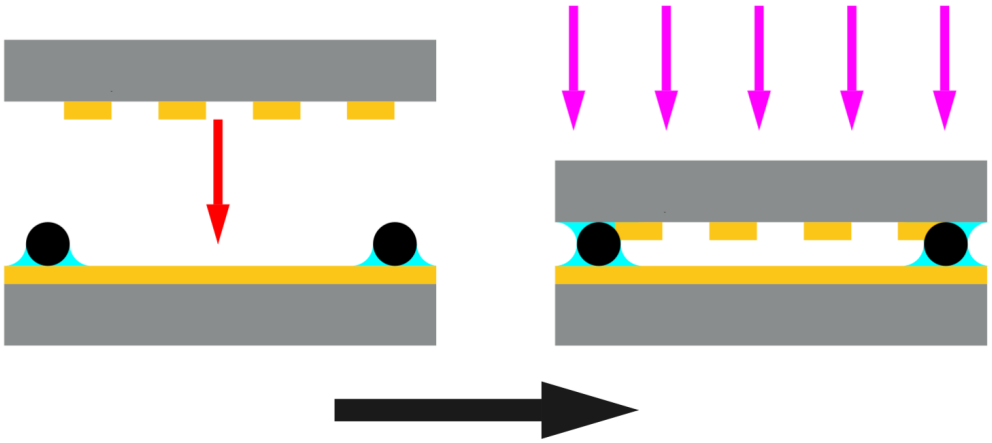

FIGURE 4.2: The fabrication steps used to fabricate a fixed microcavity which is discussed more further in the work. Micro beads of a given size are applied to a quartz slide with a layer of gold deposited on it. The beads are contained within a UV curable adhesive. A quartz slide is then place atop the beads with the split ring resonators and the gold layer separated by a an air gap. The newly made microcavities are the cured with UV light for two-three minutes.

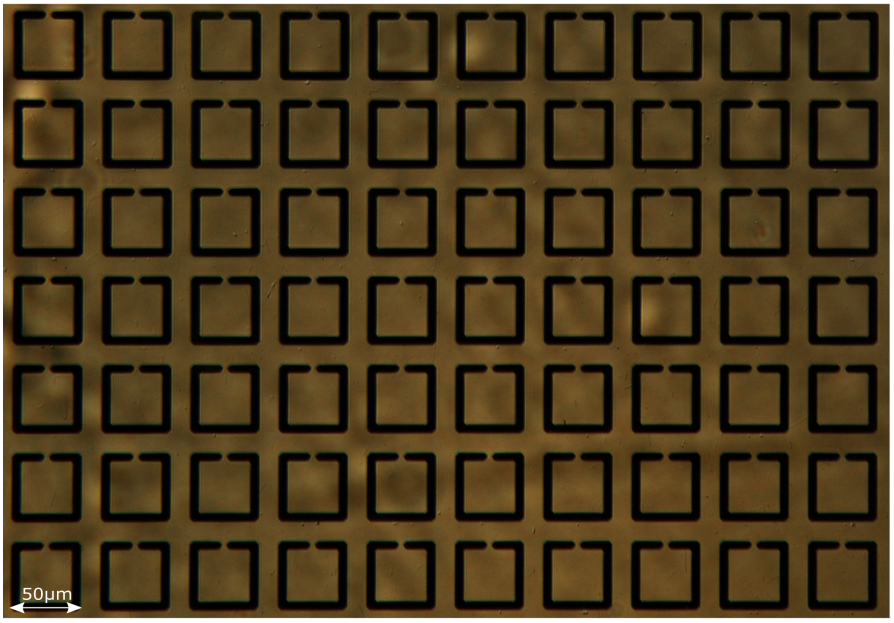

FIGURE 4.3: A back lit image of an array of SRRs with a side length 50 μm and a gap and width size of 4μm in a repeating grid pattern with a spacing between the SRRs of 20 μm.

Figure 4.3 shows a microscope image of the resonators. Figure 4.4 shows an SEM image of a set of resonators of side length 50 μm and a gap and width size of 4μm. The images in figure 4.3 and 4.4 show that the the resonators form a repeating pattern.

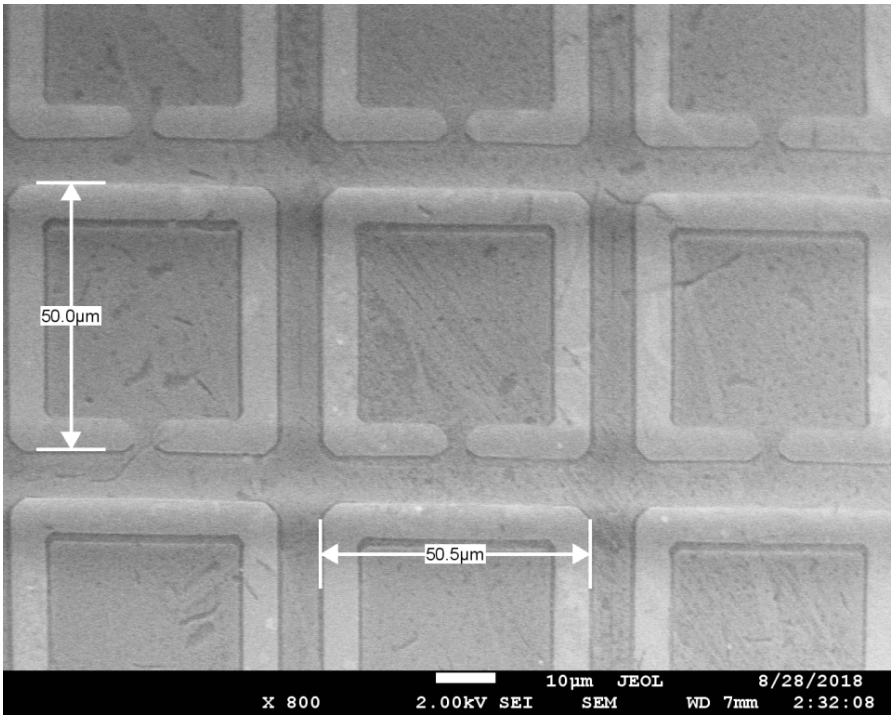

FIGURE 4.4: SRRs of side length 50 μm and a gap and width size of 4μm in a repeating grid pattern with a spacing between the SRRs of 5 μm.

4.3 Construction of the THz time-domain spectroscopy setup

Terahertz time domain spectroscopy (THZ-TDS) is a spectroscopic method used for the measurement of the effect on THz as it passes through a material or object. Figure4.5 shows a typical THZ-TDS set up. A pulsed Ti:Sapphire 800nm laser with a repetition rate of 60 *Hz* and a pulse duration of 80fs is radiant upto a PCA which emitts pulsed THz as described in ?? and is collimated through a lens onto through the air, into a sample and then collected by a second lens and focused onto a second PCA. The second PCA is also irradiated by the Ti:Sapphire laser, creating electron hole pairs that are accelerated by the THz electric field. Through the use of a variable delay stage the overlap of the THz pulse and the 800nm pulse can be changed allowing the 800nm pulses to probe different parts of the THz pulse due to the THz pulse having a pulse duration of 2ps compared to the Ti:sapphire's 80fs.

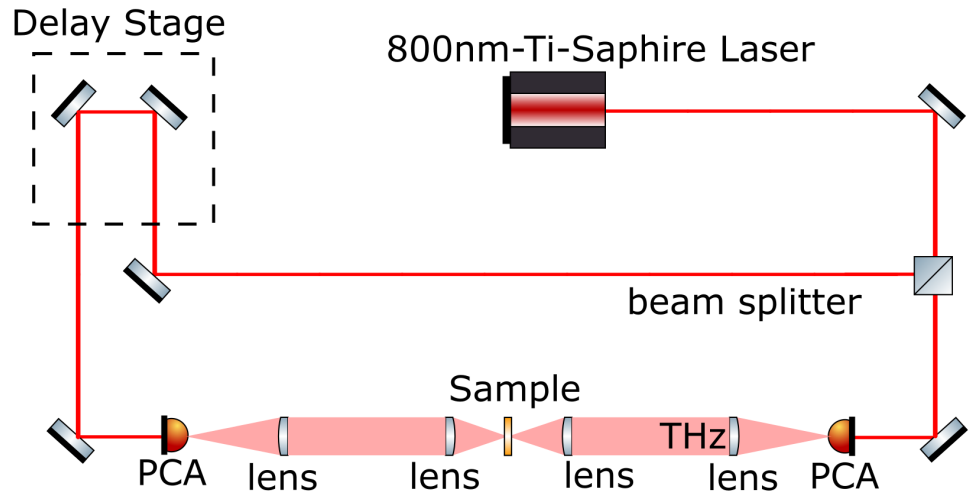

FIGURE 4.5: Setup for time domain spectroscopy(THz TDS). A 800nm Ti:Sapphire laser with a repetition rate of 60 *Hz* is radiant upon two PCAs. The first PCA has a bias voltage applied and serves as a THz emitter, the second PCA serves as a detector and generates a current when both the Ti:Sapphire laser and the THz are both incident upon it.

4.4 Experimental Set-ups

The metamaterial designs they are placed within a THz-TDS set-up for testing. This will allow a Fourier transform to be applied in order to find the absorption of the meta-material. Firstly the SRR will be tested in a transmission set-up. As shown in figure 2.8 the SRR layer an absorption peak at the resonance. By testing the SRRs on a trans-mission set-up it should be possible to see this resonance within the Fourier Transform.

The set-up for a THz-TDS is shown in figure 4.6 for the SRRs the transmission set-up will be used. The SRR sample is to be placed at the sample point in the set-up which will allow the Transmission spectrum of the SRR to be analysed.

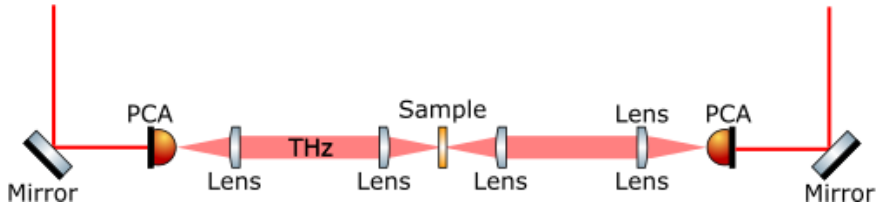

FIGURE 4.6: Beam line for THz-TDS set up, PCA's used as THZ detector and emitter. THz is focused onto the sample through a lens, collimated after the sample and then focused down on to the detector.

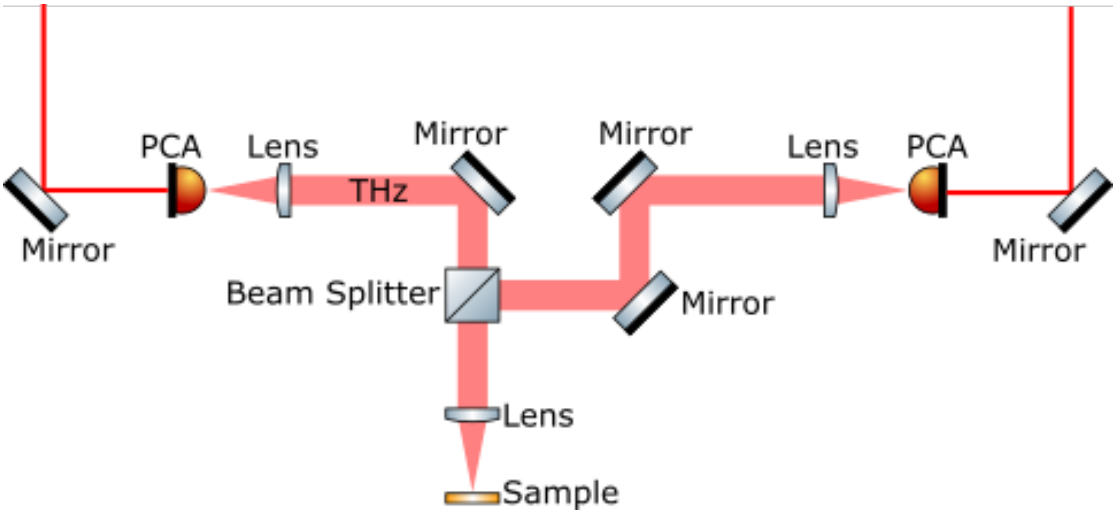

FIGURE 4.7: Beam line for THz-TDS reflection set up, PCA's used as THZ detector and emitter. THz is focused onto the sample through a lens through a beam splitter, then focused onto the sample. The THz is reflected off of the sample back through the beam splitter where it is directed towards the detector PCA.

Figure 4.7 shows the set up for a THz-TDS reflection set up. This set up measures the THz that is reflected off the sample compared to figure 4.6 which measures the transmitted THz. By finding the reflected and transmitted light, the absorption spectrum can be found.

4.5 Transmission

Using the THz-TDS set up shown in figure 4.6 the transmission of THz-SRRs was tested. In order to measure the change in transmission across the THz frequencies and in order to see the response of the SRRs at their resonance, two measurements are required. The first measurement is the THz pulse through a quartz plate, the second is a measurement of the THz pulse through a quartz plate with an SRR layer. By comparing the Terahertz spectrum of these two measurements the transmission of the sample can

be found. Figures 4.8 and 4.10 show the THz pulse and corresponding Fourier transforms of THz through free space and a sample. The sample used is a pattern of square SRRs with side length of $50\mu m$ with a gap and width size of $4\mu m$ as shown in figure 4.3. In figure 4.8 there is a noticeable reduction in the amplitude of the pulse from the free space reference pulse to the sample pulse, this reduction due to not all the THz being transmitted by the SRRs. This is shown more clearly in figure 4.10 which shows the logarithmic amplitude of the Fourier Transformation of THz pulses from figure 4.8, It is seen in figure 4.10 that there is a reduction in the transmission of the THz through the sample at around 0.7 THz.

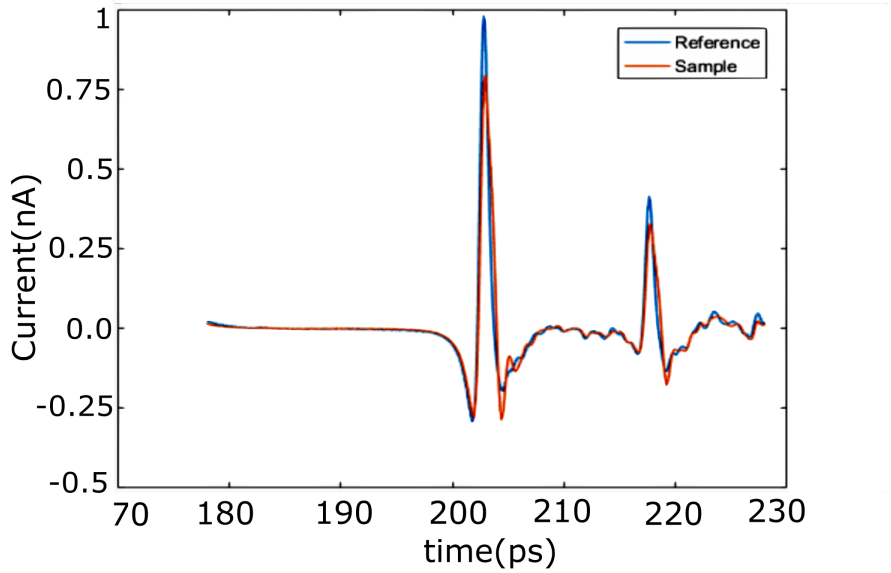

FIGURE 4.8: Shows the Terahertz a pulse through free space and through SRRs. The amplitude of the pulse is changed in the sample pulse with respect to the reference pulse, The second pulse is a etalon effect caused by the emitter.

Figure 4.9 shows the Transmission spectrum and phase shift of the THz through the SRRs shown in figure 4.3. The centre of the resonance at just below 0.7 THz corresponds to the minimum transmission through the SRRs and the steepest part of the phase change of the THz as it passes through the SRRs.

In order to measure the effects of the THz polarization on the SRRs, the SRRs were rotated perpendicular to the THz. Figure 4.11 a) shows the effect of rotating the SRRs with regards to the THz polarization. When the SRRs are aligned at 0 degrees like that as shown in figure 4.11 b) the THz does not interact with the SRR gap, but treats the SRR as a ring resonator (RR) which has a resonant frequency of twice that of the SRR, this can be seen in 4.11 a) where the 0 degree line transmission is dropping as the frequency increases. When the SRR is rotated as shown in 4.11 c) the THz interacts with the gap which induces the electric field across the gap, creating a capacitance which causes the

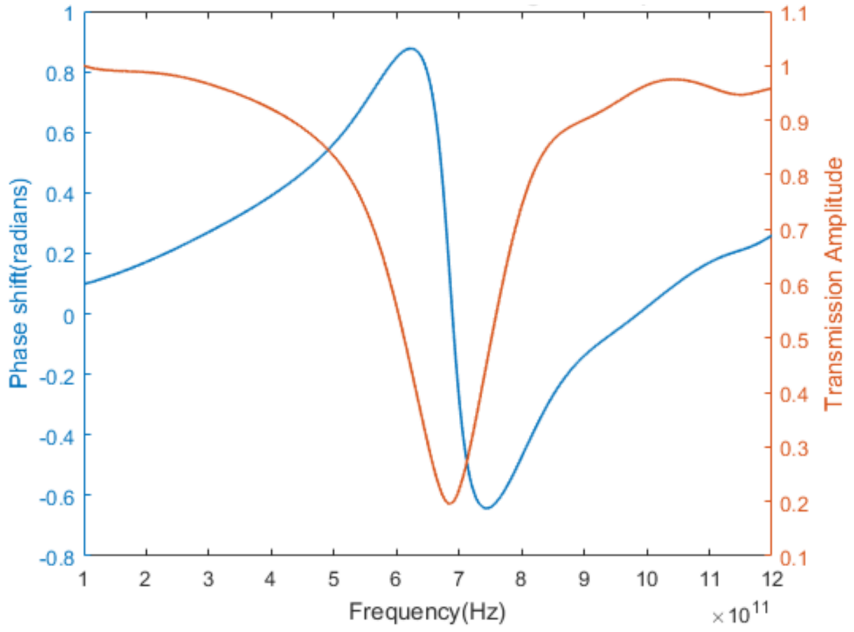

FIGURE 4.9: The terahertz transmission of the SRRs, It shows that there is a drop to 0.2 transmission of the Terahertz at the resonance position of the SRRs and a phase shift of 1.5 radians through the resonance. The minimum of the transmission and the centre of the phase change occur at near 0.7 THz.

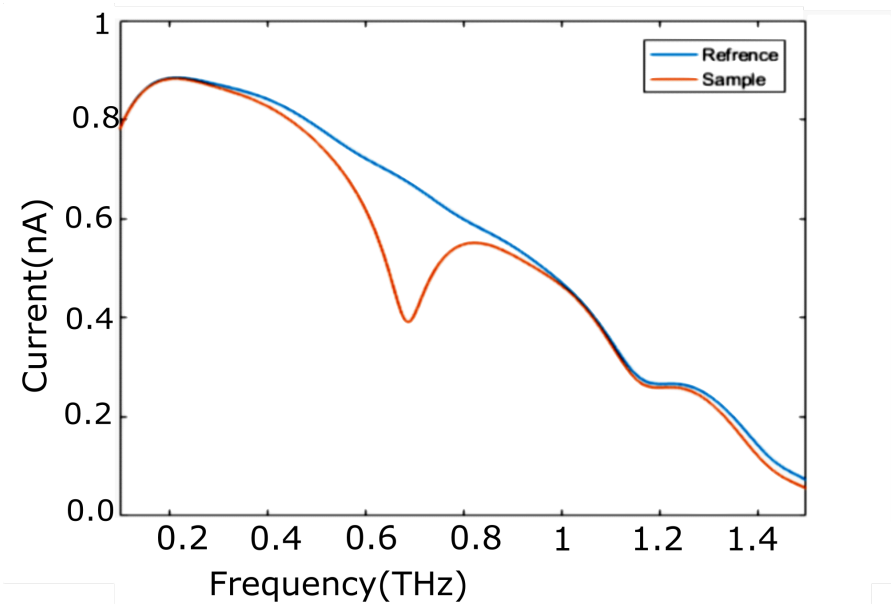

FIGURE 4.10: Shows the corresponding logarithmic Fourier transforms of the sample and reference pulses, it is clear to see the position of the SRRs resonance at close to 0.7 THz.

SRR resonance instead of the RR resonance. At orientations between 0 and 90 degrees there is a resonance response from the SRRs but it is reduced.

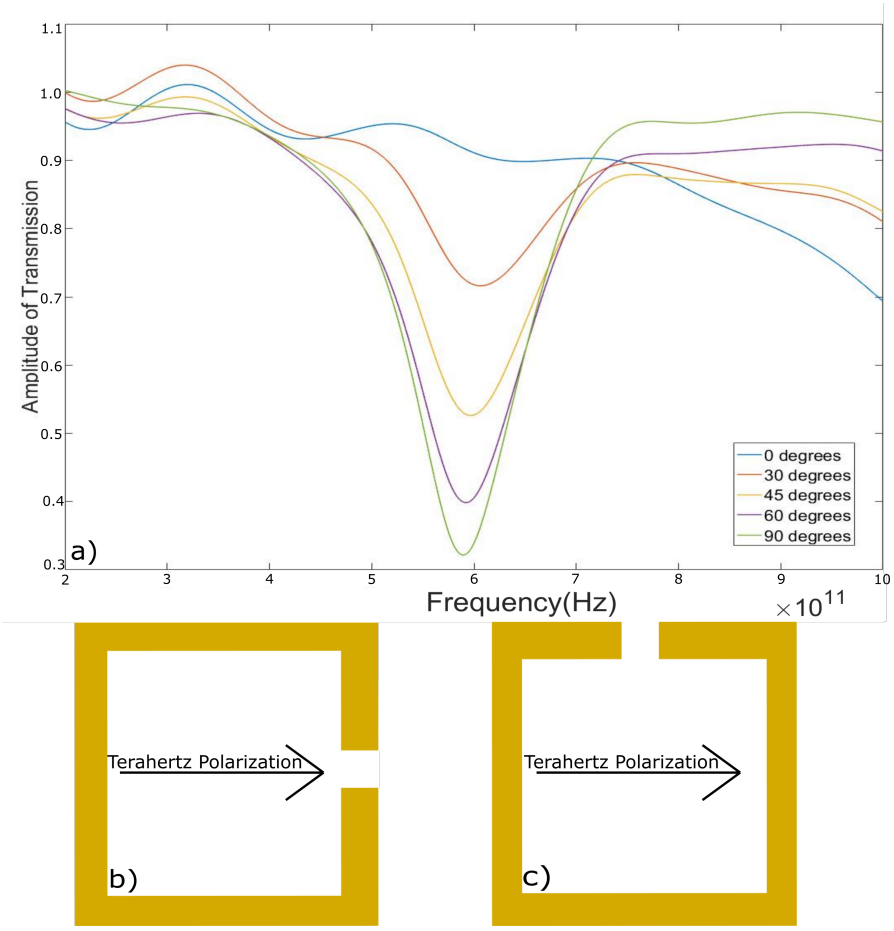

FIGURE 4.11: Figure a) shows the change in the transmission spectrum of the THz through the SRRs at different orientations with regard to the THz polarization. As the SRRs are rotated from 0 to 90 degrees, the strength of the resonance increases which is shown by the drop in the transmission at the resonance. Figure b) and c) shows the orientation of 0 and 90 degrees of the SRRs compared to the THz polarization which is shown by the black arrows.

4.6 Data Analysis

4.6.1 Initial Pulse Analysis

In order to extract the transmission of THz through the SRRs the measured Time domain pulse has to be converted to a frequency spectrum through a Fourier transform. Figure 4.12 a) shows a Time domain THz pulse and b) shows the corresponding frequency spectrum. The repeated sinusoidal features of the frequency spectrum are due to the etalon effect created by reflections from the THz emitter. Figure 4.12 c) shows a window that is applied to the time domain pulse, this window serves to remove the data that is far away from the peak of pulse and in doing so removes the reflected pulse and the etalon effect. Figure 4.12 d) shows the THz frequency spectrum before and after the application of the window, comparing the two shows that the overall amplitude remains the same and the sinusoidal etalon is removed. The window can be controlled in both the width of the window and how steeply it approaches zero, by changing the window the time pulse can be sculpted to remove the etalon effect without loosing important information. The window size and shape that were selected were chosen to remove the secondary from the data and leave only the initial pulse which in turn removes the etalon effect shown in figures 4.12.

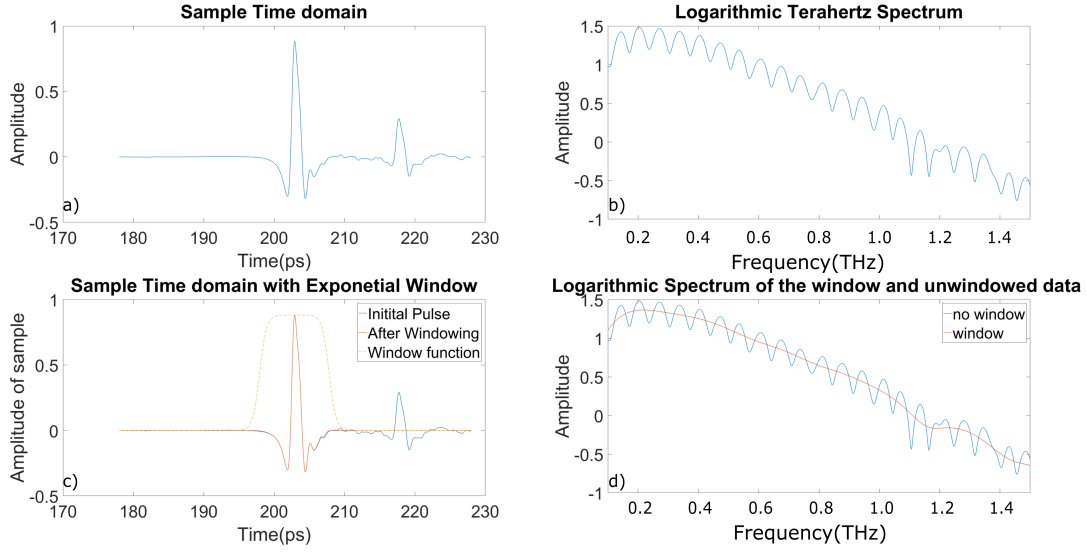

FIGURE 4.12: a) Shows a the time domain of a THz pulse and b) shows its corresponding frequency spectrum. c) is the original spectrum with a window function applied to remove the reflection pulse which causes the etalon effect seen in b. d) shows the comparison of the frequencies of the time pulse before and after the application of the window function. The window size shown here is representative of the window use in the transmission setup. For the reflection setup used in later sections the window can be made larger due to the separation between the initial and secondary pulses being much greater.

When the Fourier transform is performed on the Time pulse, not only is the THz spectrum retrieved but the phase of the THz is also extracted. By taking the difference of the phase from the THz that passes through our reference and our sample, the phase shift of the THz at the resonance can be found. The size of the phase shift gives an indication of the strength of the resonance.

In order to find the position of the resonance more accurately, the phase and transmission of THz at the resonance can be fitted to the Lorentz model as shown in section 2.3. By fitting equations 2.13 and 2.14 to the phase and transmission of the THz through the SRRs, the position of the resonance can be found. Figure 4.14 shows the transmission and phase as shown in figure 4.13 but with fitted curves from equations 2.13 and 2.14 respectively.

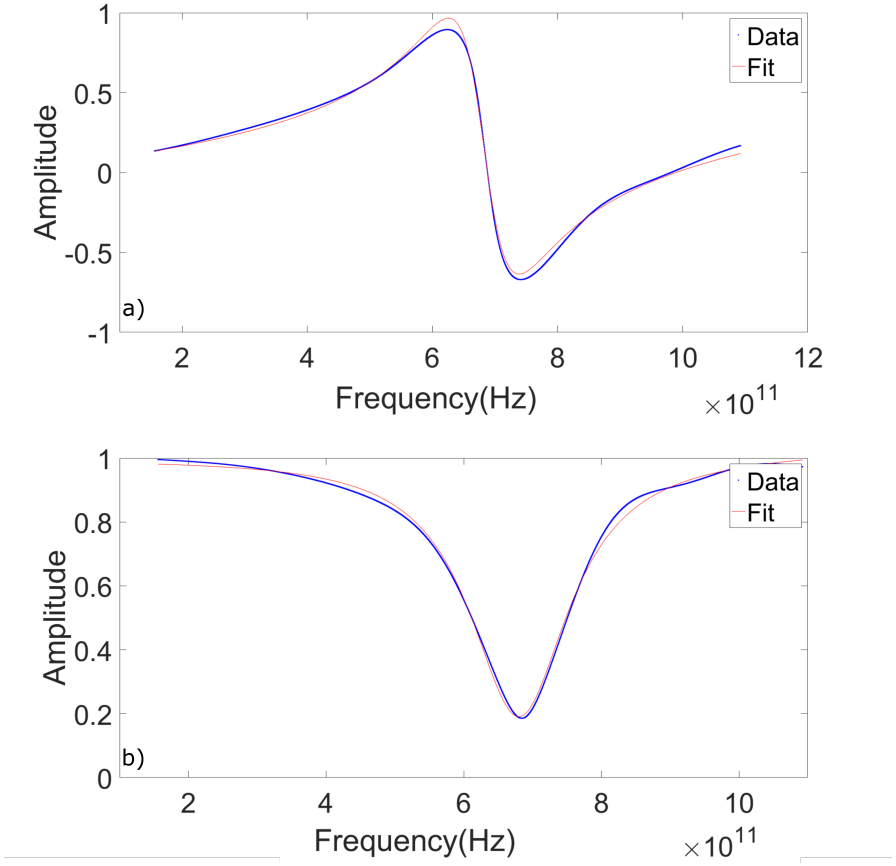

FIGURE 4.13: The terahertz transmission of the SRRs, It shows that there is a drop to 0.2 transmission of the Terahertz at the resonance position of the SRRs and a phase shift of 1.5 radians through the resonance. The minimum of the transmission and the centre of the phase change occur at near 0.7 THz.

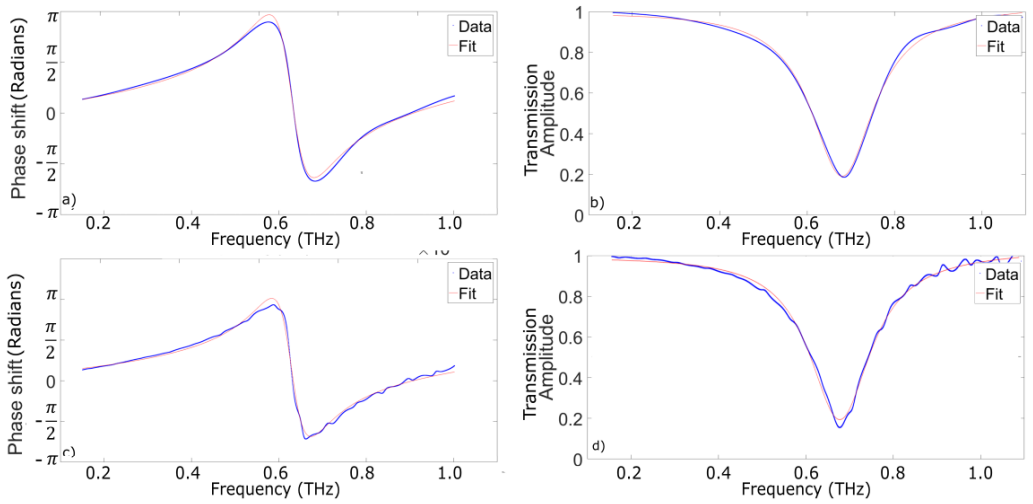

FIGURE 4.14: a) Shows the Transmission spectrum through an array of SRRs with an windowing function applied and b) shows the corresponding phase shift of THz as it passes through the SRRs with the same windowing. Both are fitted to the theoretical curves in equations 2.13 and 2.14 respectively. c) and d) show the same transmission and phase shift through the SRRs without windowing the time domain pulse.

In order to show that windowing the time domain data doesn't change the result and serves to remove the etalon effects caused by the emitter, the phase change and transmission spectrum of the un-windowed data are fitted to equations 2.13 and 2.14 respectively, this is shown in figure 4.14 c) and d) and the corresponding resonant frequencies are 0.6841 THz and 0.6867 Thz respectively, which are slightly shifted from the frequencies extracted from figure 4.14.

4.6.2 Second Pulse Analysis

The secondary pulses in the THz time domain pulses were analysed to show that they are reflections of the initial pulses. To do this the extraction window was moved to enclose the secondary pulse and cut of the initial pulse. Figure 4.15 a) shows the time domain spectrum with a exponential window applied to isolate the reflected pulse. Figure 4.15 b) shows the frequency spectrum of the initial pulse and the secondary pulse, it can be seen that the two spectra contain the same frequencies but the secondary pulse frequencies have a reduced amplitude compared the those of the initial pulse.

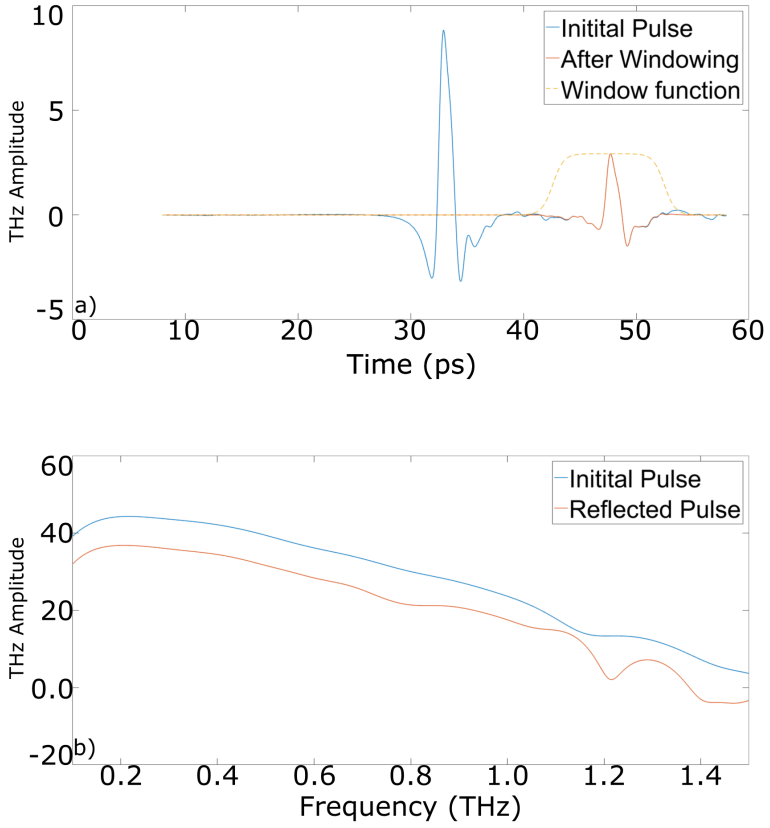

FIGURE 4.15: a) The time reflected pulse and the window applied to the time domain to isolate the reflection .b), The Frequency components of the initial and reflected time domain pulses. At low frequencies the reflected pulse contains an almost identical spectrum but with a reduced amplitude, as the frequency increases however, the reflected pulse begins to differ. This suggests that the emitter does not reflect all the THz evenly and could also have some absorption at these frequencies.

4.6.3 Experimental Error

Experimental error in this work is complex. When undergoing Fourier transformation, errors propagate through the transform, in this case, to give additional frequencies in the resonant response. However, the experimental error for the time domain measurements are small because each measurement is averaged over a long period of time. Error of a mean measurement decreases with as the square root of the number of measurements, in the case of these measurements where ten thousand scans are averaged, the error is reduced by a factor of one hundred. As such the errors are not visible in either the time or frequency domains.

4.7 Echo Self Referencing

An application of this secondary pulse is for Echo Self Referencing (ESR) as shown by Gorecki et al [139]. As shown in figure 4.16 the primary pulse and the secondary pulse are separated in time such that they can individually be converted from time domain into frequency domain through Fourier Transform. a) Shows the Terahertz TDS setup used, with a PCA emitter (section **??**) and a Pockels cell detector (section **??**). b) shows the path of the THZ pulse as passes from air into the Lithium Niobate sample, then passes back into air, these transitions from a low to high refractive index and then from a high to low refractive index are the origin of the internal reflection that leads to the secondary pulse. c) Depicts the both the initial and secondary pulses in the time domain and that they are separated in time such that they can be individually transformed through Fourier transform into the frequency domain.

As depicted in Figure 4.16 the secondary pulse is due to the internal reflections of the THz within the Lithium Niobate. This series of transmissions can be described as seen in equation 4.1 where A is an arbitrary power of the incoming pulse into the Lithium Nobate, T_{ab} and T_{ba} are the transmission coefficients of the boundaries of material a and b. P is the complex Beer Lambert term $P = exp(-i\omega\tilde{n}_b d/c)$ where d is the thickness of the material, c is the speed of light and $\tilde{n}_b$ is the samples complex refractive index of the sample. X_1 denotes the total transmission of the intial pulse through the sample.

$$X_1 = A \cdot T_{ab} \cdot P \cdot T_{ba} \tag{4.1}$$

Applying the same to the secondary pulse caused by the total internal reflection of the sample, we arrive at equation 4.2 where R_{ab} is the complex reflection coefficient from the interface between materials a and b at the samples boundary's, $R_{ab} = (\tilde{n}_b - \tilde{n}_a)/(\tilde{n}_b + \tilde{n}_a)$ where $\tilde{n}_a$ and $\tilde{n}_b$ are the complex refractive indices of the surrounding material and the sample respectively.

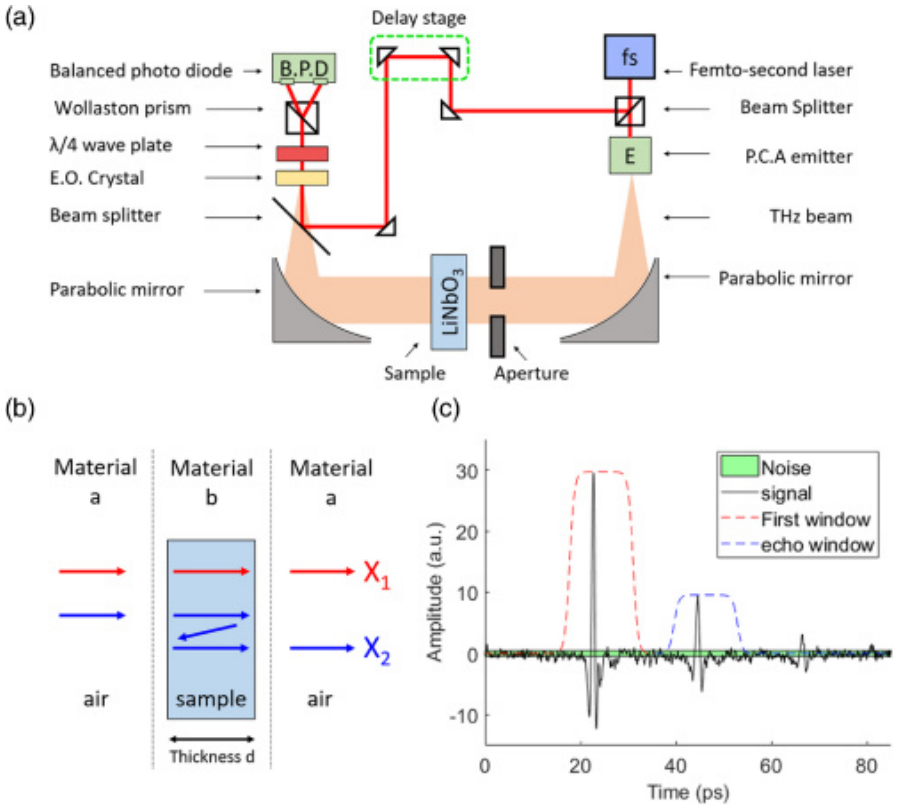

FIGURE 4.16: Reproduced from Gorecki et all [139]. a) Shows the Terahertz TDS setup used, with a PCA emitter and a Pockels cell detector. b) shows the path of the THZ pulse as passes from air into the Lithium Niobate sample, then passes back into air, these transitions from a low to high refractive index and then from a high to low refractive index are the origin of the internal reflection that leads to the secondary pulse. c) Depicts the both the initial and secondary pulses in the time domain and that they are separated in time such that they can be individually transformed through Fourier transform into the frequency domain.

$$X_2 = A \cdot T_{ab} \cdot P \cdot R_{ba} \cdot P \cdot R_{ba} \cdot P \cdot T_{ba} \tag{4.2}$$

By dividing the two pulses the transmission coefficients and the arbitrary power are removed which gives the complex transfer function H which can be represented as unwrapped polar co-ordinates of the complex Fourier transform with $|Y(\omega)|$ being the magnitude and $\phi(\omega)$ being the angle.

$$H = P^2 \cdot R_{ba}^2 = |Y(\omega)| \cdot e^{i\phi(\omega)} \tag{4.3}$$

The Complex refractive index of the sample can be written as $\tilde{n} = n_b + ik_b$, when n¿¿k the complex reflection coefficients can be taken to be real which allows the real and imaginary parts of the refractive index to be calculated separately as shown below:

$$e^{-2i\omega n_b d/c} = e^{i\phi(\omega)} \tag{4.4}$$

To give the real component, n_b when can then be used in equation to get the complex components, k_b.

$$e^{-2\omega k_b d/c} \cdot \left(\frac{n_b - n_a}{n_a + n_b}\right)^2 = |Y(\omega)| \tag{4.5}$$

Figure 4.17 a) shows the extracted relative THz intensity of a THz pulse through air, the z-cut lithium Niobate sample and the echo pulse through the sample in the frequency domain. While the pulse can be seen to have a bandwidth of upto 3 THz in air this drops off significantly in the Lithium Niobate to 1.5 THz due to a phonon feature at 4 THz [140]. The Bandwidth of the echo pulse is reduced further to around 1 THz.Figure 4.17 b) shows the extracted refractive index for z-cut lithium Niobate calculated using the air reference and the echo pulse reference for comparison. The shaded areas show the standard deviation of measurements twenty four taken over fifty minutes . Additionally the results given by Shao, Unferdorben and Yi-Min [141–143] are given for further comparison. While the values calculated from the different sources vary, likely due to differences in the samples and extraction methods. Despite this the values calculated with this echo method are comparable Upto 1 THz and a within this region has a much smaller standard deviation than the air reference method.

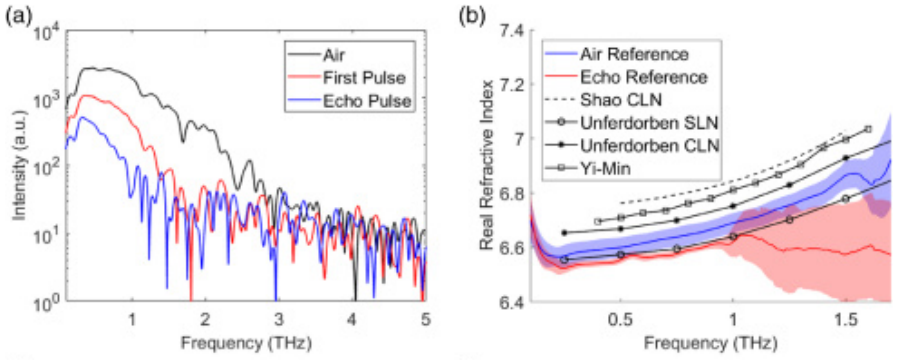

FIGURE 4.17: Reproduced from Gorecki et all [139]. a) The extracted intensity in the frequency domain for the THz pulse through air, the pulse through the Lithium Niobate sample and the echo pulse through the sample. b) The extracted real refractive index for lithium Niobate calculated using an air reference and an echo reference. Additional results by Shao, Unferdorben and Yi-Min are added for comparison.

This work has shown that through the analysis of the echo pulses causes by reflections within samples, the refractive index can be extracted without the need for an in air reference. The advantages of this method are that measurements can be taken faster and more accurately as samples don't require unloading and loading into setup which can cause misalignment of the beam path and secondary measurements for references

of the surrounding medium are also not required. While the bandwidth of these measurements is less than that of measurements made with a reference of the surrounding medium, the smaller standard deviation in the results and the improved measurement time make it a appealing alternative.

4.8 Conclusions

In conclusion, experimental techniques for THz time-domain spectroscopy were successfully developed both in transmission and reflection, which allow also for polarization-dependent studies. Split ring resonators were fabricated using photolithography and the optical response of split ring resonators was studied. We observe the polarization dependent resonances of the devices which fits the expected behaviour. The use of echo pulses as a reference is discussed and shown to be a potentially useful technique which avoids some of the complications associated with conventional references.

Chapter 5

Control of THz metasurface perfect absorption using a microcavity

5.1 Introduction

This chapter discusses the theory and experimental results for microcavity control over the metamaterial response. It is shown here that the resonant response of the metamaterial can be finely controlled through the use of a a metallic back reflector in such a way that demonstrates both fine control over the resonant responses position and the strength of the response. We experimentally demonstrate a THz metamaterial perfect absorber (MPA) that enables precise control over the perfect absorption condition by mechanically tuning the proximity of the metasurface to a mirror ground plane. First, a background study is presented with numerical simulations investigating the response of the coupling of the metasurface and metal back-reflector. Next, experimental results are presented using a fixed thickness spacer and a mechanically controlled microcavity.

In previous works, electrostatic control of MPAs using micro-electromechanical systems (MEMS) has been achieved in the GHz range by a variety of works [144]. Lei et al. [145] furthermore demonstrated a magnetically tunable MPA at GHz frequencies with an absorptivity that reaches 99.2%. Ma et al. [146] used a non-tunable MPA to achieve absorptions near 74% in experimental work characterised with Fourier-transform IR spectroscopy. Liu et al. [147] achieved fast kHz modulation of a PMA stack with up to 80% peak absorption achieved. A mechanically tunable air gap was also used by Schalch et al. [148], but this research is concentrating in much larger air-gaps up to a millimetre, with typical absorptions achieved in the region of 60-80%. In THz time-domain experiments, MEMS-type perfect absorber designs have been demonstrated that were able to continuously tune from the under- to overcoupled regime [149, 150] by shifting the metasurface resonance frequency.

Here we discuss experimental results using a mechanically tuned cavity for controlling the perfect absorption condition. The Chapter starts with a section discussing the theory of the microcavity-induced perfect absorption. Subsequently the experimental setup is described including the use of a white-light interferometer to calibrate the thickness. Results are presented both for a fixed cavity using spacer beads, and for a piezoelectrically controlled microcavity.

5.2 Theory of microcavity-induced perfect absorption

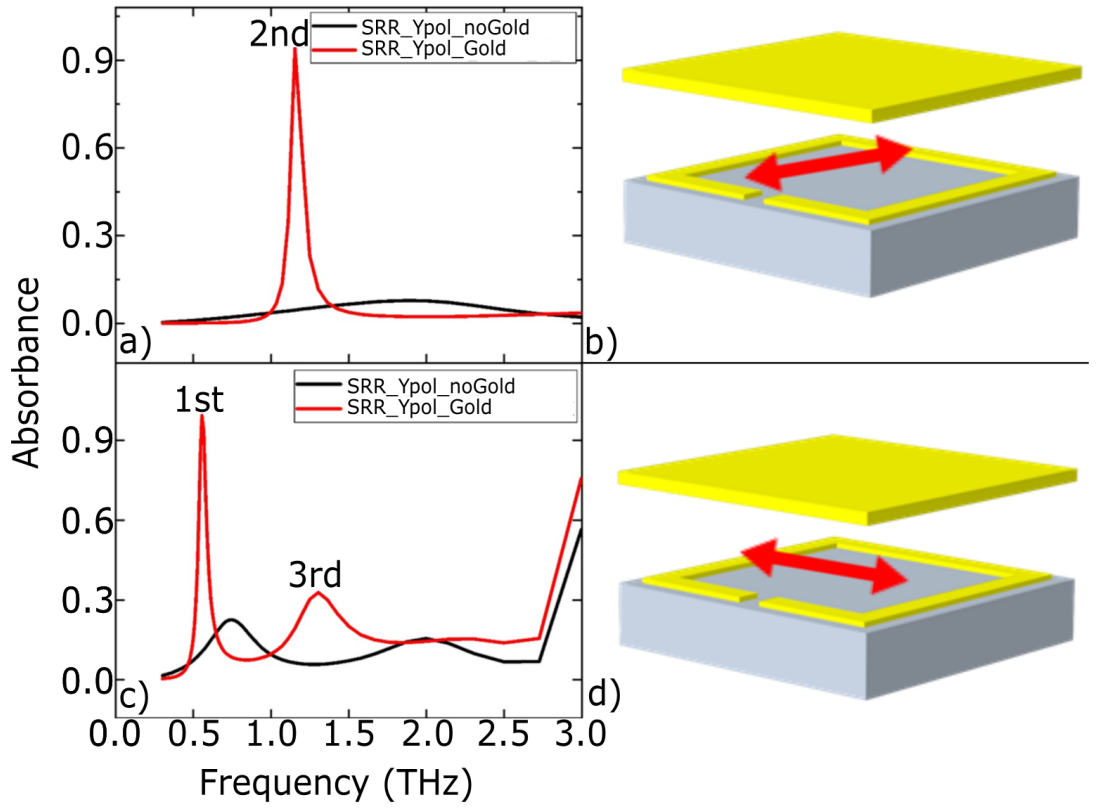

FIGURE 5.1: This figure shows the absorbance a split ring resonator. The split ring resonator has three resonances, the first and third resonance occur when the incident light is polarized across the split ring resonators gap. The second resonance occurs when the incident THz is polarized at 90 degrees to the gap.

Figure 5.1 shows the simulated absorption of a split ring resonator with and without a gold reflective layer. There are three main resonances of a split ring resonator. The first and third resonances occur when the incident THz is polarized across the SRR gap and the second resonance occurs at the polarization perpendicular to the gap. Figure 5.1 a) shows the response of the split ring resonator with the polarisation of in the incident THz parallel to the SRR gap. The black line shows the absorption of the SRR without a layer of gold and the red line shows it with the gold layer. The position of the first resonance shifts from 0.75 THz and shifts to 0.58THz with the inclusion of the gold

layer and the absorbance rises from 0.23 to 0.95. The third resonance shifts from 2 THz to 1.3 THz and the absorbance rises from 0.15 to 0.32.

Figure 5.1 b) shows the response of the same resonator with orthogonal polarisation to a) such that the polarisation is perpendicular the SRR gap. With this polarisation we see the resonance which occurs at 1.8 THz and shifts to 1.2 THz with an absorbance increases from 0.07 to 0.92. It is seen that each of the three resonances absorb light but that the first resonance has a more prominent absorption. Because of this higher absorbance and position of the resonance, the focus of this work is directed towards the first resonance.

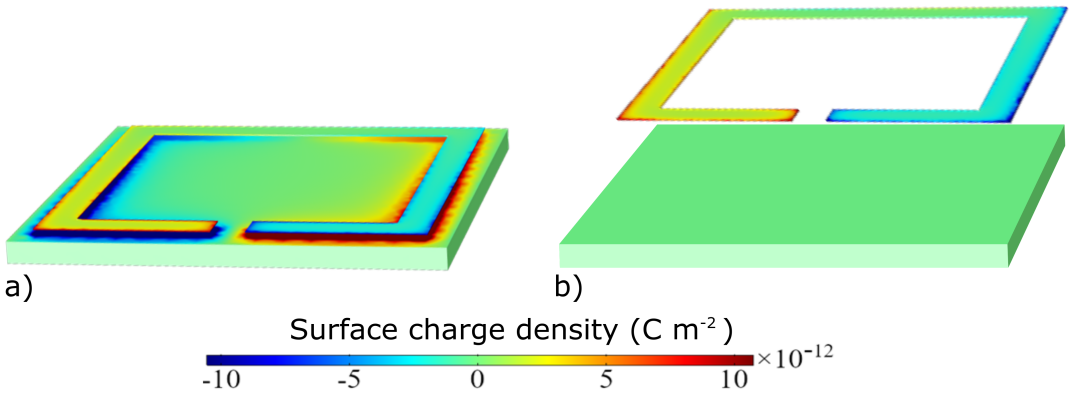

FIGURE 5.2: Charge induction in surface of the metamaterial by the SRR's at resonance is shown above. a) shows the charge in the gold layer from the SRR which is 0.5μm from the surface of the gold. b) is the charge in the gold layer from the SRR which is 16.5μm from the gold.

Figure 5.2 above shows the charge induction at different distances from the surface of the metamaterial by the SRR's at resonance. a) is the induced charge in the gold layer from the SRR which is 0.5μ from the surface of the gold. b) is the induced charge in the gold layer from the SRR which is 16.5μ from the surface of the gold. By comparing the two, it is seen that while there is charge induction in the first instance with the SRR close to the gold layer there is minimal to no charge induced in the gold layer in the instance with the SRR 16.5μ from the surface of the gold. This shows that the enhancement of the resonant response is not due to charge interactions because the maximum enhancement occurs at 18μm and at that separation there are no induced charges in the gold.

Figure ?? above shows the near field at different distances from the surface of the metamaterial. The top row of images show the near field for just the metamaterial layer where as the second row show the near field for metamaterials with a gold layer placed at 16μm from the metamaterial layer. It can be seen that the gold layer enhances the strength of the near field but the near field itself is weakened and barely noticeable

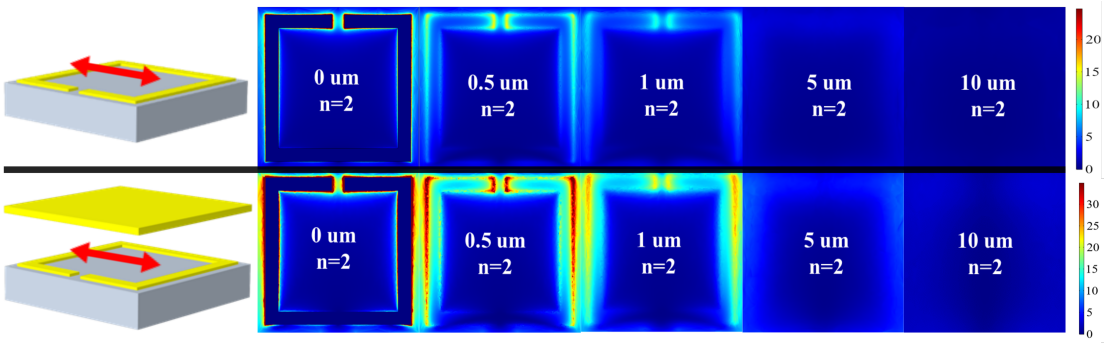

FIGURE 5.3: This figure shows the near field at different distances from the surface of the metamaterial. The top row of images show the near field for just the metamaterial layer where as the second row show the near field for metamaterials with a gold layer placed at 16μm from the metamaterial layer. It can be seen that the gold layer enhances the strength of the near field but the near field itself is weakened and barely noticeable once you are 5 or 10μm from the metamaterial layer in both cases. This demonstrates that the enhancement is not due to interactions in the near field as the enhancement occurs at larger separation.. The red arrows indicate the polarization of the incident THz with respect to the orientation of the split ring resonators.

once you are 5 or 10μm from the metamaterial layer in both cases. This demonstrates that the enhancement is not due to interactions in the near field as the enhancement occurs at larger separation.. The red arrows indicate the polarization of the incident THz with respect to the orientation of the split ring resonators. Due to the near field being so weak once we pass a distance of 10μm this shows us that the enhancement effect is not due to near field interactions as the enhancement is observed at greater separations than this.

Split ring resonators used in this work can be considered electrically long as their side length is approximately one tenth of the wavelength of the incident THZ. The near field range of electrically long antenna is defined by the Fraunhofer distance, equation 5.1. The Fraunhofer distance depends on the wavelength of the light (λ) and the physical size of the resonator (D) [151]. In this case the near field for terahertz with a frequency of 0.6 THz has a corresponding wavelength of 500μm. The resonator size used in these experiments has a side length of 50μm. By putting these numbers into equation5.1 we get a near field range of 10μm which corresponds to the results shown in the simulations in figure 5.3.

$$near_field_range = \frac{2D^2}{\lambda} \tag{5.1}$$

Equation 5.2 is the equation for the reflectively through infinite reflections of a metamaterial cavity. $\tilde{r}$ is the total reflection from the cavity, $r_{\tilde{12}}$ and $r_{\tilde{21}}$ are the reflectivity from each side of the metamaterial, $t_{\tilde{12}}$ and $t_{\tilde{21}}$ are the transmission through each side of the metamaterial and β is the phase shift due to propagation through the cavity[152].

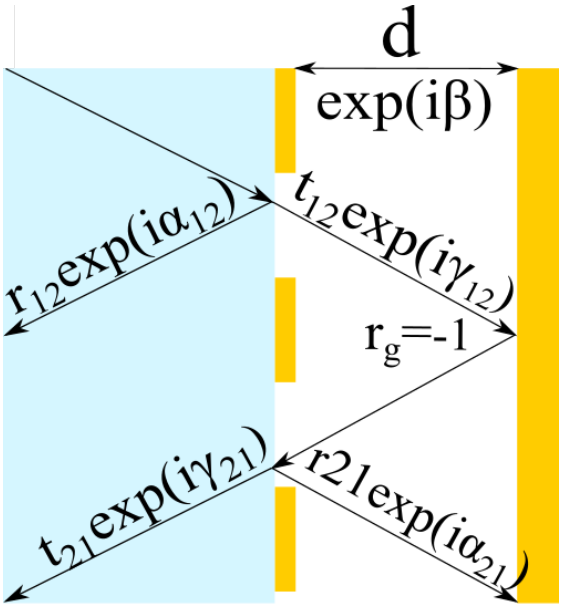

FIGURE 5.4: Figure 5.4 shows the phase and amplitude of the light as it interacts with different parts of the cavity. r_{12} and r_{21} are the changes in the lights amplitude as it is reflected off of each side of the meta-surface. t_{12} and t_{21} are the equivalent changes in the amplitude as it is transmitted through the meta-surface. α_{12}, α_{21}, γ_{12} and γ_{21} are the corresponding phases for the reflection and transmission for both sides of the meta surface respectively. r_g represents the π phase shift given by the reflection from the gold layer .The summation on infinite reflections through this cavity gives Equation 5.2

$$\tilde{r} = r_{\tilde{12}} - \frac{t_{\tilde{12}} t_{\tilde{21}} e^{i2\beta}}{1 + r_{\tilde{21}} e^{i2\beta}} \tag{5.2}$$

It can be seen from equation 5.2 that for the reflectivity of the cavity to be zero, the reflectivity from the metamaterial and the light that enters then exits the cavity must cancel out through destructive interference. For this to occur, the phase of both of these sources of light must be opposite to each other and the amplitudes must be equal. By assuming that the total reflectivity of the cavity is zero and that the reflectivity and transmission from each side of the metamaterial are the same, we can arrive at equation 5.3.

Equation 5.3 shows the cavity phase shift (β) required for there to be zero total reflectivity from the cavity. It is seen that it is dependant on the transmission phase(γ) and amplitude (t) of the SRRs and the reflection phase(α) and amplitude (r) of the SRRs . Equation 5.4 is the phase shift due to the cavity (β), it shows the dependence of the phase shift with both wavelength(λ) of the THz and the refractive index of the medium in the cavity(n) and thickness of the cavity(d).

$$e^{2i\beta} = \frac{re^{i\alpha}}{t^2e^{2i\gamma} - r^2e^{2i\alpha}} \tag{5.3}$$

$$\beta = \frac{2\pi dn}{\lambda} \tag{5.4}$$

Equation 5.4 shows that as the cavity thickness changes. In-order to maintain the same phase shift due to the propagation in the cavity, the wavelength at which zero reflectively is achieved is must change. This shows us that to create a wavelength tuneable perfect absorber, we need to change the cavity thickness in order to shift the position of the resonant wavelength.

By introducing a gold layer in close proximity to an array of SRRs, as show in figure 5.1, their resonant response can be greatly enhanced to create a near perfect absorber [25, 87, 153] . With the inclusion this gold layer, the SRRs that initially were an predominantly transmissive structure become reflective instead. This change is due to the gold layer being thicker than the skin depth of THz in gold and so acts as a mirror [154, 155]. This near perfect absorption by the SRR and gold layers is due to constructive interference between the light reflected by the SRRs and the light that is transmitted through the SRRs onto the gold layer and reflected back [152]. The frequency that the maximum constructive interference occurs is determined by the thickness of the cavity as well as the the transmission and reflection coefficients of the metasurface.

5.3 Micro Cavity Experimental Setup

Figure 5.5 shows the experimental setup used to measure both the reflected THz and the etalon of the cavity formed between the SRR layer and the gold mirror layer. A femtosecond pulsed laser is split into to beams, the first of which is directed to a photoconductive antenna (PCA) [126, 156], This PCA acts as an emitter for the THz. Once emitted the THz is directed into the cavity through a pair of apertures to removed unwanted back reflections, these apertures are one centimeter in diameter meaning the beam that is incident upon the resonators is smaller than the size of the resonator array . The THz then exits the cavity and is sent into the detector along with the second arm of of the split femtosecond pulsed laser. The Terahertz and femtosecond laser are sent into a Pockels cell **??** and the white light laser is directed into the cavity using a removable mirror, the reflected light is sent to a spectrometer where the free spectral range and, subsequently, the cavity thickness is measured. In figure 5.5 the rectangular square dotted line is the microcavity and its mount, this part of the set up changes for different experiments. Figures 5.7 5.7 5.8 are different samples used in the different experiments.

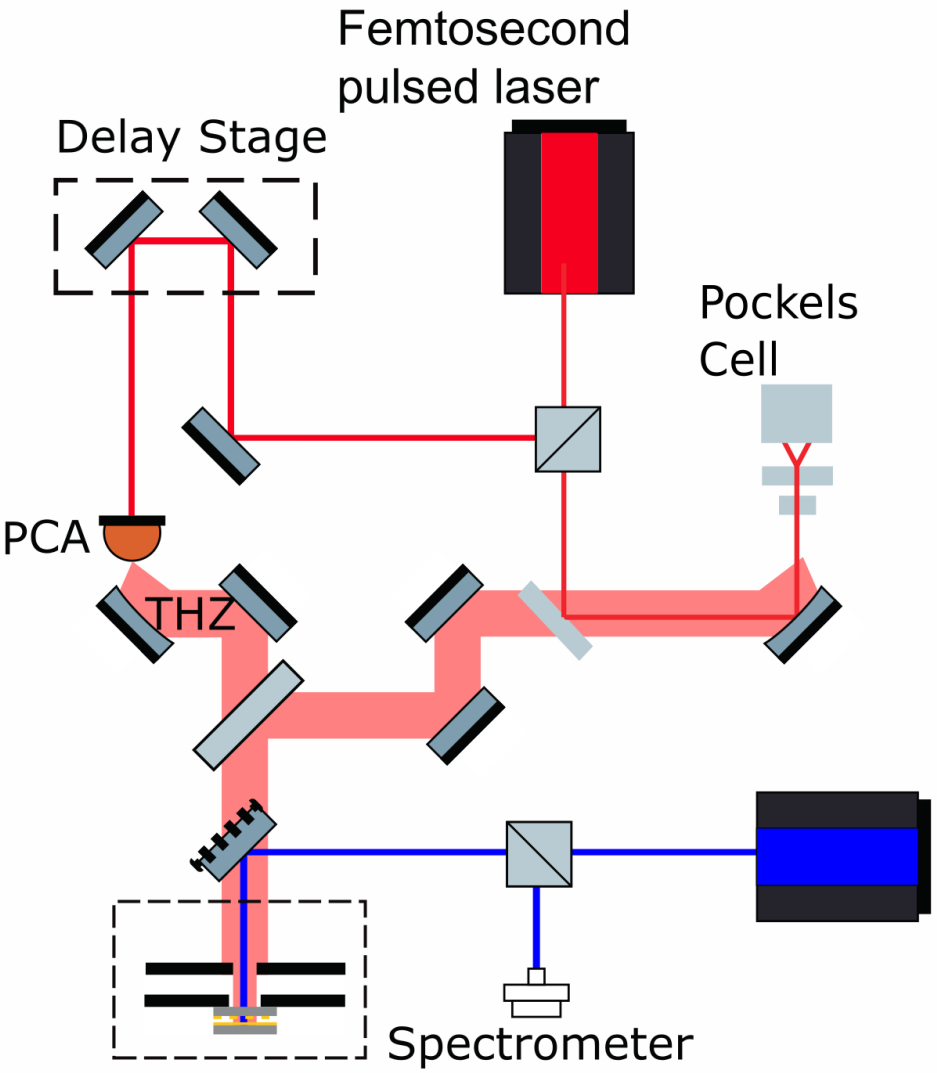

FIGURE 5.5: The experimental set-up used to measure the THz reflection as well as the cavity thickness is shown above. A THz time domain reflection spectroscopy is used to collect the reflected THz from the sample. A pair photo conductive antenna (PCA) serve as emitter and detector for the THz radiation. The THz is directed towards the cavity using gold mirrors and a 5mm thick silicon wafer used as a beam splitter. The THz then enters the cavity through a series of apertures to prevent unwanted back reflections. The THz then leaves the cavity and is sent to the detectors PCA. To measure the cavity thickness a coherent white light source is used which is passed into the cavity and the light from the cavity is collected and measured on a spectrometer. The etalon of the cavity is then measured using the free spectral range and thus the cavity thickness is measured.

Equation 5.5, below, shows the equation for free spectral range, Δv is the free spectral range, n_g is the group index of the medium and L is the cavity length [157].

$$\Delta v = \frac{c}{2n_g L} \tag{5.5}$$

Figure 5.6 shows the fitting of the reflected white light from the cavity, as shown in figure 5.5, in order to find the free spectral range of the cavity and hence find the cavity length as per equation 5.5.

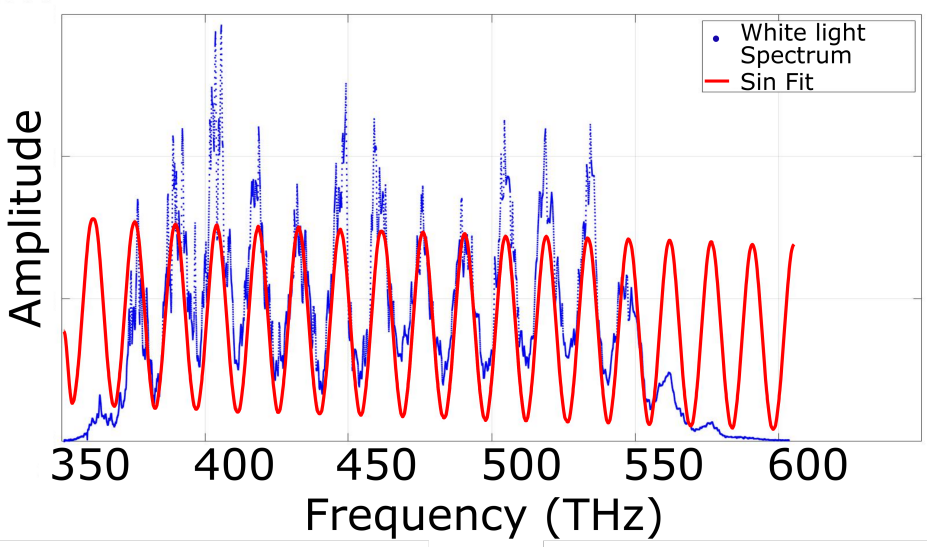

FIGURE 5.6: The blue line in figure 5.6 is the reflected white light from the cavity. The etalon formed by the cavity has a free spectral ranged which is dependant on the cavity length as shown by equation 5.5. By fitting a sin curve to this, the spacing of the etalon fringes can be found and from that the cavity thickness.

5.3.1 Method

Gold split-ring resonators of 45 µm side length and 100 nm thickness were fabricated on a quartz substrate using photolithography. A separate uncoated gold mirror with a surface flatness of 63 nm over a diameter of 12.7 mm, was mounted at either a fixed or variable distance from the metasurface as described further below.

5.3.2 Microcavity: Fixed Cavity

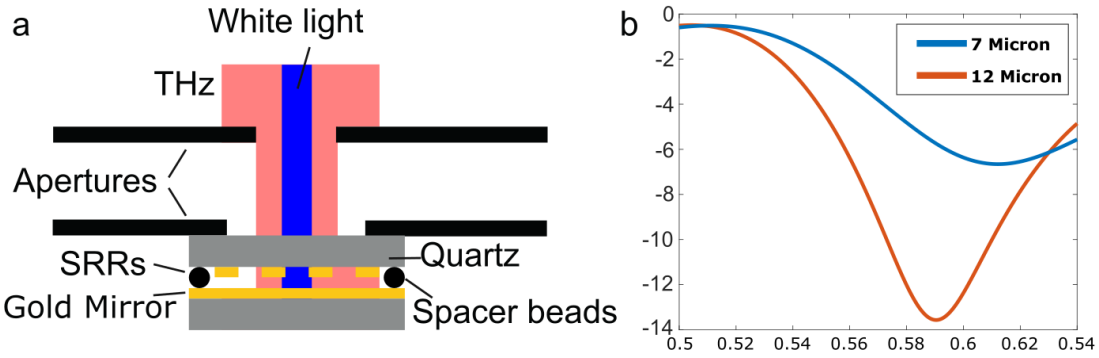

FIGURE 5.7: Sub-figure a) shows a close up of the experimental setup. A SRR metasurface is separated from a gold mirror layer by spacer beads. Terahertz pulses and white light are directed into the cavity through a series of apertures, the last one of which has the cavity mounted on it. b) shows the corresponding reflection measurements of two cavities with thickness 7 and 12 µm. The 12 µm cavity shows a stronger resonant response than that of the 7 µm cavity.

Figure 5.7 a) is the cavity used in the fixed thickness experiment. These cavities consist on two quartz slides separated by micro-beads of different sizes. The two inside quartz surfaces of the microcavity are as follows, the first is a meta-surface consisting of gold SRRs with a slide length of $50nm$ and a ring width and gap size of $4nm$. The second side is a $200nm$ thick layer of gold.

Figure 5.7 b) shows the reflection graphs for two fixed cavities, of thickness 7μm and 12μm. These cavities are made with spacer beads in a UV set adhesive. The resonant response of the 12μm cavity is stronger than that of the 7μm cavity.

This work shows that cavities of different thicknesses have a noticeably different resonant response. To further expand on this, the work evolved into that done in section 5.3.3 where instead of the cavities being a fixed size, the cavity size is adjustable. The advantage of having an adjustable cavity over a fixed cavity is more cavity thicknesses can be measured without the restriction of the spacer bead sizes and the fabrication of the fixed cavities.

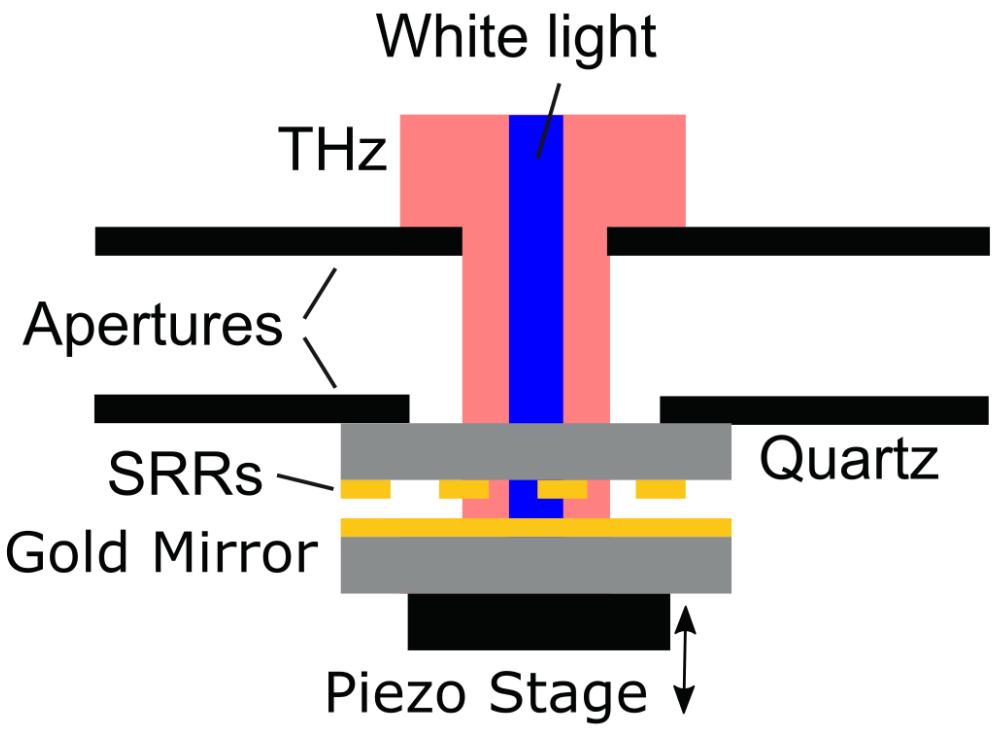

FIGURE 5.8: This figure shows a close up of the Piezo controlled microcavity. As with figure 5.7 a), this setup is in place of the boxed region of figure 5.5. The incident terahertz is sent through a series of apertures to minimise back reflections from the quartz and the aperture the quartz is mounted on from interfering with the measurements. The THz then passes through the quartz and SRR layers to a gold mirror with a surface flatness of 63nm over its diameter of 12.7mm. The terahertz is then leaves the microcavity and back into the THz Reflection TDS setup. The gold mirror is mounted on a piezo stage which allows for the fine control of the mirrors position, roll and yaw with respect to the SRR to ensure the two surfaces are parallel.

5.3.3 Microcavity: Piezo Stage Cavity

Figure5.8 presents in greater detail the experimental arrangement of the MPA sample. The MPA consists of an array of 100 nm thick gold SRRs deposited onto a 1 mm thick quartz substrate. An uncoated gold mirror with a surface flatness of 63 nm over a diameter of 12.7 mm, was aligned parallel to the metasurface array and acted as the back-reflector. The separation of the gold mirror to the SRRs was controlled with nanometer precision using a closed-loop piezoelectric stage. Suppression of a number of unwanted THz back-reflections from edges of the sample holder was achieved with the use of apertures placed in front of the sample. as illustrated in figure 5.8

5.4 Results

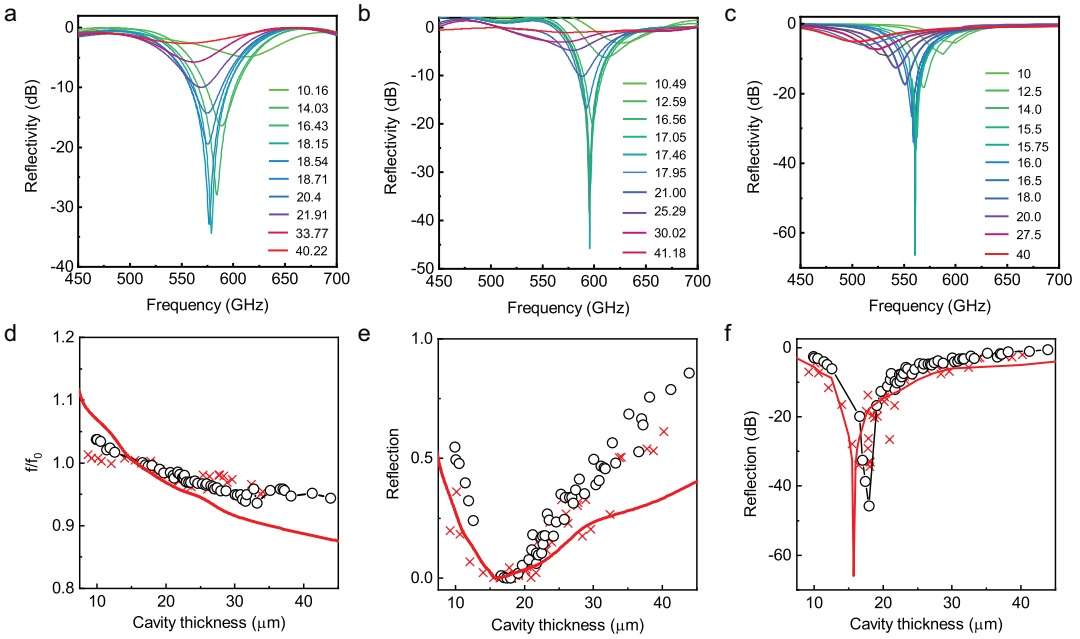

FIGURE 5.9: (a-c) Terahertz reflectivity spectra for different values of cavity size. Experimental traces (a,b) and simulated (c) spectral response of the metamaterial for a range of cavity thicknesses from 10 - 41.2 µm as indicated in legend. (d-f) Extracted values for resonance frequency normalized to the perfect absorption frequency f_0 (d), minimum in reflectivity on linear scale (e) and log-scale (f), as a function of the cavity thickness. Data shown for the two experimental runs (crosses, dots) and simulations (red line).

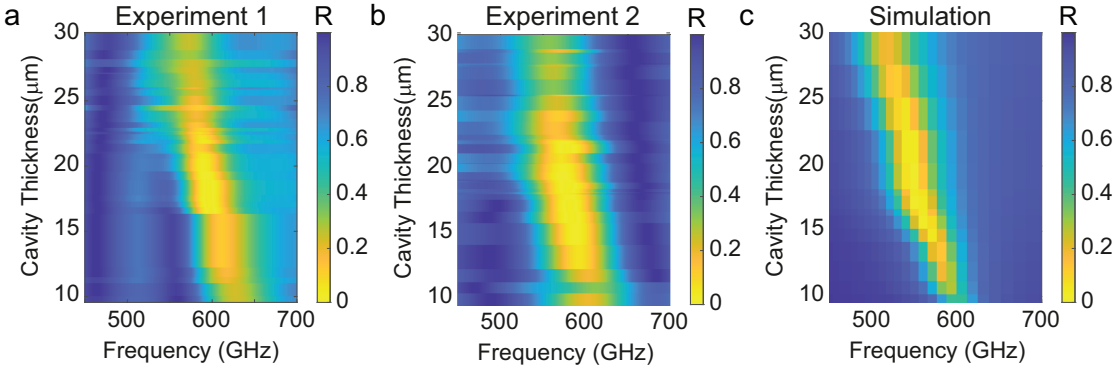

FIGURE 5.10: Figure showing the effect of changing cavity thickness on the reflectivity of the meta-surface.(a-c) Maps of the reflected THz spectrum versus cavity thickness, for experiments 1 and 2 (a,b) and for simulations (c).

Figure 5.9 shows the experimental and simulated response of the tunable SRR-mirror cavity. Corresponding colour maps of reflectivity against frequency and cavity thickness are presented in Figure 5.10. Experimental reflectivity spectra for the tunable SRR-mirror cavity are shown in Figure 5.9(a) and (b) for different values of the cavity thickness between 10 µm and 45 µm, where the two datasets correspond to different experimental runs which are respectively labelled as Experiment 1 and 2. Experiments 1

and 2 are identical experiments using the same SRR on Quartz sample and gold mirror but performed with complete re-alignment of the setup and on different days. Corresponding simulation results for the same SRR and cavity dimensions are shown in Figure 5.9(c). The power spectrum of the reflected THz signal is highly dependant on the separation between the SRRs and the gold mirror, and shows a sharp resonant drop around the optimal MPA configuration. Figure 5.9(a) exhibits a drop in the reflectivity of 34 dB which occurs at a cavity thickness of 19 µm, while Figure 5.9(b) has a drop in the reflectivity of 45.8 dB, which occurs at a cavity thickness of 18.4 µm. The minima in the reflected THz signal occur at 575.6 GHz and 591 GHz respectively in the two experiments. In comparison, the simulations which use finite element modelling in Figure 5.9(c) shows a drop in reflectivity of 66.7 dB at 561.1 GHz.

Figure 5.9(d) shows the spectral position of the dip in spectral reflectivity for each experiment at different cavity thicknesses, normalized to the frequency scan of the minimum MPA reflectivity. The observed shift in the frequency is around $\pm 5\%$ of the centre frequency, or around 50 GHz, which is somewhat smaller for the experimental results compared to that of the simulation. Figure 5.9(e-f) show the amplitude of the minimum reflectivity of the cavity at different cavity lengths on linear (e) and logarithmic (f) axes. These respectively display that the reflectivity in the experimental results is more susceptible to the cavity thickness than that of the simulated results, and also that the critical thickness of the simulated cavity is smaller than that of the experiment.

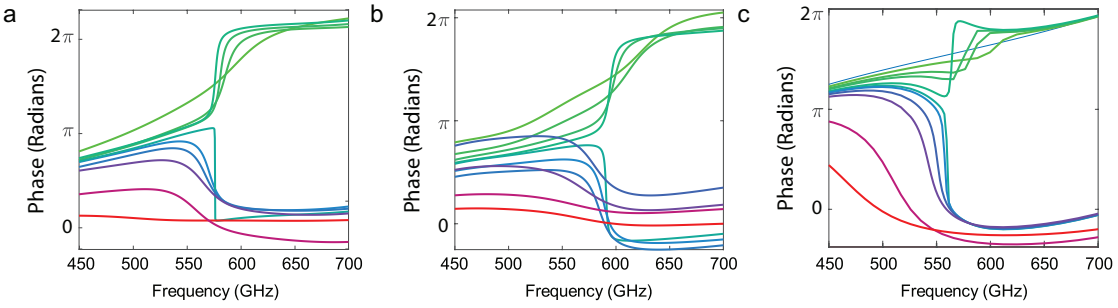

FIGURE 5.11: Figures showing the experimental (a,b) and simulated (c) phase response of the metamaterial for the same range of thicknesses as Figure 5.9. It is seen in a) b) and c) that at the resonant position at arround 600 GHz there is a 2π shift in the phase between the cavity thickness lee than that of the the resonant frequency and those of a greater cavity thickness.

.

Figure 5.11 presents the corresponding phase response of the reflected THz for the two experimental cavities as well as the simulations. Correspondingly, Figure 5.12 shows in more detail the relationship between the phase of the reflected THz from the microcavity for different cavity thicknesses in the range 10-20 µm. The simulated response, shown in Figure 5.11(c) and Figure 5.12(c), presents the expected behaviour for the hybrid SRR-microcavity structure. For cavity thickness sufficiently far (i.e. several µm) from the critical thickness, we see a slow evolution of the phase over the spectrum

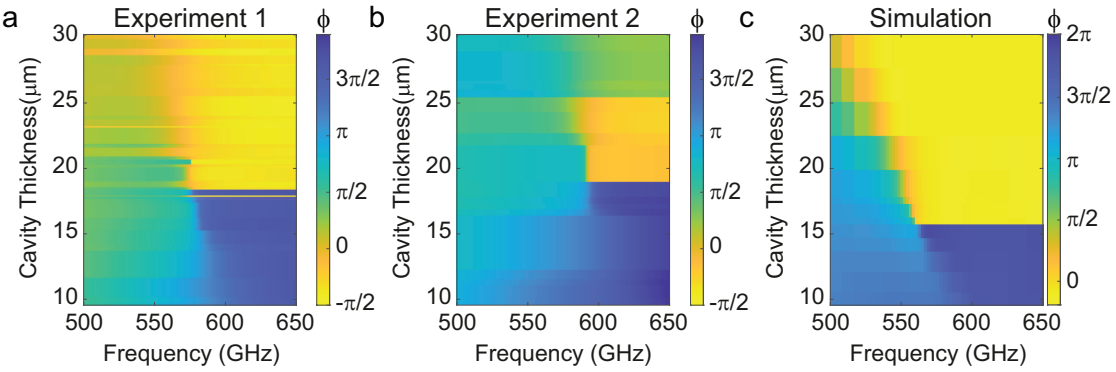

FIGURE 5.12: Experimental and simulated phase response heat maps of microcavityies with varying cavity thicknesses

Figure showing the effect of changing cavity thickness on the relative phase of the metasurface and the corresponding shift in the sign of the phase. (a-c) Maps of the phase from the reflected THz spectrum versus cavity thickness, for experiments 1 and 2 (a,b) and for simulations (c).

from 0 to 2π, which is indicative of the individual SRR resonance. As the cavity approaches the critical thickness, an additional sharp phase jump becomes apparent, related to the interplay of the metasurface and cavity modes. Cavity sizes smaller than that of the critical thickness display a relative increase of the phase to 2π, while cavity sizes larger than the critical thickness show a jump back to zero phase. As a result, the phase response splits up in two separate regions for thicknesses below and above the critical thickness, where the phase flips to either 2π or 0 above the perfect absorption frequency. Qualitatively the same behaviour for the MPA structure, including the characteristic splitting of phase response, is found in the experimental data of Figure 5.11(a,b). Differences in the slow overall phase evolution are attributed to the normalization to the reference spectrum between experiments and theory, where in the latter case we normalized to the substrate without SRRs and subtracted a slowly varying background phase taken at 50 μm cavity length. This deviation does not affect significantly the fast phase evolution around the cavity critical condition.

The maps in Figure 5.12 clearly show the presence of a phase singularity at the perfect absorption location where the optical vortex results in a phase accumulation of 2π. The point in the centre of the phase vortex occurs at the critical cavity thickness which in turn corresponds to the minimum signal of the reflected THz response.

5.5 Conclusion

In conclusion, we have demonstrated THz devices with tunable and reconfigurable characteristics based on a metasurface perfect absorber geometry with mechanically controlled cavity. Our experiment achieves a reflectivity minimum of -45.8 dB close to the detection limit of our THz time domain setup. The combination of a bidirectional

accuracy of ±10 nm and *in-situ* characterization using a white-light interferometer offers reliable calibration of cavity thicknesses. We show with numerical simulations that the mechanism explaining the enhanced absorption cannot be near field effects, they are shown to be negligible at the distances where maximum absorption occurs. Our precisely tunable experimental system is in good agreement with the purely interferometric interpretation of the MPA response [158]. The work demonstrated in this study shows the effectiveness of manipulating the MPA response and its sensitivity to design parameters. This work can be used for more efficient THz detection and sensing applications [88, 159]. Also, in future, the SRR response may be tuned using active substrates such as photo-conductive insulators [160], in addition to more advanced control over the cavity length using for example arrays of microelectromechanical piston actuators [161], in order to further optimize the maximum absorption and tunability range of the system with potential applications in active phase control.

Chapter 6

Future Prospects and Conclusions

6.1 Future Prospects

This work opens up multiple avenues for future projects which are detailed below. With the inclusion of additional materials such as Lithium Niobate or a Phase change material such as Antimony Trisulfide (Sb_2S_3) would allow for the shifting of the SRR's resonant position to be moved through the optical properties of the materials being changed i.e. re-writing lithium niobate metasurfaces or changing the phase of the phase change materials.

6.1.1 Microcavity: Lithium Niobate

Work done by Goreki et al shows that Iron doped Lithium Niobate (Fe:LiNb0_3) and graphene can be used to create optically re-configurable metasurfaces within the THz regime [160]. By illuminating the lithium niobate with a non-uniform pattern it was shown that once illumination was stopped, the illuminated areas retained the properties they exhibited under illumination until thermally annealed or until the changed was reversed via thermal annealing or uniform illumination on the sample. Utilising this and combining it with the Terahertz Microcavity, the position of the maximum absorption can be shifted optically by rewriting the meta-surface. Additionally due to Fe:LiNb0_3's high refractive index in the Thz regime (3-7?) the peak of the absorption is displaced to the frequencies without the manipulation and re-configuration of the meta-surface.

The ability to move and and rewrite the peak position of the Meta-surfaces absorption would allow for perfect absorption across a larger range of frequencies but still grant a high Q-factor. This would allow for the development of THz detectors that aren't reliant on incident laser light such as Photo-conductive Antenna and Pockels cells while

having a broad range of detection and such as the Golay cell but with a high frequency resolution due to the relative broadness of the absorption peak.

6.1.2 Microcavity: Membrane Cavity

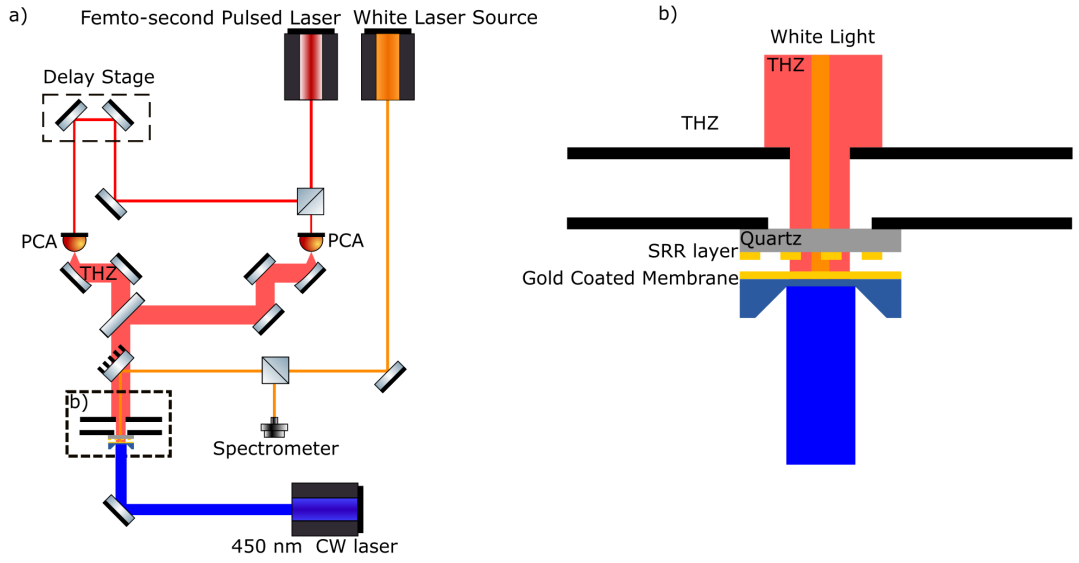

FIGURE 6.1: a) This figure shows the overall proposed setup for a membrane cavity experiment. A reflection THz TDS setup is used to measure the strength of the resonant response between the resonators and gold coated membrane. A white light CW laser source is used to measure the cavity thickness as in 5.3. An additional laser is introduced onto the membrane so that it undergoes thermal expansion and changes the cavity thickness. b) shows a close up of the part of figure a) in the boxed area. Here it can be seen that as in previous work the quartz layer with the SRR surface is mounted on an aperture with the cavity positioned parallel to the SRR's such that when it thermally expands it will pass into and through the cavities critical thickness.

Figure 6.1 a) is the experimental setup for the membrane microcavity experiment. This setup varies from the setups that have used the setup shown in figure 5.5 as there is an additional 450nm CW laser added to heat the membrane. By heating the membrane with the incident laser, the membrane is caused to under go thermal expansion. This expansion forces the membrane to flex and hence changes the separation between its surface and the Meta-surface, thus changing the cavity thickness. Figure 6.1 b)is the membrane cavity. Alternatively heating via a heating element surrounding the membrane would also causes the thermal of the membrane.

An alternative advancement on the microcavity would be the utilisation of a microcavity with a membrane. The membrane would replace the gold mirror layer of microcavity and could be heated via laser, heat gun or heating coil. By heating the membrane, it would flex under thermal expansion, this flex would change the cavity thickness proportionally to the temperature. This would allow for the fine control of the cavities

thickness around the position of maximum absorption. One down side of this proposed idea is that the membrane would flex more towards its center which would lead to a cavity thickness that varies across the cavity.

6.1.3 Microcavity: Phase Change

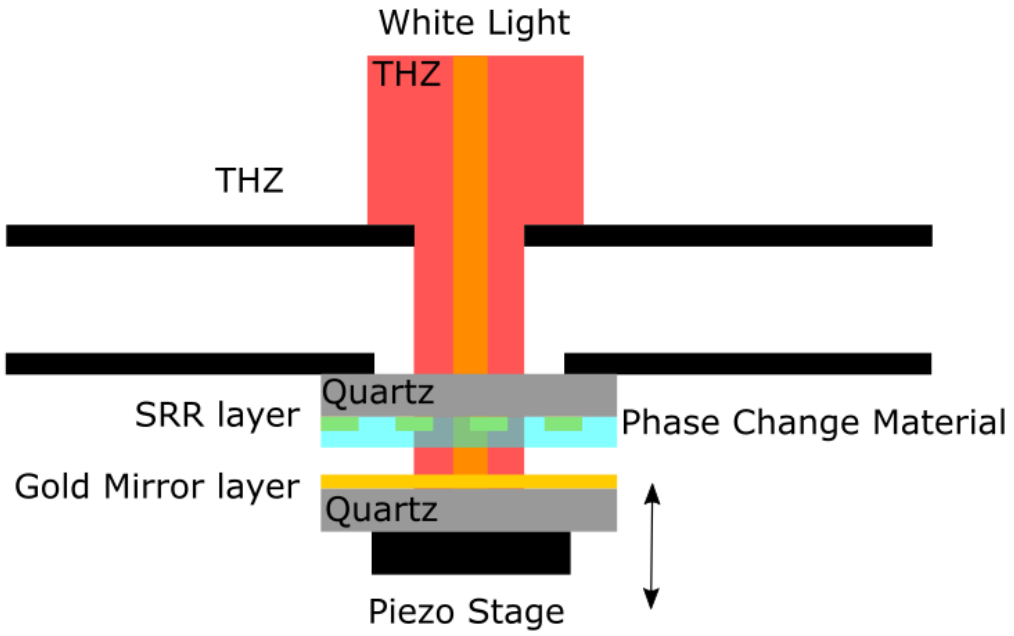

FIGURE 6.2: This experimental setup would replace the boxed section in figure 5.5. In this setup a layer of phase change material is used to shift the metamaterials resonant frequency between two new frequency's defined by the phase change materials crystalline and amorphous phases. A Peizo mounted gold mirror is also used to allow the cavity to me moved to the new critical thicknesses of the corresponding resonances.

A future addition to the Terahertz Microcavity would be a layer of phase change material such as Sb_2S_3 (Antimony trisulfide) or Gst (germanium-antimony-tellurium) [162, 163]. Phase change materials have two physical states, crystalline and amorphous, which have been shown to have substantial refractive index changes [164–167]. Phase change materials can be switched between these two states optically, thermally and electrically. Through the inclusion of a phase change layer and the chosen switching method it would be possible to create a Terahertz microcavity with two different resonant responses which would allow for a larger range of measurements similar to that of the lithium Niobate proposed idea.

6.2 Conclusion

THIS work the shows limitations and advantages of the Terahertz spectrum from its generation to its applications and detection.Terahertz is used in fields such as security, food testing, medicine and communications. Because of all these potential applications, the need for more reliable Terahertz detection is something that people are striving for. The Theory behind metamaterial split ring resonators is discussed with regards to the inductance-capacitance circuit model. Simulations of split ring resonators show their charge and current distributions also show the inductance and capacitance of their response with current flow within the split ring and a build up of charge at the split ring resonators gap.

Details on the extraction of the terahertz response and data windowing are discussed and how work done on how internal reflections can be used to determine a materials refractive index without the requirement of taking in air references is also shown.

Towards this end, this work has looked into the development of Terahertz absorbing metamaterials and their improvement through their inclusion in microcavity systems in order to achieve perfect material absorbers. By manipulating the size of the microcavity, it has been shown that the metamaterials resonant response is both enhanced, narrowed and also tunable. The mechanism behind this response is also investigated through simulations of charge, near-field and the phase responses of the metamaterial and the gold layer. These simulations help show that the cavity response is a phase interference effect which constructively interferes at the resonant response and destructively elsewhere due to the phase shift caused by light transmitting into the microcavity and reflecting back out. By altering the cavity thickness, the frequency at which the peak absorption occurs shifts due to the inter cavity phase shift changing.

The next stages of experimentation are proposed for methods of further control over the microcavities resonant response and for methods of tunability. From using Lithium Niobate and graphene to create re-writable metasurfaces for use within a microcavity. Or the inclusion of a phase change material, such as Antimony Trisulfide which would allow the resonant response to be changed though the properties of the different phases of the phase change material. The inclusion of a gold coated membrane in the microcavity in place of the gold mirror, would allow for the tunability of the cavity through thermal expansion of the membrane. Through the inclusion of these additional elements the microcavity could be tuned over either a larger range or a shifted range.

6.3 Conferences and Published work.

6.3.1 Conferences

London Plasmonic Forum King's College London on the 8th of June 2018: Presented Poster

TeraMetaNano 4, Leece in Italy: Presented Poster

Complex Nanophotonics Science Camp at Cumberland Lodge, Windsor Great Park 2019: Presented Poster

Quantum Light and Matter Summer School, 2017-2019: Organised the conferences, Talks and Posters, Presented posters and gave talks.

6.3.2 Published Work

Mechanically Tunable Terahertz Metamaterial Perfect Absorber LK Piper, HJ Singh, JRC Woods, K Sun, OL Muskens, V Apostolopoulos Advanced Photonics Research, 2100136

Optical Tuning of Graphene Electronics and Plasmonics on Iron Doped Lithium Niobate J Gorecki, L Piper, V Apostolopoulos, S Mailis, N Papasimakis 2019 Conference on Lasers and Electro-Optics (CLEO), 1-2

High-precision THz-TDS via self-referenced transmission echo method J Gorecki, N Klokkou, L Piper, S Mailis, N Papasimakis, V Apostolopoulos Applied Optics 59 (22), 6744- 6750

Optically Reconfigurable Graphene/Metal Metasurface on Fe:LiNbO3 for Adaptive THz Optics J Gorecki, L Piper, A Noual, S Mailis, N Papasimakis, V Apostolopoulos ACS Applied Nano Materials 3 (9), 9494-9501

Appendix A

Split-Ring Resonator Equations

The derivation for equation 2.1. Where ε_0 is the permittivity of free space, ε_g is the relative Permittivity of material in the gap of the SRR. d is the width of the SSR gap, h is the height of the SRR and R is the radius of the SRR. σ is the skin depth of the SRR. w_g and w_r is the width of the ring at the gap and in the inductance region of the SSR respectively . [112]

$$w_{eff} = \frac{w_r}{2} \tag{A.1}$$

(A.1) w_{eff} is the effective ring width of the SRR and is taken to be half of the width of the ring within the inductance region.

$$a = R - \frac{w_{eff}}{2} \tag{A.2}$$

(A.2) a is the approximate radius of the inductance region of the SRR, it is equivalent to the difference between the SRR radius and half the effective width of the inductance region.

$$t = \sigma[1 - exp(\frac{-h}{\sigma}] \tag{A.3}$$

(A.3) Is the effective thickness to which the electric field within the SRR can be considered to be uniform for the wave length and thicknesses we are working with.

$$l_{eff} = 2\pi a - d \tag{A.4}$$

(A.4) Is the effective ring length which is the circumference found from the effective radius of the inductance region and the width of the SRR gap.

$$A = \pi a^2 \tag{A.5}$$

(A.5) Is the equation for the area of the inductance region of the SRR for a circular SRR. This uses the radius from equation A.2.

$$L_s = \mu_0 \frac{A}{t} \tag{A.6}$$

(A.6) Is the self inductance of the SRR due to its geometric properties. The self inductance is proportional to the surface area of the inductance region.

$$L_{kin} = \frac{l_{eff}}{\varepsilon_0 \omega_p^2 w_{eff} t} \tag{A.7}$$

(A.7) Is the inductance from free electrons within the SRR. Is is dependant of the plasma frequency of the material (w_p), the effective ring length, the effective ring width (w_{eff}) and the effective thickness of the SRR (t).

$$L = L_s + L_{kin} \tag{A.8}$$

(A.8) The total inductance of the SRR is equal to the sum of the self inductance and the inductance of from the free electrons.

$$C = \varepsilon_0 \varepsilon_g \frac{w_g h}{d} \tag{A.9}$$

(A.9) The capacitance of an SRR is modelled as a plate capacitor.

$$\varepsilon_g = (n_{eff})^2 = (\alpha n_{medium} + (1 - \alpha) n_{substrate})^2 \tag{A.10}$$

(A.10) The permittivity of the SRR gap where n_{eff} is the effective index of the SRR gap, n_{medium} is the refractive index of the medium in the gap and $n_{substrate}$ is the refractive index of the substrate on which the SRR is fabricated upon. α is given as 0.82 [168].

$$f_{LC} = \frac{1}{2\pi\sqrt{LC}} \tag{A.11}$$

(A.11) The final equation or resonance of a SRR is equal to one over two pi multiplied by the reciprocal of the square root of the product of the capacitance and the total inductance.

References

[1] Lewis K. Piper, H. Johnson Singh, Jonathan R. C. Woods, Kai Sun, Otto L. Muskens, and Vasilis Apostolopoulos. Mechanically tunable terahertz metamaterial perfect absorber. *Advanced Photonics Research*, 2:2100136, 12 2021. ISSN 2699-9293. . URL https://onlinelibrary.wiley.com/doi/full/10.1002/adpr.202100136.

[2] Carlo Sirtori. Applied physics: Bridge for the terahertz gap. *Nature*, 417(6885): 132–133, may 2002. .

[3] S S Dhillon, M S Vitiello, E H Linfield, P Dean, A Valavanis, J Keeley, H A Hafez, X Chai, A Ibrahim, Nicholas Karpowicz, Hua Zhong, Jingzhou Xu, W Zouaghi, M D Thomson, K Rabia, John F Federici, Brian Schulkin, and Feng Huang. Imaging with terahertz radiation. *Rep. Prog. Phys*, 70, 2007.

[4] Hu Tao, A. C. Strikwerda, K. Fan, W. J. Padilla, X. Zhang, and R. D. Averitt. Reconfigurable terahertz metamaterials. *Physical Review Letters*, 103(14), 2009. .

[5] Tony Low and Phaedon Avouris. Graphene plasmonics for terahertz to mid-infrared applications. *ACS Nano*, 8(2):1086–1101, 2014. .

[6] Jason B. Baxter and Glenn W. Guglietta. Terahertz spectroscopy, jun 2011.

[7] W. J. Padilla, A. J. Taylor, C. Highstrete, Mark Lee, and R. D. Averitt. Dynamical electric and magnetic metamaterial response at terahertz frequencies. *Physical Review Letters*, 96(10), 2006. .

[8] Shi Wei Qu, Huan Yi, Bao Jie Chen, Kung Bo Ng, and Chi Hou Chan. Terahertz Reflecting and Transmitting Metasurfaces, jun 2017.

[9] Hou Tong Chen, John F. O'Hara, Abul K. Azad, and Antoinette J. Taylor. Manipulation of terahertz radiation using metamaterials, jul 2011.

[10] Ashish Y. Pawar, Deepak D. Sonawane, Kiran B. Erande, and Deelip V. Derle. Terahertz technology and its applications. *Drug Invention Today*, 5(2):157–163, 2013. .

[11] Michael C. Kemp, P. F. Taday, Bryan E. Cole, J. A. Cluff, Anthony J. Fitzgerald, and William R. Tribe. Security applications of terahertz technology. In R. Jennifer Hwu and Dwight L. Woolard, editors, *Terahertz for Military and Security Applications*, volume 5070, page 44. International Society for Optics and Photonics, aug 2003. .

[12] John F Federici, Brian Schulkin, Feng Huang, Dale Gary, Robert Barat, Filipe Oliveira, and David Zimdars. THz imaging and sensing for security applications—explosives, weapons and drugs. *Semiconductor Science and Technology*, 20 (7):S266–S280, jun 2005. .

[13] A. Giles Davies, Andrew D. Burnett, Wenhui Fan, Edmund H. Linfield, and John E. Cunningham. Terahertz spectroscopy of explosives and drugs. *Materials Today*, 11(3):18–26, mar 2008. .

[14] Peter H. Siegel. Terahertz technology in biology and medicine. *IEEE Transactions on Microwave Theory and Techniques*, 52(10):2438–2447, oct 2004. .

[15] Pawel Hlosta, Marcin Nita, Dorota Powala, and Waldemar Świderski. Terahertz radiation in non-destructive testing of composite pyrotechnic materials. *Composite Structures*, 279:114770, jan 2022. .

[16] Josette El Haddad, Frederick De Miollis, Joyce Bou Sleiman, Lionel Canioni, Patrick Mounaix, and Bruno Bousquet. Chemometrics applied to quantitative analysis of ternary mixtures by terahertz spectroscopy. *Analytical Chemistry*, 86 (10):4927–4933, may 2014. .

[17] Jana Orsavova, Ladislava Misurcova, Jarmila Vavra Ambrozova, Robert Vicha, and Jiri Mlcek. Fatty acids composition of vegetable oils and its contribution to dietary energy intake and dependence of cardiovascular mortality on dietary intake of fatty acids. *International Journal of Molecular Sciences*, 16(6):12871–12890, jun 2015. .

[18] Yongqiang Pang, Haifeng Cheng, Yongjiang Zhou, and Jun Wang. Analysis and enhancement of the bandwidth of ultrathin absorbers based on high-impedance surfaces. *Journal of Physics D: Applied Physics*, 45(21):5, 2012. .

[19] P. C. Upadhya, Y. C. Shen, A. G. Davies, and E. H. Linfield. Terahertz time-domain spectroscopy of glucose and uric acid. In *Journal of Biological Physics*, volume 29, pages 117–121, 2003. .

[20] Dong Kyu Lee, Ji Hun Kang, Jun Seok Lee, Hyo Seok Kim, Chulki Kim, Jae Hun Kim, Taikjin Lee, Joo Hiuk Son, Q. Han Park, and Minah Seo. Highly sensitive and selective sugar detection by terahertz nano-antennas. *Scientific Reports*, 5, oct 2015. .

[21] Ling Ding, Wen Hui Fan, Xu Chen, Ze You Chen, and Chao Song. Terahertz spectroscopy and solid-state density functional theory calculations of structural isomers: Nicotinic acid, isonicotinic acid and 2-picolinic acid. *Modern Physics Letters B*, 31(13):1750149, may 2017. .

[22] W Li Q Li X Yu H Xu Q Liu, Hui Xu, Quanwen Liu, Wenxin Li, Qingnuan Li, and Xiaohan Yu. THz time-domain spectroscopy of anthraquinone and its derivatives. *Chemistry*, 69(6):450–453, 2006.

[23] Maojiang Song, Fei Yang, Liping Liu, Li Shen, Pengfei Hu, and Feng Han. Chemical identification of non-esterified catechins by terahertz time domain spectroscopy. *Journal of Nanoscience and Nanotechnology*, 16(12):12208–12213, dec 2016. .

[24] Zhuan Ping Zheng, Wen Hui Fan, Hui Yan, Jia Liu, Li Min Xu, and H Yan J Liu L M Xu ZP Zheng WH Fan. Study on THz spectra and vibrational modes of benzoic acid and sodium Benzoate. *Spectrosc. Spectr. Anal.*, 33(3):582–585, 2013. .

[25] Jing Chen, Hai Nie, Cheng Peng, Shibin Qi, Chaojun Tang, Ying Zhang, Lianhui Wang, and Gun Sik Park. Enhancing the Magnetic Plasmon Resonance of Three-Dimensional Optical Metamaterials via Strong Coupling for High-Sensitivity Sensing. *Journal of Lightwave Technology*, 36(16):3481–3485, 2018. .

[26] M M Nazarov, A P Shkurinov, E A Kuleshov, and V V Tuchin. Terahertz time-domain spectroscopy of biological tissues. *Quantum Electronics*, 38(7):647–654, jul 2008. .

[27] Andrew D. Burnett, Wenhui Fan, Prashanth C. Upadhya, John E. Cunningham, Michael D. Hargreaves, Tasnim Munshi, Howell G.M. Edwards, Edmund H. Linfield, and A. Giles Davies. Broadband terahertz time-domain spectroscopy of drugs-of-abuse and the use of principal component analysis. *Analyst*, 134(8): 1658–1668, 2009. .

[28] Sachiko Nakajima, Hiromichi Hoshina, Masatsugu Yamashita, Chiko Otani, and Norio Miyoshi. Terahertz imaging diagnostics of cancer tissues with a chemometrics technique. *Applied Physics Letters*, 90(4):041102, 2007. .

[29] Ruth M. Woodward, Vincent P. Wallace, Richard J. Pye, Bryan E. Cole, Donald D. Arnone, Edmund H. Linfield, and Michael Pepper. Terahertz pulse imaging of ex vivo basal cell carcinoma. *Journal of Investigative Dermatology*, 120(1):72–78, jan 2003. .

[30] Chao Song, Wen Hui Fan, Ling Ding, Xu Chen, Ze You Chen, and Kai Wang. Terahertz and infrared characteristic absorption spectra of aqueous glucose and fructose solutions. *Scientific Reports*, 8(1):1–8, dec 2018. .

[31] Philip F. Taday, I. V. Bradley, D. D. Arnone, and M. Pepper. Using Terahertz pulse spectroscopy to study the crystalline structure of a drug: A case study of the polymorphs of ranitidine hydrochloride. *Journal of Pharmaceutical Sciences*, 92 (4):831–838, apr 2003. .

[32] Clare J. Strachan, Philip F. Taday, David A. Newnham, Keith C. Gordon, J. Axel Zeitler, Michael Pepper, and Thomas Rades. Using terahertz pulsed spectroscopy to quantify pharmaceutical polymorphism and crystallinity. *Journal of Pharmaceutical Sciences*, 94(4):837–846, 2005. .

[33] P. F. Taday, I. V. Bradley, and D. D. Arnone. Terahertz pulse spectroscopy of biological materials: L-glutamic acid. In *Journal of Biological Physics*, volume 29, pages 109–115, 2003. .

[34] Robert K. May, Michael J. Evans, Shuncong Zhong, Ian Warr, Lynn F. Gladden, Yaochun Shen, and J. Axel Zeitler. Terahertz in-line sensor for direct coating thickness measurement of individual tablets during film coating in real-time. *Journal of Pharmaceutical Sciences*, 100(4):1535–1544, 2011. .

[35] Edward P.J. Parrott, K. Lien Nguyen, Tomislav Friščić, J. Axel Zeitler, Michael Pepper, William Jones, and Lynn F. Gladden. Using terahertz time-domain spectroscopy to identify pharmaceutical cocrystals. In *IRMMW-THz2007 - Conference Digest of the Joint 32nd International Conference on Infrared and Millimetre Waves, and 15th International Conference on Terahertz Electronics*, pages 660–661, 2007. ISBN 1424414385. .

[36] Clare J. Strachan, Thomas Rades, David A. Newnham, Keith C. Gordon, Michael Pepper, and Philip F. Taday. Using terahertz pulsed spectroscopy to study crystallinity of pharmaceutical materials. *Chemical Physics Letters*, 390(1-3):20–24, may 2004. .

[37] Tuononen Heikki, Fukunaga Kaori, Kuosmanen Marko, Ketolainen Jarkko, and Kai Erik Peiponen. Wiener bounds for complex permittivity in terahertz spectroscopy: Case study of two-phase pharmaceutical tablets. *Applied Spectroscopy*, 64(1):127–131, jan 2010. .

[38] Aifeng Ren, Adnan Zahid, Dou Fan, Xiaodong Yang, Muhammad Ali Imran, Akram Alomainy, and Qammer H. Abbasi. State-of-the-art in terahertz sensing for food and water security – a comprehensive review. *Trends in Food Science Technology*, 85:241–251, 2019. .

[39] Seung Hyun Baek, Ju Hee Kang, Yeun Hee Hwang, Kang, Min Ok, Kyungwon Kwak, Hyang Sook Chun, * Hyang, and Sook Chun. Detection of Methomyl, a Carbamate Insecticide, in Food Matrices Using Terahertz Time-Domain Spectroscopy. *J Infrared Milli Terahz Waves*, 37:486–497, 2016. .

[40] Honglei Zhan, Jianfeng Xi, Kun Zhao, Rima Bao, and Lizhi Xiao. A spectral-mathematical strategy for the identification of edible and swill-cooked dirty oils using terahertz spectroscopy. *Food Control*, 67:114–118, sep 2016. .

[41] Alex Dinovitser, Dimitar G. Valchev, and Derek Abbott. Terahertz time-domain spectroscopy of edible oils. *Royal Society Open Science*, 4(6), jun 2017. .

[42] Ming Yin, Shoufeng Tang, and Minming Tong. Identification of edible oils using terahertz spectroscopy combined with genetic algorithm and partial least squares discriminant analysis. *Analytical Methods*, 8(13):2794–2798, apr 2016. .

[43] Mingliang Li, Guangbin Dai, Tianying Chang, Changcheng Shi, Dongshan Wei, Chunlei Du, and Hong Liang Cui. Accurate determination of geographical origin of tea based on terahertz spectroscopy. *Applied Sciences (Switzerland)*, 7(2):172, 2017. .

[44] Yuying Jiang, Hongyi Ge, Feiyu Lian, Yuan Zhang, and Shanhong Xia. Early detection of germinated wheat grains using terahertz image and chemometrics. *Scientific Reports*, 6, feb 2016. .

[45] L. I. Jiusheng. Optical parameters of vegetable oil studied by terahertz time-domain spectroscopy. *Applied Spectroscopy*, 64(2):231–234, 2010. .

[46] Ben Xin Wang, Gui Zhen Wang, Tian Sang, and Ling Ling Wang. Six-band terahertz metamaterial absorber based on the combination of multiple-order responses of metallic patches in a dual-layer stacked resonance structure. *Scientific Reports*, 7, 2017. .

[47] Weiwei Liu, Bing Wang, Shaolin Ke, Chengzhi Qin, Hua Long, Kai Wang, and Peixiang Lu. Enhanced plasmonic nanofocusing of terahertz waves in tapered graphene multilayers. *Optics Express*, 24(13):14765, jun 2016. .

[48] Mehdi Hasan, Sara Arezoomandan, Hugo Condori, and Berardi Sensale-Rodriguez. Graphene terahertz devices for communications applications, 2016.

[49] Farnoosh Moshir and Suresh Singh. Modulation and rate adaptation algorithms for terahertz channels, 2016.

[50] Anna Maria Vegni and Valeria Loscrí. Chirality effects on channel modeling for THz-band wireless communications in LoS/NLoS propagation, 2016.

[51] Kao Cheng Huang and Zhaocheng Wang. Terahertz terabit wireless communication. *IEEE Microwave Magazine*, 12(4):108–116, jun 2011. .

[52] Tadao Nagatsuma, Guillaume Ducournau, and Cyril C. Renaud. Advances in terahertz communications accelerated by photonics. *Nature Photonics*, 10(6):371–379, jun 2016. .

[53] Yong Niu, Yong Li, Depeng Jin, Li Su, and Athanasios V. Vasilakos. A survey of millimeter wave communications (mmWave) for 5G: opportunities and challenges. *Wireless Networks*, 21(8):2657–2676, nov 2015. .

[54] Alwyn J. Seeds, Haymen Shams, Martyn J. Fice, and Cyril C. Renaud. TeraHertz photonics for wireless communications. *Journal of Lightwave Technology*, 33(3): 579–587, feb 2015. .

[55] Thomas Kürner and Sebastian Priebe. Towards THz communications - Status in research, standardization and regulation. *Journal of Infrared, Millimeter, and Terahertz Waves*, 35(1):53–62, 2014. .

[56] S. Ummethala, T. Harter, K. Koehnle, Z. Li, S. Muehlbrandt, Y. Kutuvantavida, J. Kemal, P. Marin-Palomo, J. Schaefer, A. Tessmann, S. K. Garlapati, A. Bacher, L. Hahn, M. Walther, T. Zwick, S. Randel, W. Freude, and C. Koos. THz-to-optical conversion in wireless communications using an ultra-broadband plasmonic modulator, aug 2019.

[57] E. Abraham, A. Younus, J. C. Delagnes, and P. Mounaix. Non-invasive investigation of art paintings by terahertz imaging. *Applied Physics A: Materials Science and Processing*, 100(3):585–590, 2010. .

[58] S. Koenig, D. Lopez-Diaz, J. Antes, F. Boes, R. Henneberger, A. Leuther, A. Tessmann, R. Schmogrow, D. Hillerkuss, R. Palmer, T. Zwick, C. Koos, W. Freude, O. Ambacher, J. Leuthold, and I. Kallfass. Wireless sub-THz communication system with high data rate. *Nature Photonics*, 7(12):977–981, dec 2013. .

[59] Craig Kulesa. Terahertz spectroscopy for astronomy: From comets to cosmology. *IEEE Transactions on Terahertz Science and Technology*, 1(1):232–240, sep 2011. .

[60] Yukio Kawano. Terahertz waves: a tool for condensed matter, the life sciences and astronomy, jun 2013.

[61] X. C. Zhang. Terahertz wave imaging: Horizons and hurdles. *Physics in Medicine and Biology*, 47(21):3667–3677, 2002. .

[62] Alan W.M. Lee, Qi Qin, Sushil Kumar, Benjamin S. Williams, Qing Hu, and John L. Reno. Real-time terahertz imaging over a standoff distance (¿25 meters). *Applied Physics Letters*, 89(14):141125, oct 2006. .

[63] C M Soukoulis, S Linden, and M Wegener. Negative Refractive Index at Optical Wavelengths. *Science*, 315(5808):47–49, 2007.

[64] Hou-Tong Chen, Antoinette J Taylor, and Nanfang Yu. A review of metasurfaces: physics and applications. *Rep. Prog. Phys.*, 79(7):076401, jun 2016. .

[65] Seojoo Lee, Soojeong Baek, Teun-Teun Kim, Hyukjoon Cho, Sangha Lee, Ji-Hun Kang, and Bumki Min. Metamaterials for enhanced optical responses and their application to active control of terahertz waves. *Adv. Mater.*, 32(35):2000250, 2020. .

[66] Qian Ma and Tie Jun Cui. Information Metamaterials: bridging the physical world and digital world. *PhotoniX*, 1:1–32, dec 2020. .

[67] Xing Lin, Yair Rivenson, Nezih T. Yardimci, Muhammed Veli, Yi Luo, Mona Jarrahi, and Aydogan Ozcan. All-optical machine learning using diffractive deep neural networks. *Science*, 361(6406):1004–1008, sep 2018. .

[68] Willie J. Padilla, Dimitri N. Basov, and David R. Smith. Negative refractive index metamaterials. *Materials Today*, 9(7):28–35, 2006. .

[69] Vladimir M. Shalaev. Optical negative-index metamaterials. *Nature Photonics 2006 1:1*, 1(1):41–48, jan 2007. .

[70] Fei Ding, Yanxia Cui, Xiaochen Ge, Yi Jin, and Sailing He. Ultra-broadband microwave metamaterial absorber. *Applied Physics Letters*, 100(10):251104–103506, 2012. .

[71] Jé ré my Butet, Pierre-Franc -ois Brevet, and Olivier J F Martin. Optical Second Harmonic Generation in Plasmonic Nanostructures: From Fundamental Principles to Advanced Applications. 12:5, 2021. .

[72] Nikolay I. Zheludev and Yuri S. Kivshar. From metamaterials to metadevices. *Nature Materials*, 11(11):917–924, 2012. .

[73] Koray Aydin, Vivian E. Ferry, Ryan M. Briggs, and Harry A. Atwater. Broadband polarization-independent resonant light absorption using ultrathin plasmonic super absorbers. *Nat. Comm.*, 2(1):517, 2011. .

[74] Andreas Tittl, Patrick Mai, Richard Taubert, Daniel Dregely, Na Liu, and Harald Giessen. Palladium-based plasmonic perfect absorber in the visible wavelength range and its application to hydrogen sensing. *Nano Lett.*, 11(10):4366–4369, oct 2011. .

[75] Joel T. Collins, David C. Hooper, Andrew G. Mark, Christian Kuppe, and Ventsislav K. Valev. Second-Harmonic Generation Optical Rotation Solely Attributable to Chirality in Plasmonic Metasurfaces. *ACS Nano*, 12(6):5445–5451, 2018. .

[76] E. Plum, J. Zhou, J. Dong, V. A. Fedotov, T. Koschny, C. M. Soukoulis, and N. I. Zheludev. Metamaterial with negative index due to chirality. *Physical Review B - Condensed Matter and Materials Physics*, 79(3), 2009. .

[77] Kai Sun, Christoph A. Riedel, Yudong Wang, Alessandro Urbani, Mirko Simeoni, Sandro Mengali, Maksim Zalkovskij, Brian Bilenberg, C. H. de Groot, and Otto L. Muskens. Metasurface optical solar reflectors using azo transparent conducting oxides for radiative cooling of spacecraft. *ACS Photonics*, 5(2):495–501, 2018. .

[78] N. I. Landy, S. Sajuyigbe, J. J. Mock, D. R. Smith, and W. J. Padilla. Perfect metamaterial absorber. *Physical Review Letters*, 100(20), 2008. .

[79] Osman Balci, Nurbek Kakenov, Ertugrul Karademir, Sinan Balci, Semih Cakmakyapan, Emre O. Polat, Humeyra Caglayan, Ekmel Ozbay, and Coskun Kocabas. Electrically switchable metadevices via graphene. *Sci. Adv.*, 4(1):eaao1749, jan 2018. .

[80] Chenggang Hu, Liyuan Liu, Zeyu Zhao, Xu'nan Chen, and Xiangang Luo. Mixed plasmons coupling for expanding the bandwidth of near-perfect absorption at visible frequencies. *Opt. Express*, 17(19):16745–16749, Sep 2009. .

[81] Ahmmed A. Rifat, Mohsen Rahmani, Lei Xu, and Andrey E. Miroshnichenko. Hybrid metasurface based tunable near-perfect absorber and plasmonic sensor. *Materials*, 11(7):1091, jun 2018. .

[82] Khagendra Bhattarai, Sinhara Silva, Kun Song, Augustine Urbas, Sang Jun Lee, Zahyun Ku, and Jiangfeng Zhou. Metamaterial Perfect Absorber Analyzed by a Meta-cavity Model Consisting of Multilayer Metasurfaces. *Scientific Reports*, 7(1): 1–9, dec 2017. .

[83] Xingcun Colin Tong. *Concepts From Metamaterials to Functional Metadevices*, pages 1–21. Springer International Publishing, Cham, 2018. ISBN 978-3-319-66044-8. .

[84] Huanyang Chen, D Schurig, J J Mock, B J Justice, S A Cummer, J B Pendry, A F Starr, and D R Smith. Experimental verification of a negative index of refraction. *Phys. Rev. Lett*, 85(18):1780–1782, 2009. .

[85] Sher Yi Chiam, Ranjan Singh, Carsten Rockstuhl, Falk Lederer, Weili Zhang, and Andrew A. Bettiol. Analogue of electromagnetically induced transparency in a terahertz metamaterial. *Physical Review B - Condensed Matter and Materials Physics*, 80(15), 2009. .

[86] C. Rockstuhl, T. Zentgraf, H. Guo, N. Liu, C. Etrich, I. Loa, K. Syassen, J. Kuhl, F. Lederer, and H. Giessen. Resonances of split-ring resonator metamaterials in the near infrared. *Appl. Phys. B*, 84(1-2):219–227, jul 2006. .

[87] Claire M. Watts, Xianliang Liu, and Willie J. Padilla. Metamaterial electromagnetic wave absorbers. *Advanced Materials*, 24(23):OP98–OP120, jun 2012. .

[88] Yu Yao, Raji Shankar, Mikhail A. Kats, Yi Song, Jing Kong, Marko Loncar, and Federico Capasso. Electrically tunable metasurface perfect absorbers for ultrathin mid-infrared optical modulators. *Nano Letters*, 14(11):6526–6532, nov 2014. .

[89] Jeremy A. Bossard, Lan Lin, Seokho Yun, Liu Liu, Douglas H. Werner, and Theresa S. Mayer. Near-ideal optical metamaterial absorbers with super-octave bandwidth. *ACS Nano*, 8(2):1517–1524, 2014. .

[90] Mikhail A. Kats, Deepika Sharma, Jiao Lin, Patrice Genevet, Romain Blanchard, Zheng Yang, M. Mumtaz Qazilbash, D. N. Basov, Shriram Ramanathan, and Federico Capasso. Ultra-thin perfect absorber employing a tunable phase change material. *Applied Physics Letters*, 101(22):221101, 2012. .

[91] G P Williams and ; M Tonouchi. Subwavelength structures; (110.6795) Terahertz Imaging; (160.1890) Detector Materials; (160.3918) Metamaterials; (260.5740) Resonance. References and links 1. Technical Report C, 2006.

[92] Xiaofei Zang, Cheng Shi, Lin Chen, Bin Cai, Yiming Zhu, and Songlin Zhuang. Ultra-broadband terahertz absorption by exciting the orthogonal diffraction in dumbbell-shaped gratings. *Scientific Reports*, 5:8901, mar 2015. .

[93] Leopoldo Angrisani, Giovanni Cavallo, Annalisa Liccardo, Gian Paolo Papari, and Antonello Andreone. THz Measurement Systems. jul 2016. .

[94] Mohammad P. Hokmabadi, Soner Balci, Juhyung Kim, Elizabath Philip, Elmer Rivera, Muliang Zhu, Patrick Kung, and Seongsin M. Kim. Terahertz metamaterials: design, implementation, modeling and applications. In Mehdi F. Anwar, Thomas W. Crowe, and Tariq Manzur, editors, *Terahertz Physics, Devices, and Systems X: Advanced Applications in Industry and Defense*, volume 9856, page 98560B. International Society for Optics and Photonics, may 2016. ISBN 9781510600973. .

[95] Peter H. Siegel. Terahertz technology, mar 2002.

[96] Masayoshi Tonouchi. Cutting-edge terahertz technology. *Nature Photonics 2007 1:2*, 1(2):97–105, feb 2007. .

[97] Sumeet Walia, Charan M. Shah, Philipp Gutruf, Hussein Nili, Dibakar Roy Chowdhury, Withawat Withayachumnankul, Madhu Bhaskaran, and Sharath Sriram. Flexible metasurfaces and metamaterials: A review of materials and fabrication processes at micro- and nano-scales. *Applied Physics Reviews*, 2(1):11303, 2015. .

[98] Imogen M. Pryce, Koray Aydin, Yousif A. Kelaita, Ryan M. Briggs, and Harry A. Atwater. Highly strained compliant optical metamaterials with large frequency tunability. *Nano Letters*, 10(10):4222–4227, 2010. .

[99] Prakash Pitchappa, Chong Pei Ho, Piotr Kropelnicki, Navab Singh, Dim Lee Kwong, and Chengkuo Lee. Micro-electro-mechanically switchable near infrared complementary metamaterial absorber. *Applied Physics Letters*, 104(20):201114, 2014. .

[100] Prakash Pitchappa, Chong Pei Ho, Yu Sheng Lin, Piotr Kropelnicki, Chia Yi Huang, Navab Singh, and Chengkuo Lee. Micro-electro-mechanically tunable metamaterial with enhanced electro-optic performance. *Applied Physics Letters*, 104(15):151104, 2014. .

[101] Kailing Shih, Prakash Pitchappa, Manukumara Manjappa, Chong Pei Ho, Ranjan Singh, Bin Yang, Navab Singh, and Chengkuo Lee. Active MEMS metamaterials for THz bandwidth control. *Applied Physics Letters*, 110(16):161108, 2017. .

[102] H. Němec, P. Kužel, F. Kadlec, C. Kadlec, R. Yahiaoui, and P. Mounaix. Tunable terahertz metamaterials with negative permeability. *Physical Review B*, 79(24), 2009. .

[103] Hou Tong Chen, Willie J. Padilla, Michael J. Cich, Abul K. Azad, Richard D. Averitt, and Antoinette J. Taylor. A metamaterial solid-state terahertz phase modulator. *Nature Photonics*, 3(3):148–151, 2009. .

[104] Sukang Bae, Hyeongkeun Kim, Youngbin Lee, Xiangfan Xu, Jae Sung Park, Yi Zheng, Jayakumar Balakrishnan, Tian Lei, Hye Ri Kim, Young Il Song, Young Jin Kim, Kwang S. Kim, Barbaros Özyilmaz, Jong Hyun Ahn, Byung Hee Hong, and Sumio Iijima. Roll-to-roll production of 30-inch graphene films for transparent electrodes. *Nature Nanotechnology*, 5(8):574–578, 2010. .

[105] A K Geim. Graphene: Status and Prospects. Technical report.

[106] Kuan I. Ho, Mohamed Boutchich, Ching Yuan Su, Rosalia Moreddu, Eugene Sebastian Raj Marianathan, Laurent Montes, and Chao Sung Lai. A Self-Aligned High-Mobility Graphene Transistor: Decoupling the Channel with Fluorographene to Reduce Scattering. *Advanced Materials*, 27(41):6519–6525, 2015. .

[107] Sergei Tretyakov. On geometrical scaling of split-ring and double-bar resonators at optical frequencies. *Metamaterials*, 1(1):40–43, 2007. .

[108] S F Mingaleev, L Tkeshelashvili, and M Wegener. Dependence of LC resonance wavelength on size of silver split-ring resonator fabricated by nanosphere lithography. Technical Report 11, 1999.

[109] Basudev Lahiri, Scott G McMeekin, Ali Z Khokhar, Richard M De La Rue, Nigel P Johnson, J B Pendry, A J Holden, D J Robbins, W J Stewart, S Linden, C Enkrich, M Wegener, J Zhou, T Koschny, C M Soukoulis, G Dolling, M W Klein, S Burger, and F Schmidt. Magnetic response of split ring resonators (SRRs) at visible frequencies . Technical Report 4, 1968.

[110] T. P. Meyrath, T. Zentgraf, and H. Giessen. Lorentz model for metamaterials: Optical frequency resonance circuits. *Physical Review B - Condensed Matter and Materials Physics*, 75(20), 2007. .

[111] K. Busch, G. von Freymann, S. Linden, S. F. Mingaleev, L. Tkeshelashvili, and M. Wegener. Periodic nanostructures for photonics. *Physics Reports*, 444(3-6): 101–202, 2007. .

[112] Toshihiro Okamoto, Tomoya Otsuka, Shuji Sato, Tetsuya Fukuta, and Masanobu Haraguchi. Dependence of LC resonance wavelength on size of silver split-ring resonator fabricated by nanosphere lithography. *Optics Express*, 20(21):24059, oct 2012. .

[113] Ellen J. Zeman, George C. Schatz, Cd J Ellen Zeman, and George C. Schatz. An Accurate Electromagnetic Theory Study of Surface Enhancement Factors for. *J. Phys. Chem*, 91(3):634–643, 1987. .

[114] M. A. Ordal, Robert J. Bell, R. W. Alexander, L. L. Long, and M. R. Querry. Optical properties of fourteen metals in the infrared and far infrared: Al, Co, Cu, Au, Fe, Pb, Mo, Ni, Pd, Pt, Ag, Ti, V, and W. *Applied Optics*, 24(24):4493, 1985. .

[115] Maxwell J. Mageto, C. M. Maghanga, and Mghendi Mwamburi. The lorentz oscillator model simulation illustrating a broad maximum in the bulk reflectance for frequencies just above the resonance frequency. *African Review of Physics*, 7: 95–105, 2012.

[116] H. Tanoto, J. H. Teng, Q. Y. Wu, M. Sun, Z. N. Chen, S. A. Maier, B. Wang, C. C. Chum, G. Y. Si, A. J. Danner, and S. J. Chua. Greatly enhanced continuous-wave terahertz emission by nano-electrodes in a photoconductive photomixer. *Nature Photonics*, 6(2):121–126, jan 2012. .

[117] H. Tanoto, J. H. Teng, Q. Y. Wu, M. Sun, Z. N. Chen, S. A. Maier, B. Wang, C. C. Chum, G. Y. Si, A. J. Danner, and S. J. Chua. Nano-antenna in a photoconductive photomixer for highly efficient continuous wave terahertz emission. *Scientific Reports*, 3(1):1–6, oct 2013. .

[118] Benjamin S. Williams. Terahertz quantum-cascade lasers, sep 2007.

[119] Aniela Dunn, Caroline Poyser, Paul Dean, Aleksandar Demić, Alexander Valavanis, Dragan Indjin, Mohammed Salih, Iman Kundu, Lianhe Li, Andrey Akimov, Alexander Giles Davies, Edmund Linfield, John Cunningham, and Anthony Kent. High-speed modulation of a terahertz quantum cascade laser by coherent acoustic phonon pulses. *Nature Communications*, 11(1):1–8, dec 2020. .

[120] Maria T. Schlecht, Sascha Preu, Stefan Malzer, and Heiko B. Weber. An efficient Terahertz rectifier on the graphene/SiC materials platform. *Scientific reports*, 9(1): 11205, 2019. .

[121] Youngeun Jeon, Sungchul Jung, Hanbyul Jin, Kyuhyung Mo, Kyung Rok Kim, Wook Ki Park, Seong Tae Han, and Kibog Park. Highly-Sensitive Thin Film THz

Detector Based on Edge Metal-Semiconductor-Metal Junction. *Scientific Reports*, 7(1):1–8, dec 2017. .

[122] Imran Mehdi, Jose V. Siles, Choonsup Lee, and Erich Schlecht. THz diode technology: Status, prospects, and applications, jun 2017.

[123] Li Guo Zhu, Brian Kubera, Kin Fai Mak, and Jie Shan. Effect of surface states on terahertz emission from the Bi2Se3 surface. *Scientific Reports*, 5(1):1–8, may 2015. .

[124] Soon Hee Park, Sun Young Hamh, Joonbum Park, Jun Sung Kim, and Jong Seok Lee. Possible flat band bending of the Bi1.5Sb0.5Te1.7Se1.3 crystal cleaved in an ambient air probed by terahertz emission spectroscopy. *Scientific Reports*, 6(1): 1–8, nov 2016. .

[125] Mohammad Bashirpour, Matin Forouzmehr, Seyed Ehsan Hosseininejad, Mohammadreza Kolahdouz, and Mohammad Neshat. Improvement of Terahertz Photoconductive Antenna using Optical Antenna Array of ZnO Nanorods. *Scientific Reports*, 9(1):1–8, dec 2019. .

[126] Sergey Lepeshov, Andrei Gorodetsky, Alexander Krasnok, Nikita Toropov, Tigran A. Vartanyan, Pavel Belov, Andrea Alú, and Edik U. Rafailov. Boosting Terahertz Photoconductive Antenna Performance with Optimised Plasmonic Nanostructures. *Scientific Reports*, 8(1):1–7, dec 2018. .

[127] P. U. Jepsen, D. G. Cooke, and M. Koch. Terahertz spectroscopy and imaging - Modern techniques and applications. *Laser and Photonics Reviews*, 5(1):124–166, jan 2011. .

[128] Francis Hindle, Arnaud Cuisset, Robin Bocquet, and Gaël Mouret. Continuous-wave terahertz by photomixing: applications to gas phase pollutant detection and quantification. *Comptes Rendus Physique*, 9(2):262–275, mar 2008. .

[129] Masahiko Tani, Osamu Morikawa, Shuji Matsuura, and Masanori Hangyo. Generation of terahertz radiation by photomixing with dual- and multiple-mode lasers. *Semiconductor Science and Technology*, 20(7), 2005. .

[130] Y. R. Shen. Far-infrared generation by optical mixing. *Progress in Quantum Electronics*, 4(PART 3):207–232, jan 1976. .

[131] Jerome Faist, Federico Capasso, Deborah L. Sivco, Carlo Sirtori, Albert L. Hutchinson, and Alfred Y. Cho. Quantum cascade laser. *Science*, 264:553–556, 1994. .

[132] Alfred Y. Cho, Claire Gmachl, Deborah L. Sivco, Federico Capasso, James F. Kelly, James N. Baillargeon, John L. Hall, John S. Hartman, Matthew S. Taubman,

Richard M. Williams, and Steven W. Sharpe. Kilohertz linewidth from frequency-stabilized mid-infrared quantum cascade lasers. *Optics Letters, Vol. 24, Issue 24, pp. 1844-1846*, 24:1844–1846, 12 1999. .

[133] Rüdeger Köhler, Alessandro Tredicucci, Fablo Beltram, Harvey E. Beere, Edmund H. Linfield, A. Giles Davies, David A. Ritchie, Rita C. Iotti, and Fausto Rossi. Terahertz semiconductor-heterostructure laser. *Nature 2002 417:6885*, 417: 156–159, 5 2002. .

[134] Benjamin S. Williams, Sushil Kumar, Qing Hu, and John L. Reno. Operation of terahertz quantum-cascade lasers at 164 k in pulsed mode and at 117 k in continuous-wave mode. *Opt. Express*, 13(9):3331–3339, May 2005. .

[135] Giacomo Scalari, Christoph Walther, Milan Fischer, Romain Terazzi, Harvey Beere, David Ritchie, and Jérôme Faist. Thz and sub-thz quantum cascade lasers. *Laser and Photonics Reviews*, 3:45–66, 2009. .

[136] R A Soref and D H Mcmahon. Optical Design of Wollaston-Prism Digital Light Deflectors.

[137] Carole C Montarou and Thomas K Gaylord. Analysis and design of modified Wollaston prisms. 1999.

[138] Marcel J E Golay. Theoretical consideration in heat and infra-red detection, with particular reference to the pneumatic detector articles you may be interested in. *Review of Scientific Instruments*, 18:347, 1947. .

[139] Jon Gorecki, Nicholas Klokkou, Lewis Piper, Sakellaris Mailis, Nikitas Papasimakis, and Vasilis Apostolopoulos. High-precision THz-TDS via self-referenced transmission echo method. *Applied Optics*, 59(22):6744, aug 2020. .

[140] Moumita Dutta, Carol Ellis, Xomalin G. Peralta, Amar Bhalla, and Ruyan Guo. Terahertz electrical and optical properties of LiNbO3 single crystal thin films. In Shizhuo Yin and Ruyan Guo, editors, *Photonic Fiber and Crystal Devices: Advances in Materials and Innovations in Device Applications IX*, volume 9586, pages 28 – 37. International Society for Optics and Photonics, SPIE, 2015. .

[141] Guang hao Shao, Shi jun Ge, Yun chao Shi, Wei Hu, and Yan qing Lu. Extended cauchy equations of congruent linbo3 in the terahertz band and their applications. *Opt. Mater. Express*, 6(12):3766–3775, Dec 2016. .

[142] Márta Unferdorben, Zsuzsanna Szaller, Ivett Hajdara, János Hebling, and László Pálfalvi. Measurement of Refractive Index and Absorption Coefficient of Congruent and Stoichiometric Lithium Niobate in the Terahertz Range. .

[143] Sun Yi-Min, Mao Zong-Liang, Hou Bi-Hui, Liu Guo-Qing, and Wang Li. Giant birefringence of lithium niobate crystals in the terahertz region. *Chinese Physics Letters*, 24(2):414–417, jan 2007. .

[144] Fuli Zhang, Shuqi Feng, Kepeng Qiu, Zijun Liu, Yuancheng Fan, Weihong Zhang, Qian Zhao, and Ji Zhou. Mechanically stretchable and tunable metamaterial absorber. *Appl. Phys. Lett.*, 106(9):091907, 2015. .

[145] Ming Lei, Ningyue Feng, Qingmin Wang, Yanan Hao, Shanguo Huang, and Ke Bi. Magnetically tunable metamaterial perfect absorber. *J. Appl. Phys.*, 119 (24), 2016. .

[146] Yong Ma, Qin Chen, James Grant, Shimul C. Saha, A. Khalid, and David R. S. Cumming. A terahertz polarization insensitive dual band metamaterial absorber. *Opt. Lett.*, 36(6):945, 2011. .

[147] Mingkai Liu, Mohamad Susli, Dilusha Silva, Gino Putrino, Hemendra Kala, Shuting Fan, Michael Cole, Lorenzo Faraone, Vincent P. Wallace, Willie J. Padilla, David A. Powell, Ilya V. Shadrivov, and Mariusz Martyniuk. Ultrathin tunable terahertz absorber based on MEMS-driven metamaterial. *Microsyst. Nanoeng.*, 3: 17033, 2017. .

[148] Jacob Schalch, Guangwu Duan, Xiaoguang Zhao, Xin Zhang, and Richard D. Averitt. Terahertz metamaterial perfect absorber with continuously tunable air spacer layer. *Appl. Phys. Lett.*, 113:061113, 2018. .

[149] Longqing Cong, Prakash Pitchappa, Chengkuo Lee, and Ranjan Singh. Active phase transition via loss engineering in a terahertz mems metamaterial. *Adv. Mater.*, 29(26):1700733, 2017. .

[150] Longqing Cong, Prakash Pitchappa, Yang Wu, Lin Ke, Chengkuo Lee, Navab Singh, Hyunsoo Yang, and Ranjan Singh. Active multifunctional microelectromechanical system metadevices: Applications in polarization control, wavefront deflection, and holograms. *Adv. Opt. Mater.*, 5(2):1600716, 2017. .

[151] Constantine A. Balanis. *(PDF) Antenna Theory Analysis and Design(3rd Edition) — jonathan martinez moreno - Academia.edu*, volume 1. A JOHN WILEY SONS, INC.,, 3rd edition, 2005. URL https://www.academia.edu/19892973/Antenna_Theory_Analysis_and_Design_3rd_Edition_.

[152] Hou-Tong Chen. Interference theory of metamaterial perfect absorbers. *Opt. Express*, 20(7):7165–7172, Mar 2012. .

[153] Rasoul Alaee, Mohammad Albooyeh, and Carsten Rockstuhl. Theory of metasurface based perfect absorbers. *Journal of Physics D: Applied Physics*, 50(50):503002, 2017. .

[154] Mai O. Sallam, Guy A. E. Vandenbosch, Georges Gielen, and Ezzeldin A. Soliman. Integral equations formulation of plasmonic transmission lines. *Optics Express*, 22(19):22388, sep 2014. .

[155] Hu Tao, C. M. Bingham, A. C. Strikwerda, D. Pilon, D. Shrekenhamer, N. I. Landy, K. Fan, X. Zhang, W. J. Padilla, and R. D. Averitt. Highly flexible wide angle of incidence terahertz metamaterial absorber: Design, fabrication, and characterization. *Physical Review B - Condensed Matter and Materials Physics*, 78(24), 2008. .

[156] Nathan M. Burford and Magda O. El-Shenawee. Review of terahertz photoconductive antenna technology. *Optical Engineering*, 56(1):010901, jan 2017. .

[157] Eugene Hecht. *Optics*. 5 ed. edition, 2017. ISBN 9780133977226.

[158] Hou-Tong Chen. Interference theory of metamaterial perfect absorbers. *Opt. Express*, 20(7):7165–7172, Mar 2012. .

[159] Longqing Cong, Siyu Tan, Riad Yahiaoui, Fengping Yan, Weili Zhang, and Ranjan Singh. Experimental demonstration of ultrasensitive sensing with terahertz metamaterial absorbers: A comparison with the metasurfaces. *Appl. Phys. Lett.*, 106(3):031107, 2015. .

[160] Jon Gorecki, Lewis Piper, Adnane Noual, Sakellaris Mailis, Nikitas Papasimakis, and Vasilis Apostolopoulos. Optically Reconfigurable Graphene/Metal Metasurface on Fe:LiNbO3for Adaptive THz Optics. *ACS Applied Nano Materials*, 3(9): 9494–9501, 2020. .

[161] Thomas Bifano. Adaptive imaging: Mems deformable mirrors. *Nature Photonics*, 5, 01 2011. .

[162] Dan Hewak, Daniel Lawson, Ioannis Zeimpekis, Matthew Delaney, and Otto Muskens. Sb2S3 and Sb3Se3 as Next Generation Low Loss Phase Change Materials for Photonic Applications. *OSA Advanced Photonics Congress (AP) 2020 (IPR, NP, NOMA, Networks, PVLED, PSC, SPPCom, SOF) (2020), paper NoTh2C.3*, Part F186-NOMA 2020:NoTh2C.3, jul 2020. .

[163] Matthew Delaney, Ioannis Zeimpekis, Daniel Lawson, Daniel W. Hewak, and Otto L. Muskens. A New Family of Ultralow Loss Reversible Phase-Change Materials for Photonic Integrated Circuits: Sb2S3 and Sb2Se3. *Advanced Functional Materials*, 30(36):2002447, sep 2020. .

[164] Qian Wang, Edward T.F. F Rogers, Behrad Gholipour, Chih-Ming Ming Wang, Guanghui Yuan, Jinghua Teng, and Nikolay I. Zheludev. Optically reconfigurable metasurfaces and photonic devices based on phase change materials. *Nature Photonics*, 10(1):60–65, 2016. .

[165] Prakash Pitchappa, Abhishek Kumar, Saurav Prakash, Hariom Jani, Thirumalai Venkatesan, and Ranjan Singh. Chalcogenide Phase Change Material for Active Terahertz Photonics. *Advanced Materials*, 31(12):1808157, mar 2019. .

[166] Behrad Gholipour, Jianfa Zhang, Kevin F. MacDonald, Daniel W. Hewak, and Nikolay I. Zheludev. An all-optical, non-volatile, bidirectional, phase-change meta-switch. *Advanced Materials*, 25(22):3050–3054, jun 2013. .

[167] Demetri Psaltis, Dirk Berben, Karsten Buse, Marc Luennemann, Ulrich Hartwig, and Yunping Yang. Photorefractive properties of lithium niobate crystals doped with manganese. *JOSA B, Vol. 20, Issue 7, pp. 1491-1502*, 20(7):1491–1502, jul 2003. .

[168] A Curry, G Nusz, A Chilkoti, and A Wax. Substrate effect on refractive index dependence of plasmon resonance for individual silver nanoparticles observed using darkfield micro-spectroscopy. 2005.